Par **Tea RUKAVINA**

Multi-scale damage model of fiber-reinforced concrete with parameter identification

Thèse présentée pour l'obtention du grade de Docteur de l'UTC

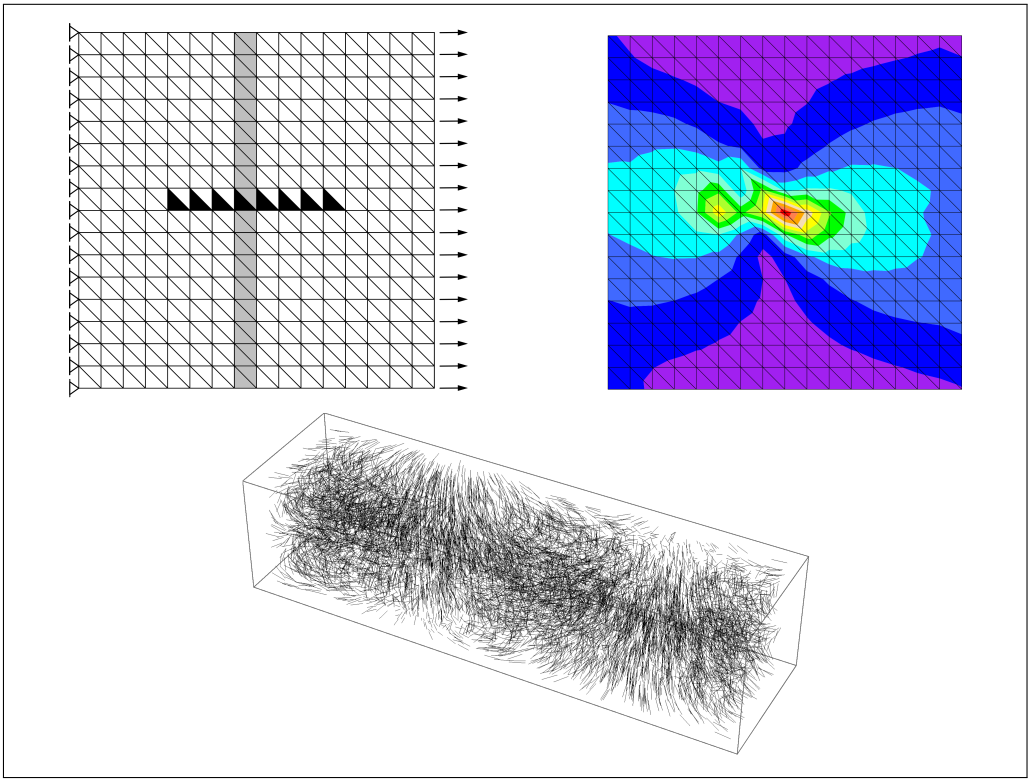

Soutenue le 17 décembre 2018

Specialité : Mécanique numérique

Unité de recherche en Mécanique - Laboratoire Roberval (UMR-7337)

UNIVERSITY OF RIJEKA, FACULTY OF CIVIL ENGINEERING

UNIVERSITÉ DE TECHNOLOGIE DE COMPIÈGNE
SORBONNE UNIVERSITÉS

Tea Rukavina

MULTI-SCALE DAMAGE MODEL OF FIBER-REINFORCED CONCRETE WITH PARAMETER IDENTIFICATION

DOCTORAL THESIS

Supervisors:

Prof. dr. sc. Ivica Kožar

Prof. dr. sc. Adnan Ibrahimbegović

Rijeka & Compiègne, 2018

The doctoral thesis was defended on December 17, 2018. at the University of Rijeka, Faculty of Civil Engineering, in front of the committee members:

1. Prof. dr. sc. Boštjan Brank, University of Ljubljana, Faculty of Civil and Geodetic Engineering
2. Prof. dr. sc. Zdenko Tonković, University of Zagreb, Faculty of Mechanical Engineering and Naval Architecture
3. Ass. prof. dr. sc. Neira Torić Malić, University of Rijeka, Faculty of Civil Engineering
4. Prof. emer. Pierre Villon, Université de Technologie de Compiègne, Sorbonne Universités
5. Dr. sc. Giulio Alfano, Brunel University London, Department of Mechanical, Aerospace and Civil Engineering
6. Dr. sc. Maja Gaćeša, Ansys Netherlands
7. Prof. dr. sc. Adnan Ibrahimbegović, Université de Technologie de Compiègne, Sorbonne Universités
8. Prof. dr. sc. Ivica Kožar, University of Rijeka, Faculty of Civil Engineering

”Whatever inspiration is,
it’s born from a continuous ’I don’t know.’”

Wisława Szymborska

Acknowledgements

The work on this thesis has been made possible by the Croatian Science Foundation Grant No. 9068 "Multi-scale concrete model with parameter identification", the EU founded project "Centre of Excellence for Structural Health (CEEStructHealth)", the French Government scholarship for doctoral level, and the Eiffel excellence scholarship awarded by the French Ministry of Europe and Foreign Affairs. All support is gratefully acknowledged.

First of all, I would like to thank my supervisors, professor Ivica Kožar and professor Adnan Ibrahimbegović, for their skillful guidance during my doctoral studies. They were always willing to share their knowledge and expertise, and offer new ideas and suggestions to follow. I have learned a lot from both, and not just about science.

I am greatful to professors Boštjan Brank, Zdenko Tonković and Neira Torić Malić, for carefully reading my thesis, and providing useful comments and suggestions. I also thank the members of the jury, Maja Gaćeša, Giulio Alfano, and Pierre Villon for their questions and their interest, I really appreciate it.

Many people from the University of Rijeka and Université de Technologie de Compiègne have given their particular contribution to the completion of this thesis. Special thanks go to Gordan Jelenić, who was the one to light the spark of scientific interest in me, and was always there to listen and help, and Gojko Balabanić with whom I shared many interesting conversations in our department's hallway. I would like to thank Delphine Brancherie and Norberto Dominguez for sharing their knowledge selflessly, and to Željko Smolčić and Marin Grbac for their contribution to the experimental part. I also thank Nilda Zelenika and Marina Đureta for making everything easier with their positive attitude.

Nothing would be the same without my wonderful colleagues from both universities, with whom I have shared these memorable years full of emotions, ranging from utter desperation to shear happiness. Emina, Pablo, Adela, Ivana, Ivona – I love you, guys. Abir, Andjelka, Andrea, Arturo, Carlos, Daniel, Edmundo, Eduard, Emir, Florian, Ismar, Laurette, Luis, Maria, Mijo, Milan, Miran, Natalija, Nina, Nino, Sara, Simona, Xuan Nam, and all the members of the Letifoka team, volley UTC, the coffee group, and H8bot – there has always been time for sports, a coffee, or a drink to share, and I am grateful for that.

And last but not least, I would like to thank my family, for their constant support and encouragement. Mom and dad, thank you for believing in me and teaching me what are the important things in life. Daniela, thank you for setting the bar high from the start, and for the magic box full of inspiration. Ivan, thank you for all the cool things you do every day to make me laugh.

Abstract

In this thesis, several approaches for modeling fiber-reinforced composites are proposed. The material under consideration is fiber-reinforced concrete, which is composed of a few constituents: concrete, short steel fibers, and the interface between them. The behavior of concrete is described by a damage model with localized failure, fibers are taken to be linear elastic, and the behavior of the interface is modeled with a bond-slip pull-out law. A multi-scale approach for coupling all the constituents is proposed, where the macro-scale computation is carried out using the operator-split solution procedure. This partitioned approach divides the computation in two phases, global and local, where different failure mechanisms are treated separately, which is in accordance with the experimentally observed composite behavior. An inverse model for fiber-reinforced concrete is presented, where the stochastic caracterization of the fibers is known from their distribution inside the domain. Parameter identification is performed by minimizing the error between the computed and measured values. The proposed models are validated through numerical examples.

Keywords: fiber-reinforced concrete, bond-slip, damage model, embedded discontinuity finite element method (ED-FEM), extended finite element method (X-FEM), multi-scale approach, fiber distribution, inverse modeling, parameter identification.

Prošireni sažetak

U ovom doktorskom radu razvija se nekoliko pristupa modeliranju betona ojačanog vlaknima, kako bi se omogućio odgovarajući opis ponašanja pri slomu. Beton ojačan vlaknima heterogeni je materijal pa više različitih faza mora biti uzeto u obzir: beton, čelična vlakna i veza između njih (eng. *interface*). U prvom dijelu rada promatra se mikro-struktura kompozita te su opisani detalji pri modeliranju svakog pojedinog dijela. Ponašanje betona opisano je 2D modelom oštećenja s očvršćavanjem i omekšanjem, gdje je lokalizirani slom uzet u obzir kroz ugrađeni diskontinuitet u polju pomaka (ED-FEM). Izotropni model oštećenja opisuje stvaranje mikropukotina u betonu nakon elastične faze, a anizotropnim se modelom oštećenja uzima u obzir otvaranje makro-pukotine u modu I ili modu II. Prilikom otvaranja pukotine, dolazi do disipacije energije, pri čemu površina ispod krivulje koja opisuje omekšanje materijala predstavlja energiju loma. Čelična vlakna su u ovom slučaju uzeta kao linearno elastična. Ponašanje veze između betona i vlakana modelira se pomoću 1D elastoplastičnog zakona ponašanja ili kroz opis čupanja vlakna, ovisno o rubnim uvjetima na krajevima vlakna. Upravo to kompletno čupanje vlakna iz betona jest komponenta koja nedostaje u mnogim do sada razvijenim modelima. Kako jedno vlakno može prolaziti kroz više konačnih elemenata, njegov utjecaj uzima se u obzir pomoću proširene metode konačnih elemenata (X-FEM).

Predstavljeni modeli pojedinih komponenti materijala međusobno su povezani višeskalnim pristupom, gdje se proračun na makro razini odvija u sklopu *operator-split* tehnike koja dijeli proračun u dvije faze, globalnu i lokalnu. U globalnoj fazi dobivaju se pomaci u betonu, a u lokalnoj fazi računa se proklizavanje veze između betona i vlakna. Takav sekvencijalni pristup omogućava brži i robusniji proračun, u usporedbi s pristupom gdje se sve jednadžbe rješavaju istovremeno. Razvijeni su trokutni konačni elementi koji, uz standardne stupnjeve slobode koji predstavljaju pomake u betonu, imaju i dodatne stupnjeve slobode koji opisuju proklizavanje vlakna. Originalni doprinos ovog rada uključuje i implementaciju svih triju komponenti materijala u jedan obogaćeni konačni element. Predložena teorijska formulacija implementirana je u računalni kod baziran na metodi konačnih elemenata *FEAP - Finite Element Analysis Program*. Provedene su numeričke simulacije za slučaj standardne armature i za slučaj ojačanja vlaknom, kako bi se testirala predložena metodologija.

Na primjerima je prikazana distribucija naprezanja duž vlakna, kao i odnos između otvaranja pukotine u betonu i proklizavanja vlakna. Također, provedena su laboratorijska ispitivanja izvlačenja jednog vlakna te ispitivanja savijanja u tri točke, kako bi se dobio bolji uvid u ponašanje kompozitnog materijala.

Nakon toga, predstavljen je inverzni model za beton ojačan vlaknima. Prikazano je kako se Levenberg-Marquard metoda može primijeniti na rješavanje inverznih problema te je dano nekoliko ilustrativnih primjera dobivanja parametara konstrukcije iz rezultata mjerenja. Stohastička karakterizacija vlakana dobivena je iz njihove prostorne distribucije koja je generirana pomoću predstavljenog algoritma izrađenom u softveru *Wolfram Mathematica*. Kako bi se povezali parametri materijala s globalnim dijagramom sila-pomak, model je formuliran preko *order statistics* i modela snopa vlakana (eng. *fiber bundle model*). Inverzni model omogućava provedbu identifikacije parametara, gdje se minimizira greška između izmjerenih i modeliranih vrijednosti.

U zaključnom dijelu rada dan je sveukupni komentar prikazanih rezultata, uz navođenje originalnih znanstvenih doprinosa te perspektiva za daljnji razvoj modela.

Ključne riječi: Beton ojačan vlaknima, proklizavanje između betona i vlakna, model oštećenja, višeskalni pristup, metoda konačnih elemenata s ugrađenim diskontinuitetom (ED-FEM), proširena metoda konačnih elemenata (X-FEM), raspodjela vlakana, inverzno modeliranje, identifikacija parametara.

Résumé étendu

Dans cette thèse, plusieurs approches de modélisation de composites renforcés par des fibres sont proposées. Le matériau étudié est le béton fibré, et dans ce modèle, on tient compte de l'influence de trois constituants : le béton, les fibres, et la liaison entre eux. Dans la première partie de la thèse, les détails de la micro-structure sont présentés, où les modèles de matériaux choisis sont expliqués précisément pour chaque constituant. Le comportement du béton est analysé avec une loi constitutive d'endommagement homogénéisé pour décrire les microfissures et une discontinuité dans le champ de déplacement (ED-FEM) qui représente une macrofissure. Le modèle d'endommagement anisotropique multi-surface décrit l'ouverture de la fissure en mode I ou en mode II. Lorsque la fissure s'ouvre, il se produit une dissipation d'énergie, où la surface sous la partie adoucissante de la courbe représente l'énergie de rupture. Les fibres d'acier sont considérées comme élastiques linéaires. Le comportement sur l'interface est décrit dans le cadre d'un modèle élastoplastique 1D, ou avec une loi de glissement avec extraction, en fonction des conditions limites sur les extrémités des fibres. L'originalité principale de ce travail est la prise en compte de l'extraction complète de la fibre, et ainsi la représentation pertinente de l'interaction de tous les mécanismes de rupture, ce qui a manqué dans tout autre modèle. Comme une fibre peut traverser plusieurs éléments finis, son influence est prise en compte à travers la méthode des éléments finis étendue (X-FEM).

Une approche multi-échelle pour coupler tous les constituants est proposée, dans laquelle le calcul à l'échelle macro est effectué dans la procédure de solution *operator-split*. Cela divise le calcul en deux phases qui sont liées aux deux phases de la rupture : au niveau global, on prend en compte l'influence du béton, de la fibre et du chargement externe, alors qu'au niveau local, on a seulement la fibre et le glissement. Cette approche partitionnée permet un calcul plus rapide et plus robuste, par rapport à l'approche monolithique où toutes les équations sont résolues simultanément. Concernant la mise en oeuvre de la méthodologie décrite, on a développé des éléments finis triangulaires qui, en plus des degrés de liberté standards représentant les déplacements du béton, ont des degrés de liberté supplémentaires décrivant le glissement. L'originalité de notre travail réside également dans la façon dont le calcul des trois composants est encapsulé dans un seul élément enrichi. L'implémentation

de cette formulation théorique est effectuée dans un logiciel d'éléments finis intitulé *FEAP - Finite Element Analysis Program*. Des simulations numériques du renforcement standard et du renforcement avec des fibres ont été effectuées pour valider la méthodologie proposée. En outre, des expériences en laboratoire ont été réalisées pour mieux comprendre les mécanismes de rupture des composites, notamment des essais de traction d'une fibre (*single-fiber pull-out tests*) et des essais de flexion à trois points sur des éprouvettes entaillées avec des fibres traversant l'entaille.

Dans la dernière partie de la thèse, un modèle inverse pour le béton fibré est présenté. Il est montré comment la méthode de Levenberg-Marquard peut être appliquée pour résoudre des problèmes inverses, avec plusieurs exemples illustratifs sur la détermination de paramètres de matériau à partir de données mesurées. Ensuite, la génération de la distribution aléatoire de fibres est expliquée, ainsi que sa mise en œuvre algorithmique dans le logiciel *Wolfram Mathematica*. La distribution obtenue est utilisée comme entrée pour le modèle inverse, dans lequel la caractérisation stochastique de chaque fibre est connue. Pour relier les paramètres du matériau à la courbe de charge-déplacement globale obtenue à partir d'expériences, un modèle direct est formé sur la base de statistiques ordonnées et du modèle de faisceau de fibres (*fiber bundle model*). Le modèle inverse nous permet d'effectuer l'identification des paramètres en minimisant l'erreur entre les valeurs mesurées et modélisées.

Mots clés : béton fibré, glissement entre le béton et l'acier, modèle d'endommagement, méthode des éléments finis avec discontinuité intégrée (ED-FEM), méthode des éléments finis étendue (X-FEM), approche multi-échelle, distribution des fibres, modélisation inverse, identification des paramètres.

Contents

1 Introduction

Contents

In this introductory part, the context and objectives of the thesis are laid out, together with the hypothesis and the research aims. Then, a literature review is given, where the most important research related to this thesis is considered. The materials and methodology part is followed by a short description of the thesis structure.

1.1 Context and objectives

Models capable of detecting cracks are a crucial tool for ensuring the durability and integrity of large structures such as bridges, dams, wind turbines, and nuclear power plants. The safety of the latter is especially important in France, where 3/4 of the total energy are produced by 19 nuclear power plants [1].

For this reason, it is crucial to determine when a structural element loses its functionality due to the propagation of damage during its lifetime. That is why we have to know when it is possible to repair existing structures and retain their functionality, and when it is it necessary to demolish them completely and replace them with new ones. The excellent properties of fiber-reinforced composites can be a part of the answer in both cases, because of their strength, increased ductility and good performance under dynamic loading. An example of such a material is fiber-reinforced concrete, which consists of a cement matrix, aggregate, and steel fibers. The most important benefit that comes with the addition of fibers is the increased resistance to cracking, because fibers bridge micro-cracks and prevent their coalescence into macro-cracks (Figure 1.1). This gives rise to better post-cracking performance, compared to standard concrete [2]. These improved properties are the reason for current applications of this material, from standard uses in pavements and in sprayed concrete (shotcrete), to new potential applications in floating structures for large off-shore wind turbines.

The difficulty imposed by the size of massive structures, which prevents the experimental validation, pushes us to develop faithful and predictive models, allowing us to provide a realistic description of the failure of the material (with the spacing and the opening of cracks). Thus, the only possibility is to resort to a multi-scale analysis, by detecting the processes that occur at all levels, from the micro-scale of the material to the macro-scale of the entire structure, ultimately leading to failure.

Figure 1.1: Crack in a fiber-reinforced concrete specimen at the end of a three-point bending test, with fibers bridging the notch.

1.2 Research hypothesis and research aims

The hypothesis of this thesis can be stated as:

Modelling fiber reinforced concrete using the proposed multi-scale approach is capable of providing an adequate representation of failure, and parameter identification can be used to obtain the model parameters.

The research aims are the following:

1. Develop a damage model of fiber reinforced concrete that takes into account the bond-slip between the concrete and the fibers;
2. Implement the coupling between the microstructure representation and the macro-scale response using a multi-scale approach;
3. Obtain material parameters of the model from inverse analysis.

1.3 Literature review

Microstructure representation is crucial in determining physical properties of composite materials, and artificial microstructures can be generated by relying on volume fraction information or statistical distributions, or using different imaging techniques such as X-ray microtomography combined with different reconstruction methods [3, 4]. In a number of previous works dealing with complex microstructures, the most often chosen approach is homogenization, smearing the material properties over a so-called representative volume element. For example, in [5] the authors are combining the extended finite element method and Monte Carlo simulations for modeling a domain with inclusions.

On the macro level, concrete can be considered to be a homogeneous material, but on the meso level, it has a heterogeneous structure, and is usually considered to be a three-phase material, consisting of aggregates, cement paste matrix, and the interface transition zone (ITZ) between them. Different constitutive models have been developed to represent the inelastic behavior of concrete at the macro-scale, such as elastoplasticity or damage models. In contrast, meso-scale models take into account each constituent separately, which gives a better representation of failure mechanisms, but also increases computational cost. To achieve balance between model fidelity and computational cost, adaptive solution strategies have been developed in which critical regions of the structure are modeled on the meso-scale, while other regions are approximated with a homogeneous macroscopic model [6]. This is an example of weak (hierarchical) multi-scale coupling, where the averaged properties are determined at the micro-scale and then transferred to the macro-scale,

implying separate analysis that brings us to a classic homogenization problem. In contrary, strong (concurrent) coupling requires simultaneous computation on both scales, where the scales have to communicate during the whole analysis [7]. An overview of micro-macro modelling of heterogeneous materials is given in [8]. Here, special care has to be taken to define the representative volume element (RVE), and to model the interface between the micro and the macro-scale. The computational aspects regarding numerical implementation of multi-scale methods using parallel computing are discussed in [9]. A multi-scale approach for modelling FRC can be found in [10].

Microstructure heterogeneity is closely related to failure mechanisms in concrete, characterized by initiation, propagation and coalescence of micro-cracks. Their localization gives rise to the formation of macro-cracks, leading to material softening. This means that large inelastic deformations develop within a small fracture process zone (FPZ), and the surrounding material starts to unload. To model such behavior, different approaches for crack representation have been developed, such as the discrete and smeared crack approach, the microplane model [11] etc. A review of existing damage models for concrete can be found in [12]. Also, the fracture of concrete can be simulated with lattice models [13, 14] consisting of 1D finite elements: beams or truss bars that represent cohesive links connecting two neighboring cells. One efficient way to make discrete models is by using Voronoi tessellation that creates polygonal structures dual to Delauney triangulation, and such models have shown computational robustness [15]. A comparison of discrete and continuum models for modeling fracture in concrete is given in [16].

In the embedded discontinuity finite element method (ED-FEM), a strong discontinuity is added inside the element to simulate the crack opening, so mesh dependency is avoided. This requires a modification of kinematic equations, where the enriched strain field is introduced, and it can be implemented in the framework of the method of incompatible modes [17]. As it can be seen in [18], the damage model with an embedded discontinuity applied to a beam finite element is suitable for describing the behavior of concrete. To see its application in a dynamic setting in 2D, see [19]. In [20] both displacement and strain discontinuity are implemented for a case when the boundary between two materials is located inside the element.

One of the biggest challenges in modelling FRC is introducing fibers into the model, for which different approaches can be used. In [21], authors are modelling the FRC microstructure with 4 phases: fibers, cement paste matrix, aggregates and ITZ, using a two-step homogenization approach. In [22] fibers are introduced into a discrete lattice model as zero-length springs positioned at the interface between two elements. In [23] the partition of unity finite element method (PUFEM or PUM

[24]) is used to model a continuum with embedded thin fibers, but the computation is limited to linear elastic behavior. In [25], the authors extend the application to the nonlinear behavior of both the matrix and the fiber, but their model cannot represent the fiber pull-out.

Another method that exploits the partition of unity property of standard interpolation functions is the extended finite element method (X-FEM) [26] where the mesh does not have to match the geometry or the microstructure, and global enrichment functions are used to model jumps, cracks, inclusions, etc. Since fibers can be considered as discontinuities inside the domain, the X-FEM approach is suitable for modelling fiber reinforced materials, like in [27], where the effect of individual fibers is analyzed at the meso-scale, and the observed properties are then transferred to the macro-scale. They apply the approach proposed in [28], where there are two enrichment functions in the displacement field approximation: one accounting for the discontinuity in the strain field, the other capturing the debonding along the fiber-matrix interface. The implementation of the same methodology in 3D is given in [29].

In [30] the X-FEM concept has been applied to standard reinforced concrete structures, where the bond-slip field has a global representation. Different bond models have been proposed for concrete with standard reinforcement, i.e. in [31] the bond-slip is taken into account through a zero-thickness interface element. The bond behavior could be also considered as a frictional slip [32, 33]. A multi-scale model for the treatment of slip in reinforced concrete can be found in [34]. In [35], a model for interfacial debonding in fiber-reinforced materials is presented, and in [36] pull-out is considered, also. For determining the bond-slip between fibers and concrete, single-fiber pull-out tests can be performed [37].

Being able to obtain material parameters from experimental data is very important in structural health monitoring and in the lifetime estimation of structures. It is crucial to determine when a structural component loses its resistance due to damage propagation, and that is why parameter identification is used. When solving inverse problems, the best agreement possible between predicted and measured values is required and the error has to be minimized, leading to an optimization problem. The application of this kind of procedure can be to identify a damaged element by determining its reduced stiffness. Identification of material parameters of a damage model for concrete can be seen in [38]. One step further is modelling in a probabilistic setting by accounting for the stochastic nature of the problem [39].

1.4 Materials and methodology

The research activities regarding this thesis can be divided into three complementary axes: microstructure representation, multi-scale analysis and inverse modeling.

The starting point is the microstructure representation of the material consisting of three phases: concrete, steel fibers, and the interface between them. The computational model for concrete is constructed using the finite element method, where the damage model with hardening and softening described in [40] is implemented. Each element in the mesh has an embedded discontinuity in the middle of the element that simulates the crack opening. The displacement discontinuity has to be introduced into the kinematic equations by enriching the displacement field, and it can be implemented as an incompatible mode. New degrees of freedom related to crack opening are introduced in each element, and static condensation is applied on the element level to keep only the standard degrees of freedom in the final equation. The damage of the material is defined through internal variables describing hardening and softening. The failure mechanisms start with the formation of micro-cracks in the fracture process zone (FPZ): it is a bulk dissipation happening in the hardening phase, which is taken into account through an isotropic damage model. When the limit strength is reached, the coalescence of micro-cracks takes place and a macro-crack starts to form, while the surrounding material is unloading. This is a surface dissipation happening at the discontinuity, that is described with an anisotropic multi-surface damage model which can take into account the crack opening in mode I and mode II. To attain computational efficiency, the computation is divided into two phases using the operator split method. In the local phase, evolution equations of internal variables are solved for every element using the Backward Euler integration scheme, and in the global phase, equilibrium equations are solved for the whole structure using the incremental and iterative Newton-Raphson method. New iterative sweeps are performed until equilibrium is achieved, giving as a result nodal displacements, the displacement at the discontinuity, stress in the elements and values of internal variables for every time step.

Fibers are modeled with a linear elastic constitutive law, and the behavior on the interface is described with an elasto-plastic or pull-out law, depending on the type of material we are modeling. For standard reinforced concrete, the ends of the reinforcement bar are anchored in concrete, and we consider the development of a plastic slip when the stress on the interface reaches the limit value. For fiber reinforcement, there is no anchorage, so the fiber can be pulled out of concrete. This is taken into account by a softening law that can be linear or exponential. The latter provides a better way to handle the complete pull-out of the fiber, since it gets close

to zero, but never reaches it, so it prevents numerical problems that arise when the bond stress reaches zero in the case of linear pull-out.

The microstructure representation serves as a building block for the macrostructure, so that the processes happening on the micro-scale directly affect the behavior on the macro-scale. The coupling of all the composite's constituents has been performed in a multi-scale framework. The operator-split solution procedure is used on the macro-level to divide the computation in two phases, resembling the real behavior of the composite. In the global phase, concrete and the fiber contribute to the computation, while in the local phase there is an influence of the fiber and the bond-slip [30]. The formulation has been developed using the X-FEM approximation of the displacement field, that allows for the continuity of bond-slip, as the fiber can pass through multiple finite elements [27, 28]. Both the monolithic and the partitioned approach were tested, to compare their computational efficiency and robustness.

To better understand the processes taking place during the pull-out of the fibers from the matrix, experimental test have been performed at the University of Rijeka, Faculty of Civil Engineering. Single-fiber pull-out tests have been performed on six specimens with different embedded lengths of the fibers. Also, three-point bending tests on special notched specimens with ten fibers bridging the notch have been performed [41]. The results of such tests help us to explain the failure mechanisms happening in fiber-reinforced composites. The interface fails at discrete locations in the specimen, where the cracks appear. In standard reinforced concrete, in which the steel bar is anchored at its ends, this leads to the yielding of the reinforcement at these locations. In fiber-reinforced concrete, where there is no anchorage, the appearance of the crack in concrete triggers the pull-out of the fiber. This has been observed during experiments, where none of the fibers reached their limit strength and did not break, but they all got pulled out of concrete. This important conclusion has been implemented in the numerical model.

Fibers are distributed randomly inside the domain, by taking into account their volume fraction. They are deposited independently of one another, they have an equal probability of landing at all points in the domain and of making all possible angles with an arbitrarily chosen fixed axis [42]. An algorithm is developed to generate a random distribution of fibers inside the domain in 2D and 3D. Inverse modelling is applied to obtaining model parameters from measurement results, and the Levenberg-Marquard method is used for solving the nonlinear least-squares problem. An iterative and incremental procedure is used to determine the stiffness of the damaged bar, when the values of measured displacements in some of the nodes are known; or to relate the displacement of two different structures, as has been shown in [43]. A model based on order statistics and the fiber bundle model is developed, where the

global force-displacement diagram is obtained from the contributions of all the fibers. The stochastic characterization of the model is based on the distribution of randomly generated values of length or stiffness. Order statistics provides a simple and efficient way to form an inverse model, from which parameter estimation can be performed.

The multi-scale model and the micro-structure contributions were implemented in the computer code *FEAP – Finite Element Analysis Program* [44], that is written in Fortran. A finite element was developed and tested on different examples. The fiber distribution algorithm and the Levenberg-Marquardt method for solving inverse problems were implemented in *Wolfram Mathematica* [45]. A part of the examples for the parameter identification part was solved in *Mathcad* [46]. The mesh for finite element examples has been generated in *gmsh* [47].

1.5 Structure of the thesis

This thesis is divided into five chapters. In the introductory part, the context and objectives of the research are laid down, and the hypothesis is defined, together with the literature review and the materials and methodology part. In Chapter 2, the details of the micro-structure are described, where the modeling approach for each constituent is explained. In Chapter 3, a multi-scale framework for taking into account fiber reinforcement is presented. Chapter 4 shows how an inverse model for fiber-reinforced concrete can be formed and solved, based on order statistics, the random distribution of fibers in the domain, and the Levenberg-Marquardt method. In the end, a conclusion is given, and the prospects for future work are outlined.

2

Micro-structure representation of the composite's constituents

Contents

To be able to model the composite's behavior and its failure modes at the macro-scale, we have to analyze first the constitutive law for each model ingredient. This includes a damage model for concrete, linear elasticity for the fibers, and an elasto-plastic or pull-out behavior on the interface. Each part has its own micro-scale computation, which provides the input for the macro-scale: stress value and tangent modulus. Special emphasis has been put on the bond-slip treatment, where experimental results for single-fiber pull-out test are presented.

In our approach, we are not approximating the characteristics of the composite as a whole, but are instead analysing each component separately, and then coupling them in a multi-scale setting. This allows us to have an adequate description of the behavior of every single part of the composite, and to choose a constitutive law and solution procedure most suitable for each one of it.

The behavior of concrete is described with a 2D damage model with hardening and softening, where the localized failure is taken into account through an embedded discontinuity in the displacement field. The short steel fibers are taken to be linear elastic. The behavior on the interface is model within a 1D elastoplastic setting, or with a pull-out bond-slip law, depending on the boundary conditions on the fiber ends. The behavior of concrete could be also described by a plasticity model [48, 49], or with viscoelasticity [50, 51].

On the macro-scale, we couple the influence of concrete, fibers and the interface. What is needed as an input from the micro-scale is the value of stress and the tangent modulus in each component: $\boldsymbol{\sigma}^{\mathrm{c}}$ and $\mathbf{C}^{\mathrm{ed}}$ for concrete, σ^{f} and E^{f} for the fiber, and σ^{bs} and C^{bs} for the bond-slip.

2.1 Damage model for concrete

The constitutive behavior of concrete can be described with different models. Here, we choose the elasto-damage model with hardening and softening that gives a realistic description of processes leading to failure, from the formation of the fracture process zone (FPZ) with the development of micro-cracks, to the opening of the macro-crack that leads to material softening [40, 52]. The hardening part is modelled with a continuum damage model that is isotropic, and the softening part is modelled with an embedded discontinuity in the displacement field that represents the crack opening in the middle of the element. This localized failure is treated within an anisotropic multi-surface model that can take into account the crack opening in mode I (traction), and in mode II (shear). The strong discontinuity is introduced as an incompatible mode [17, 53].

The chosen damage model is capable of representing the different phases of failure in the material. First, we have the elastic phase, followed by a damage phase with hardening that represents the fracture process zone that is characterized by the development of micro-cracks in the bulk of the material (volumetric dissipation). When the micro-cracks coalesce in a large macro-crack, surface dissipation happens, which is described by the localized failure in the softening phase. On Figure 2.1 we can observe these three distinctive phases, shown in black (elasticity), blue (hardening), and red (softening).

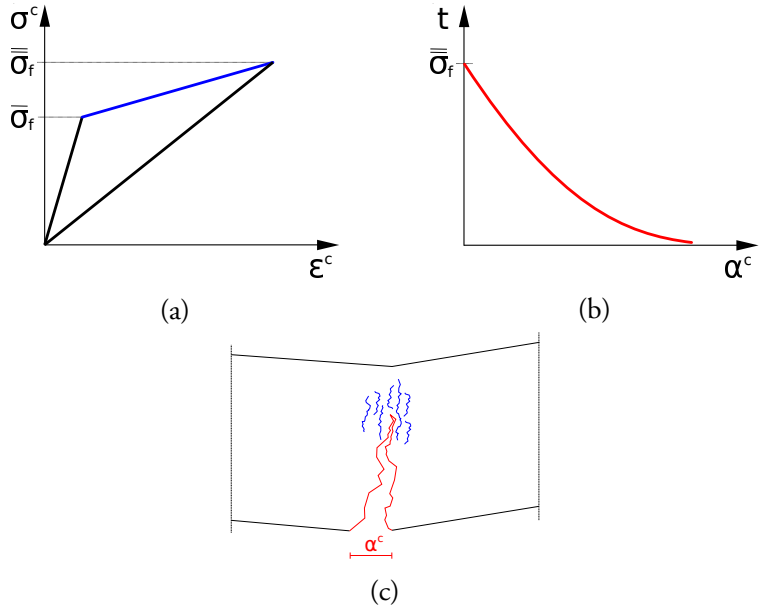

Figure 2.1: Crack development in concrete - three phases of material behavior: elasticity (black), hardening (blue), softening (red): (a) stress-strain diagram for the bulk material (elasticity + hardening phase + elastic unloading); (b) traction-separation cohesive law at the discontinuity (softening phase); (c) micro-cracks (blue) and macro-crack (red) in a specimen.

2.1.1 Kinematics of a finite element with an embedded strong discontinuity

The handling of the displacement jump inside the element is done through the introduction of an incompatible mode function, as in [17]. The implementation details for the method of incompatible modes can be found in [53].

The total displacement field of a single element is then a sum of the standard and the incompatible part

$$\mathbf{u}^c(\mathbf{x}) = \mathbf{N}\,\mathbf{d}^c + \mathbf{M}\,\boldsymbol{\alpha}^c \tag{2.1}$$

where $\mathbf{d}^c$ is the nodal displacement vector for standard degrees of freedom of a constant strain triangle (CST) element, and $\boldsymbol{\alpha}^c$ is the vector of incompatible displacements that represent the crack opening at the discontinuity. $\mathbf{N}$ is the matrix of linear shape functions for a triangular element, shown in Figure 2.2, and $\mathbf{M}$ is the matrix of incompatible shape functions, which have the following form

$$\mathbf{N} = \begin{bmatrix} N_1 & 0 & N_2 & 0 & N_3 & 0 \\ 0 & N_1 & 0 & N_2 & 0 & N_3 \end{bmatrix}; \quad \mathbf{M} = \begin{bmatrix} M & 0 \\ 0 & M \end{bmatrix}; \tag{2.2}$$

The standard shape functions N_a, $a = 1, 2, 3$, can be found in [54], while the incompatible shape function M is computed from (2.9).

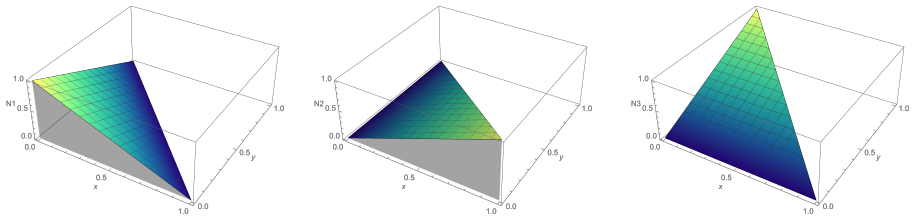

(a) (b) (c)

Figure 2.2: Shape functions for a CST element: (a) N_1; (b) N_2; (c) N_3.

From (2.1), it follows that the strain field approximation is

$$\boldsymbol{\varepsilon}^{\mathrm{c}} = \mathbf{B}\,\mathbf{d}^{\mathrm{c}} + \mathbf{G}_{\mathrm{r}}\,\boldsymbol{\alpha}^{\mathrm{c}} \tag{2.3}$$

where $\mathbf{B}$ is the matrix of standard shape functions' derivatives, and $\mathbf{G}_{\mathrm{r}}$ is the matrix of the incompatible shape function's derivatives. $\mathbf{G}_{\mathrm{r}}$ consists of a regular and a singular part

$$\mathbf{G}_{\mathrm{r}} = \bar{\mathbf{G}}_{\mathrm{r}} + \bar{\bar{\mathbf{G}}}_{\mathrm{r}} \tag{2.4}$$

Matrix $\mathbf{B}$ and the regular part of matrix $\mathbf{G}_{\mathrm{r}}$ have the following form

$$\mathbf{B} = \begin{bmatrix} \frac{dN_1}{dx} & 0 & \frac{dN_2}{dx} & 0 & \frac{dN_3}{dx} & 0 \\ 0 & \frac{dN_1}{dy} & 0 & \frac{dN_2}{dy} & 0 & \frac{dN_3}{dy} \\ \frac{dN_1}{dy} & \frac{dN_1}{dx} & \frac{dN_2}{dy} & \frac{dN_2}{dx} & \frac{dN_3}{dy} & \frac{dN_3}{dx} \end{bmatrix}; \quad \bar{\mathbf{G}}_{\mathrm{r}} = \begin{bmatrix} \frac{dM}{dx} & 0 \\ 0 & \frac{dM}{dy} \\ \frac{dM}{dy} & \frac{dM}{dx} \end{bmatrix} \tag{2.5}$$

while the singular part in (2.4) is defined as $\bar{\bar{\mathbf{G}}}_{\mathrm{r}} = \mathbf{n}\,\delta_{\Gamma_s}$. Here, $\mathbf{n}$ is the normal vector on the discontinuity surface, and δ_{Γ_s} is the Dirac delta function, that represents the derivative of the Heaviside function at the discontinuity.

To illustrate this for a simple case, the standard shape functions N_1 and N_2 for a truss bar element, together with the incompatible shape function M and its derivative G are shown on Figure 2.3.

In a 2D case, a modification has to be made for the function $\mathbf{G}_{\mathrm{r}}$ to satisfy the patch test, according to the modified method of incompatible modes [17]

$$\mathbf{G}_{\mathrm{v}} = \mathbf{G}_{\mathrm{r}} - \frac{1}{A^e}\int_{\Omega^e} \mathbf{G}_{\mathrm{r}}\, d\Omega^e \tag{2.6}$$

where A^e is the area of the finite element. The modified incompatible shape function also consists of a regular and a singular part, as in (2.4)

$$\mathbf{G}_{\mathrm{v}} = \bar{\mathbf{G}}_{\mathrm{v}} + \bar{\bar{\mathbf{G}}}_{\mathrm{v}} \tag{2.7}$$

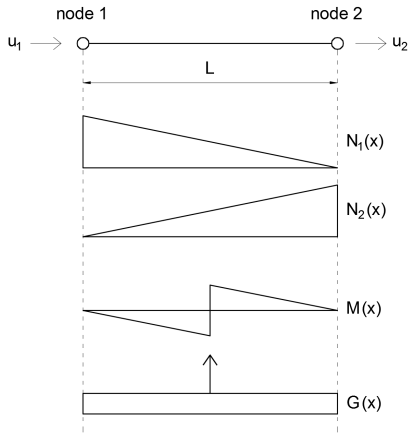

Figure 2.3: Standard shape functions and incompatible shape function with its derivative for a truss bar.

which are obtained by introducing (2.4) into (2.6), as shown in [55]

$$\bar{\mathbf{G}}_{\mathrm{v}} = \bar{\mathbf{G}}_{\mathrm{r}} - \frac{1}{A^e}\int_{\Omega^e} \bar{\mathbf{G}}_{\mathrm{r}}\, d\Omega^e - \frac{l^e_{\Gamma_s}}{A^e}\mathbf{n}; \quad \bar{\bar{\mathbf{G}}}_{\mathrm{v}} = \bar{\bar{\mathbf{G}}}_{\mathrm{r}} \tag{2.8}$$

In the above equation, $l^e_{\Gamma_s}$ is the length of the discontinuity.

Figure 2.4 shows the discontinuity surface Γ_s (that is represented by a line in 2D), where we denote by Ω^- and Ω^+ the parts of the element domain at each side of the discontinuity Γ_s, respectively. Vectors $\mathbf{n}$ and $\mathbf{m}$ are the normal and the tangential vector at the discontinuity. The chosen element has only one Gauss numerical integration point, which is located in the triangle barycenter. The discontinuity surface Γ_s passes through it, and is oriented positive towards Ω^+.

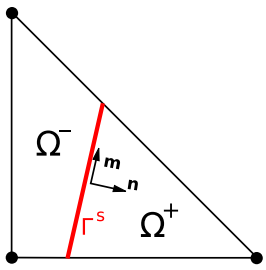

Figure 2.4: Discontinuity surface Γ_s in an element.

The incompatible shape function M is obtained by introducing a Heaviside function H that accounts for the strong discontinuity in the displacement field. The Heaviside function is equal to zero in Ω^-, and equal to one in Ω^+. The incompatible shape function M (Figure 2.5) is computed as the difference between the Heaviside

function and the sum of shape functions for the nodes that are in Ω^+

$$M = H - \sum_{a \in \Omega^+} N_a \tag{2.9}$$

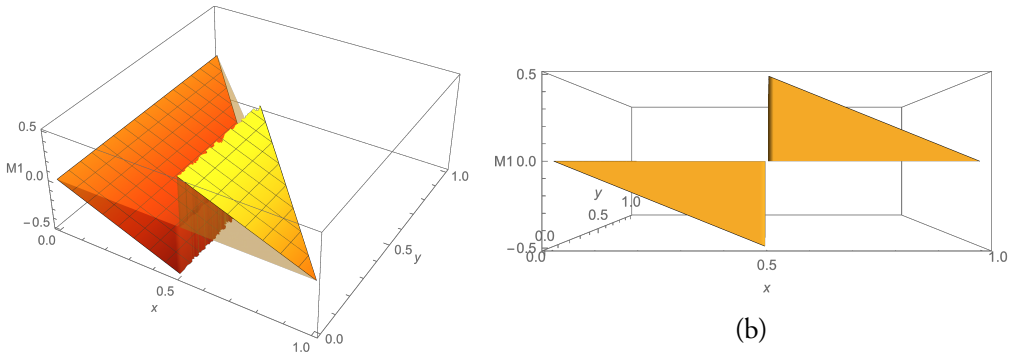

Figure 2.5: Example of the incompatible shape function M for for a CST element when the discontinuity passes through the middle of the element: (a) 3D view; (b) front view.

2.1.2 Equilibrium equations

From the principle of virtual work it follows that

$$G^{\text{int}} = G^{\text{ext}} \tag{2.10}$$

where G^{ext} is the virtual work of external forces

$$G^{\text{ext}} = \mathbf{w}^{\text{c},T}\, \mathbf{f}^{\text{ ext}} \tag{2.11}$$

and G^{int} is the virtual work of internal forces

$$G^{\text{int}} = \mathbf{w}^{\text{c},T}\, \mathbf{f}^{\text{ int}} + \tilde{\boldsymbol{\alpha}}^{\text{c}}\, \mathbf{h} \tag{2.12}$$

In the above equations, $\mathbf{w}^{\text{c}}$ are the nodal virtual displacements for a CST element, and $\tilde{\boldsymbol{\alpha}}^{\text{c}}$ is the virtual displacement jump. The external force vector $\mathbf{f}^{\text{ ext}}$ is defined as

$$\mathbf{f}^{\text{ ext}} = \int_{\Omega} \mathbf{N}^T \mathbf{b}\, d\Omega + \int_{\Gamma_\sigma} \mathbf{N}^T \mathbf{t}_{\Gamma_\sigma}\, d\Gamma_\sigma \tag{2.13}$$

where $\mathbf{b}$ are the volume forces, and $\mathbf{t}_{\Gamma_\sigma}$ is the traction acting at the boundary $d\Gamma_\sigma$. The internal force vector $\mathbf{f}^{\text{ int}}$ is defined as

$$\mathbf{f}^{\text{ int}} = \int_{\Omega} \mathbf{B}^T \boldsymbol{\sigma}^{\text{c}}\, d\Omega \tag{2.14}$$

Here, $\boldsymbol{\sigma}^{\mathrm{c}}$ is the stress in concrete, which is computed from the constitutive equation for the damage model

$$\boldsymbol{\sigma}^{\mathrm{c}} = \mathbf{C}^{\mathrm{ed}} \boldsymbol{\varepsilon}^{\mathrm{c}} \tag{2.15}$$

where $\mathbf{C}^{\mathrm{ed}}$ is the elasto-damage modulus that will be defined in the next section, and $\boldsymbol{\varepsilon}^{\mathrm{c}}$ is computed according to (2.3). In (2.12), $\mathbf{h}$ is defined as

$$\mathbf{h} = \int_{\Omega} \bar{\mathbf{G}}_{\mathrm{v}}^{T} \boldsymbol{\sigma}^{\mathrm{c}} \, d\Omega + \int_{\Gamma_s} \bar{\bar{\mathbf{G}}}_{\mathrm{v}}^{T} \mathbf{t} \, d\Gamma_s \tag{2.16}$$

where $\mathbf{t}$ is the traction acting at the discontinuity.

By introducing (2.11) and (2.12) into (2.10), two sets of equations are obtained

$$\mathbf{f}^{\,\mathrm{int}} - \mathbf{f}^{\,\mathrm{ext}} = \mathbf{0} \tag{2.17}$$

$$\mathbf{h} = \mathbf{0} \tag{2.18}$$

defining the equilibrium of the structure. The residual vector is defined as $\mathbf{r} = \mathbf{f}^{\,\mathrm{int}} - \mathbf{f}^{\,\mathrm{ext}}$.

Since the above equations are nonlinear, we solve them with a Newton-Raphson solution procedure. When we linearize system (2.17), we get

$$\mathbf{K} \, \Delta \mathbf{d}^{\mathrm{c}}_{n+1} + \mathbf{F}_{\mathrm{r}} \, \Delta \boldsymbol{\alpha}^{\mathrm{c}}_{n+1} = -\mathbf{r}_{n+1} \tag{2.19}$$

$$\mathbf{F}_{\mathrm{v}} \, \Delta \mathbf{d}^{\mathrm{c}}_{n+1} + (\mathbf{H} + \mathbf{K}_{\alpha}) \, \Delta \boldsymbol{\alpha}^{\mathrm{c}}_{n+1} = \mathbf{0} \tag{2.20}$$

where the tangent stiffness matrices are defined as

$$\mathbf{K} = \int_{\Omega} \mathbf{B}^{T} \mathbf{C}^{\mathrm{ed}} \, \mathbf{B} \, d\Omega \tag{2.21}$$

$$\mathbf{F}_{\mathrm{r}} = \int_{\Omega} \mathbf{B}^{T} \mathbf{C}^{\mathrm{ed}} \, \bar{\mathbf{G}}_{\mathrm{r}} \, d\Omega \tag{2.22}$$

$$\mathbf{F}_{\mathrm{v}} = \int_{\Omega} \bar{\mathbf{G}}_{\mathrm{v}}^{T} \mathbf{C}^{\mathrm{ed}} \, \mathbf{B} \, d\Omega \tag{2.23}$$

$$\mathbf{H} = \int_{\Omega} \bar{\mathbf{G}}_{\mathrm{v}}^{T} \mathbf{C}^{\mathrm{ed}} \, \bar{\mathbf{G}}_{\mathrm{r}} \, d\Omega \tag{2.24}$$

In equation (2.20), the term $\mathbf{K}_{\alpha}$ is defined as $\mathbf{K}_{\alpha} = l_{\Gamma_s} \bar{\bar{\mathbf{C}}}^{\mathrm{ed}}$, where l_{Γ_s} is the discontinuity length, and $\bar{\bar{\mathbf{C}}}^{\mathrm{ed}}$ is the tangent modulus for the discontinuity that will be defined in the following section.

Since the global equilibrium equation in (2.17) is solved for the whole structure, and the local one is solved on the element level, we can perform a static condensation in which the crack opening is expressed from (2.20) as

$$\Delta \boldsymbol{\alpha}^{\mathrm{c}}_{n+1} = -(\mathbf{H} + \mathbf{K}_{\alpha})^{-1} \mathbf{F}_{\mathrm{v}} \, \Delta \mathbf{d}^{\mathrm{c}}_{n+1} \tag{2.25}$$

By introducing (2.25) into (2.19), we get

$$\hat{\mathbf{K}}^{\mathrm{c}}\,\Delta\mathbf{d}^{\mathrm{c}}_{n+1} = -\mathbf{r}_{n+1} \tag{2.26}$$

where $\hat{\mathbf{K}}^{\mathrm{c}}$ is the condensed stiffness matrix for concrete that is equal to

$$\hat{\mathbf{K}}^{\mathrm{c}} = \mathbf{K} - \mathbf{F}_{\mathrm{r}}\left(\mathbf{H} + \mathbf{K}_{\alpha}\right)^{-1}\mathbf{F}_{\mathrm{v}} \tag{2.27}$$

The incremental value $\Delta\mathbf{d}^{c}$ is computed from (2.26) in the global iterations, and the update of the concrete displacements is performed

$$\mathbf{d}^{\mathrm{c}}_{n+1} = \mathbf{d}^{\mathrm{c}}_{n} + \Delta\mathbf{d}^{\mathrm{c}}_{n+1} \tag{2.28}$$

The crack opening is computed in the local iterations on the element level, together with the other internal variables of the model. The implementation for the isotropic damage model in the bulk, and the anisotropic multi-surface damage model at the discontinuity will be presented in the next two sections.

2.1.3 Bulk computation

An isotropic damage model governs the micro-crack development in the bulk, that is taking place in the hardening phase of the response. The evolution of damage can be described by a Lagrange multiplier $\bar{\gamma}$ that can take only non-negative values. We will introduce a damage function $\bar{\phi}$ that checks the admissibility of stress in the bulk. The Kuhn-Tucker loading/unloading conditions are listed here:

$$\dot{\bar{\gamma}} \geq 0, \quad \bar{\phi} \leq 0, \quad \dot{\bar{\gamma}}\bar{\phi} = 0 \tag{2.29}$$

Here, the dot above the symbol denotes a derivative with respect to time. The damage consistency condition which enforces the stress admissibility at subsequent time steps can be written as $\dot{\bar{\gamma}}\dot{\bar{\phi}} = 0$. This means that there are two admissible cases: the elastic case, with $\bar{\phi} < 0$ and $\dot{\bar{\gamma}} = 0$, and the damage case, with $\bar{\phi} = 0$ and $\dot{\bar{\gamma}} > 0$.

The internal variables for the damage model are $\bar{\mathbf{D}}$, the damage compliance tensor for the bulk material, and $\bar{\xi}$, the hardening variable. $\bar{q}_n$ is the stress-like hardening variable that controls the damage threshold evolution. For linear hardening, we have

$$\bar{q} = -\bar{K}^{\mathrm{c}}\bar{\xi} \tag{2.30}$$

where $\bar{K}^{\mathrm{c}}$ is the hardening modulus for concrete. The evolution equations of the internal variables are defined in [55] as

$$\dot{\bar{\mathbf{D}}} = \dot{\bar{\gamma}}\,\frac{\bar{\mathbf{D}}}{||\boldsymbol{\sigma}^{\mathrm{c}}||_{\boldsymbol{D}^{\mathrm{e}}}}; \qquad \dot{\bar{\xi}} = \dot{\bar{\gamma}}\,\frac{1}{\sqrt{E^{\mathrm{c}}}} \tag{2.31}$$

and we solve them using the implicit backward Euler scheme. In (2.31) E^{c} is the Young's modulus for concrete, and $||\boldsymbol{\sigma}^{\mathrm{c}}||_{\boldsymbol{D}^{\mathrm{e}}}$ is the norm of $\boldsymbol{\sigma}^{\mathrm{c}}$ in stress space, where "$\cdot$" stands for the dot product (scalar product) between two vectors

$$||\boldsymbol{\sigma}^{\mathrm{c}}||_{\boldsymbol{D}^{\mathrm{e}}} = \sqrt{\boldsymbol{\sigma}^{\mathrm{c}} \cdot \boldsymbol{D}^{\mathrm{e}} \boldsymbol{\sigma}^{\mathrm{c}}} \tag{2.32}$$

In the beginning of the computation, for a virgin material, $\bar{\mathbf{D}} = \boldsymbol{D}^{\mathrm{e}}$, where the latter is the undamaged elastic compliance tensor for the bulk material. It is computed as the inverse of the elastic constitutive matrix

$$\boldsymbol{D}^{\mathrm{e}} = (\boldsymbol{C}^{\mathrm{e}})^{-1} \tag{2.33}$$

For the plane strain case, $\boldsymbol{C}^{\mathrm{e}}$ is defined as

$$\boldsymbol{C}^{\mathrm{e}} = \frac{E^{\mathrm{c}}}{(1+\nu^{\mathrm{c}})(1-2\nu^{\mathrm{c}})} \begin{bmatrix} 1-\nu^{\mathrm{c}} & \nu^{\mathrm{c}} & 0 \\ \nu^{\mathrm{c}} & 1-\nu^{\mathrm{c}} & 0 \\ 0 & 0 & \dfrac{1-2\nu^{\mathrm{c}}}{2} \end{bmatrix} \tag{2.34}$$

where ν^{c} is the Poisson's ratio for concrete.

Elastic trial step

We start the computation in the elastic trial step by assuming that no evolution of internal variables takes place, with $\bar{\gamma}_{n+1} = 0$, and the trial values taken from the last converged step

$$\bar{\xi}^{trial}_{n+1} = \bar{\xi}_n; \quad \bar{q}^{trial}_{n+1} = \bar{q}_n; \quad \bar{\mathbf{D}}^{trial}_{n+1} = \bar{\mathbf{D}}_n \tag{2.35}$$

We start with computing the trial value of stress that is defined as

$$\boldsymbol{\sigma}^{\mathrm{c},trial}_{n+1} = \bar{\mathbf{D}}^{-1}_n \bar{\boldsymbol{\varepsilon}}^{\mathrm{c}}_{n+1} \tag{2.36}$$

where $\bar{\boldsymbol{\varepsilon}}^{\mathrm{c}}_{n+1}$ is the standard part of the strain field (without taking into account the displacement jump $\boldsymbol{\alpha}^{\mathrm{c}}$).

To determine if we are in the elastic phase, or if damage has already occurred, we have to check the trial value of the damage function, according to [55]

$$\bar{\phi}^{trial}_{n+1} = ||\boldsymbol{\sigma}^{\mathrm{c},trial}_{n+1}||_{\boldsymbol{D}^{\mathrm{e}}} - \frac{1}{\sqrt{E^{\mathrm{c}}}}(\sigma_f - \bar{q}_{n+1}) \overset{?}{\leq} 0 \tag{2.37}$$

and according to (2.30), we have: $\bar{q}_{n+1} = -\bar{K}^{\mathrm{c}} \bar{\xi}_n$.

If the damage function is less than or equal to zero ($\bar{\phi}^{trial}_{n+1} \leq 0$), the step is indeed elastic, and we take the trial values as final

$$\boldsymbol{\sigma}^{\mathrm{c}}_{n+1} = \boldsymbol{\sigma}^{\mathrm{c},trial}_{n+1}; \quad \bar{\xi}_{n+1} = \bar{\xi}^{trial}_{n+1}; \quad \bar{q}_{n+1} = \bar{q}^{trial}_{n+1}; \quad \bar{\mathbf{D}}_{n+1} = \bar{\mathbf{D}}^{trial}_{n+1} \tag{2.38}$$

and the elasto-damage modulus for the elastic case is equal to the inverse of the damage compliance tensor from the previous time step

$$\bar{\mathbf{C}}^{\mathrm{ed}}_{n+1} = \bar{\mathbf{D}}^{-1}_{n} \tag{2.39}$$

If $\bar{\phi}^{trial}_{n+1} > 0$, the step is not elastic, and we have to proceed to the damage correction step.

Damage step

If damage has occurred, the damage multiplier $\bar{\gamma}$ is not equal to zero any more, and we have to compute its new value. In this subsection, equations are derived according to [55]. The damage multiplier at time t_{n+1} is equal to

$$\bar{\gamma}_{n+1} = \frac{\bar{\phi}^{trial}_{n+1}}{\dfrac{1}{1+\bar{\mu}_n} + \dfrac{\bar{K}^{\mathrm{c}}}{E^{\mathrm{c}}}} \tag{2.40}$$

where $\bar{\mu}$ is the generalized Lagrange multiplier defining the damage evolution. We can introduce a scalar damage variable defined as

$$d = \frac{\bar{\mu}}{1+\bar{\mu}} \tag{2.41}$$

so we can write the relationship between the damage compliance tensor and the elastic tensor as

$$\bar{\mathbf{D}}^{-1} = (1-d)\,\mathbf{C}^{\mathrm{e}} \tag{2.42}$$

Using the new value of $\bar{\gamma}_{n+1}$ computed in Eq. (2.40), we can update the values of the internal variables

$$\bar{\mu}_{n+1} = \bar{\mu}_n + \frac{\bar{\gamma}_{n+1}}{||\boldsymbol{\sigma}^{\mathrm{c},trial}_{n+1}||_{\boldsymbol{D}^e} - \dfrac{\bar{\gamma}_{n+1}}{1+\bar{\mu}_n}} \tag{2.43}$$

$$\bar{\xi}_{n+1} = \bar{\xi}_n + \frac{1}{\sqrt{E^{\mathrm{c}}}}\,\bar{\gamma}_{n+1} \tag{2.44}$$

$$\bar{\mathbf{D}}_{n+1} = \bar{\mathbf{D}}_n + \bar{\gamma}_{n+1}\,\frac{\boldsymbol{D}^{\mathrm{e}}}{||\boldsymbol{\sigma}^{\mathrm{c}}_{n+1}||_{\boldsymbol{D}^{\mathrm{e}}}} \tag{2.45}$$

The final value of stress can be computed in the following manner

$$\boldsymbol{\sigma}^{\mathrm{c}}_{n+1} = \boldsymbol{\sigma}^{\mathrm{c},trial}_{n+1} - \frac{\bar{\gamma}_{n+1}}{1+\bar{\mu}_n}\mathbf{N}^{trial}_{n+1} \tag{2.46}$$

where $\mathbf{N}^{trial}$ is defined as

$$\mathbf{N}_{n+1}^{trial} = \frac{\boldsymbol{\sigma}_{n+1}^{\mathrm{c},trial}}{||\boldsymbol{\sigma}_{n+1}^{\mathrm{c},trial}||_{\boldsymbol{D}^{\mathrm{e}}}} \tag{2.47}$$

Finally, we can compute the value of the elasto-damage modulus for the bulk

$$\bar{\mathbf{C}}_{n+1}^{\mathrm{ed}} = \frac{\mathbf{C}^{\mathrm{e}}}{1+\bar{\mu}_n}\left(1 - \frac{\bar{\gamma}_{n+1}}{(1+\bar{\mu}_n)\,||\boldsymbol{\sigma}_{n+1}^{\mathrm{c},trial}||_{\boldsymbol{D}^{\mathrm{e}}}}\right) + \\ + \frac{1}{(1+\bar{\mu}_n)^2}\left(\frac{\bar{\gamma}_{n+1}}{||\boldsymbol{\sigma}_{n+1}^{\mathrm{c},trial}||_{\boldsymbol{D}^{\mathrm{e}}}} - \frac{1}{\dfrac{1}{1+\bar{\mu}_n} + \dfrac{\bar{K}^{\mathrm{c}}}{E^{\mathrm{c}}}}\right)\mathbf{N}_{n+1}^{trial} \otimes \mathbf{N}_{n+1}^{trial} \tag{2.48}$$

Discontinuity activation condition

If the principal stress is larger than the ultimate stress $\bar{\bar{\sigma}}_f$, softening has started, and we proceed to the computation at the discontinuity. Then, we shift from the continuum damage model (micro-crack development), to the localized failure model (macro-crack opening).

Principal stresses are computed in the standard manner, using the stress from (2.46), that is defined as a vector $\boldsymbol{\sigma}^{\mathrm{c},T} = \begin{bmatrix}\sigma_{xx}^{\mathrm{c}} & \sigma_{yy}^{\mathrm{c}} & \tau_{xy}^{\mathrm{c}}\end{bmatrix}$. The principal stresses are then

$$\sigma_{1,2}^{\mathrm{c}} = \frac{\sigma_{xx}^{\mathrm{c}} + \sigma_{yy}^{\mathrm{c}}}{2} \pm \sqrt{\left(\frac{\sigma_{xx}^{\mathrm{c}} + \sigma_{yy}^{\mathrm{c}}}{2}\right)^2 + (\tau_{xy}^{\mathrm{c}})^2} \tag{2.49}$$

The angle θ between the principal direction and the x-axis is

$$\tan(2\theta) = \frac{\tau_{xy}^{\mathrm{c}}}{\sigma_{xx}^{\mathrm{c}} - \sigma_{yy}^{\mathrm{c}}} \tag{2.50}$$

which defines the orientation of the discontinuity surface Γ_{s} (represented by a line in 2D). The normal and tangential vector on the discontinuity are then

$$\mathbf{n} = \begin{bmatrix}\cos\theta \\ \sin\theta\end{bmatrix}; \qquad \mathbf{m} = \begin{bmatrix}-\sin\theta \\ \cos\theta\end{bmatrix} \tag{2.51}$$

From the orientation of Γ_{s}, we determine which nodes of our element are on which side of the discontinuity surface, Ω^+ or Ω^-, as shown in Figure 2.4.

Once we enter the computation at the discontinuity, we do not perform the bulk computation any more, and we continue using the values of internal variables from the last converged step. In the softening phase, the stress is localized at the discontinuity, and the bulk of the material is unloading, so C^{ed} should be computed from (2.39), as for the elastic case.

2.1.4 Computation at the discontinuity

Since the softening part of the response is controlled by an anisotropic multi-surface damage model, we have to consider each direction at the discontinuity surface separately. This kind of model can account for the crack opening in mode I (in the normal direction) and mode II (in the tangential direction), denoted by subscripts 1 and 2 in the following equations.

As for the hardening part of the response, the damage evolution at the discontinuity is described with internal variables. There are two Lagrange multipliers at the discontinuity, $\dot{\bar{\gamma}}_1$ and $\dot{\bar{\gamma}}_2$, one for each direction. The admissibility of traction is checked with the damage functions $\bar{\phi}_1$ and $\bar{\phi}_2$, The Kuhn-Tucker conditions for the discontinuity are defined similarly to (2.29), but for both directions

$$\dot{\bar{\gamma}}_1 \geq 0, \quad \bar{\phi}_1 \leq 0, \quad \dot{\bar{\gamma}}_1 \bar{\phi}_1 = 0 \tag{2.52}$$

$$\dot{\bar{\gamma}}_2 \geq 0, \quad \bar{\phi}_2 \leq 0, \quad \dot{\bar{\gamma}}_2 \bar{\phi}_2 = 0 \tag{2.53}$$

and the consistency conditions are

$$\dot{\bar{\gamma}}_1 \dot{\bar{\phi}}_1 = 0 \tag{2.54}$$

$$\dot{\bar{\gamma}}_2 \dot{\bar{\phi}}_2 = 0 \tag{2.55}$$

The constitutive equation relating the traction at the discontinuity $\mathbf{t}$ and the displacement jump $\boldsymbol{\alpha}^{\mathrm{c}}$ is based on a traction-separation cohesive law

$$\mathbf{t} = \bar{\mathbf{Q}}^{-1} \boldsymbol{\alpha}^{\mathrm{c}} \tag{2.56}$$

where $\bar{\mathbf{Q}}$ is the damage compliance tensor for the discontinuity, which can be written in the coordinate system $(\mathbf{n}, \mathbf{m})$ in the following manner

$$\bar{\mathbf{Q}} = \begin{bmatrix} \bar{Q}_{nn} & 0 \\ 0 & \bar{Q}_{mm} \end{bmatrix} \tag{2.57}$$

with $\bar{Q}_{nn}$ and $\bar{Q}_{mm}$ being its normal and tangential component.

We can write the evolution equations for the softening part of the response which have been derived in [55]

$$\dot{\bar{\mathbf{Q}}} = \dot{\bar{\gamma}}_1 \frac{\mathbf{n} \otimes \mathbf{n}}{\mathbf{t} \cdot \mathbf{n}} + \dot{\bar{\gamma}}_2 \frac{\mathbf{m} \otimes \mathbf{m}}{|\mathbf{t} \cdot \mathbf{m}|}; \tag{2.58}$$

$$\dot{\bar{\xi}} = \dot{\bar{\gamma}}_1 + \dot{\bar{\gamma}}_2 \frac{\bar{\sigma}_s}{\bar{\sigma}_f} \tag{2.59}$$

$$\dot{\bar{q}} = -\bar{K}^{\mathrm{c}} \dot{\bar{\xi}} \tag{2.60}$$

In the above equations, $\bar{\bar{\sigma}}_s/\bar{\bar{\sigma}}_f$ is the ratio between the ultimate stress in shear (tangential direction) and in tension (normal direction), $\bar{\bar{\xi}}$ represents the softening variable, and $\bar{\bar{q}}$ is the traction-like softening variable that represents the coupling term between the two directions. For the case of exponential softening, we can write

$$\bar{\bar{q}} = \bar{\bar{\sigma}}_f \left[1 - \exp\left(-\frac{\bar{\bar{\beta}}^c}{\bar{\bar{\sigma}}_f} \bar{\bar{\xi}} \right) \right] \tag{2.61}$$

The tangent softening modulus $\bar{\bar{K}}^c$ is computed as the derivative of $\bar{\bar{q}}$

$$\bar{\bar{K}}^c = \frac{d\bar{\bar{q}}}{d\bar{\bar{\xi}}} = -\bar{\bar{\beta}}^c \exp\left(-\frac{\bar{\bar{\beta}}^c}{\bar{\bar{\sigma}}_f} \bar{\bar{\xi}} \right) \tag{2.62}$$

where $\bar{\bar{\beta}}^c$ is a material parameter that controls softening. The value of $\bar{\bar{\beta}}^c$ is inversely proportional to the fracture energy G_f, which represents the area under the softening part of the response, as shown in Figure 2.6. The fracture energy is given in [55] as

$$G_f = \frac{\bar{\bar{\sigma}}_f^2 \, l^e_{\Gamma_s}}{2\,\bar{\bar{\beta}}^c} \tag{2.63}$$

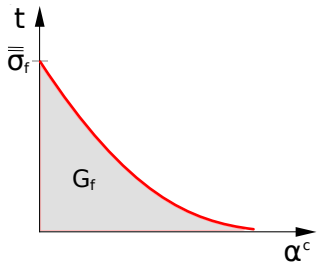

Figure 2.6: Fracture energy G_f represented by the grey area under the softening part of the response.

Elastic trial step

In the first iteration at the discontinuity, we start the computation with all the internal variables at the discontinuity being equal to zero, meaning that the discontinuity surface has not been activated yet (softening has not started)

$$\boldsymbol{\alpha}^c = \mathbf{0}; \quad \bar{\bar{\xi}} = 0; \quad \bar{\bar{q}} = 0; \quad \bar{\bar{\mathbf{Q}}} = \mathbf{0} \tag{2.64}$$

In the case when $\bar{\bar{\mathbf{Q}}} = \mathbf{0}$ and $\boldsymbol{\alpha}^c = \mathbf{0}$, the discontinuity surfaces have not been activated yet, and the continuity of tractions has to be satisfied. So, we compute the

trial value of the traction at the discontinuity by projecting the stress in the bulk to the discontinuity surface Γ_s

$$\mathbf{t}_{n+1}^{trial} = \mathbf{n} \cdot \boldsymbol{\sigma}^{c} = \begin{bmatrix} \sigma_{xx}^{c} n_1 + \tau_{xy}^{c} n_2 \\ \tau_{xy}^{c} n_1 + \sigma_{yy}^{c} n_2 \end{bmatrix} \tag{2.65}$$

The normal and the tangential component of this traction are then

$$t_{1,n+1}^{trial} = \mathbf{t}_{n+1}^{trial} \cdot \mathbf{n} \tag{2.66}$$

$$t_{2,n+1}^{trial} = \mathbf{t}_{n+1}^{trial} \cdot \mathbf{m} \tag{2.67}$$

If $\bar{\bar{\mathbf{Q}}} \neq \mathbf{0}$, this means that both discontinuity surfaces have been activated, and the trial value of traction is computed directly from (2.56)

$$\mathbf{t}_{n+1}^{trial} = \bar{\bar{\mathbf{Q}}}_{n}^{-1} \boldsymbol{\alpha}_{n+1}^{c} \tag{2.68}$$

If we write this by components, we get

$$t_{1,n+1}^{trial} = \frac{\alpha_{1,n+1}^{c}}{\bar{\bar{Q}}_{nn}}; \quad t_{2,n+1}^{trial} = \frac{\alpha_{2,n+1}^{c}}{\bar{\bar{Q}}_{mm}} \tag{2.69}$$

If one discontinuity surface has been activated, and the other not, we compute each component separately, according to equation (2.66) or (2.69), depending on the case.

With the trial value of traction in hand, we have to see if it is admissible. We do that by checking if the damage functions $\bar{\bar{\phi}}$ for each direction are negative or equal to zero [55]

$$\bar{\bar{\phi}}_{1,n+1}^{trial} = \mathbf{t}_{n+1}^{trial} \cdot \mathbf{n} - \left(\bar{\bar{\sigma}}_f - \bar{\bar{q}}_{n+1}^{trial} \right) \tag{2.70}$$

$$\bar{\bar{\phi}}_{2,n+1}^{trial} = |\mathbf{t}_{n+1}^{trial} \cdot \mathbf{m}| - \left(\bar{\bar{\sigma}}_s - \frac{\bar{\bar{\sigma}}_s}{\bar{\bar{\sigma}}_f} \bar{\bar{q}}_{n+1}^{trial} \right) \tag{2.71}$$

The trial value of $\bar{\bar{q}}$ is computed from (2.61)

$$\bar{\bar{q}}_{n+1}^{trial} = \bar{\bar{\sigma}}_f \left[1 - \exp\left(-\frac{\bar{\bar{\beta}}^{c}}{\bar{\bar{\sigma}}_f} \bar{\bar{\xi}}_n \right) \right] \tag{2.72}$$

so the softening in both directions is controlled by one variable, $\bar{\bar{\xi}}$.

Damage step

Depending on the values of the damage functions $\bar{\bar{\phi}}_1^{trial}$ and $\bar{\bar{\phi}}_2^{trial}$, we have four different cases to consider (see Table 2.1), as described in [55].

Table 2.1: Four cases depending on the values of the trial functions $\bar{\bar{\phi}}_1^{trial}$ and $\bar{\bar{\phi}}_2^{trial}$.

	$\bar{\bar{\phi}}_2^{trial} > 0$	$\bar{\bar{\phi}}_2^{trial} \leq 0$
$\bar{\bar{\phi}}_1^{trial} > 0$	case 1	case 2
$\bar{\bar{\phi}}_1^{trial} \leq 0$	case 3	case 4

These are just the four basic cases, and each one of them has sub-cases to consider, depending on the values of $\bar{\bar{Q}}_{nn}$, $\bar{\bar{Q}}_{mm}$, α_1^c, and α_2^c. In case 4, neither of the surfaces is active, so there are no sub-cases to consider.

Since the values of the damage compliance tensor $\bar{\bar{\mathbf{Q}}}$ are taken from the previous time step, and $\boldsymbol{\alpha}^c$ is computed in the current step, it can happen that $\boldsymbol{\alpha}^c \neq \mathbf{0}$, while $\bar{\bar{\mathbf{Q}}} = \mathbf{0}$. This means that the discontinuity surface has just become active, so the damage function $\bar{\bar{\phi}}_i$ for the direction under consideration is larger than zero for sure. In this case, the Lagrange multiplier at the discontinuity is equal to the displacement jump. For each direction separately, we have

$$\bar{\bar{\gamma}}_{1,n+1} = \alpha^c_{1,n+1} \tag{2.73}$$

$$\bar{\bar{\gamma}}_{2,n+1} = \alpha^c_{2,n+1} \tag{2.74}$$

Equation (2.73) accounts for the first appearance of the crack in the normal direction, and equation (2.73) means the same for the tangential direction.

The sub-cases for cases 1, 2 and 3 are described in Tables 2.2 to 2.4.

Table 2.2: Sub-cases for case one, when both surfaces are active: $\bar{\bar{\phi}}_1^{trial} > 0$ and $\bar{\bar{\phi}}_2^{trial} > 0$.

CASE 1	$\bar{\bar{Q}}_{mm} \neq 0$	$\bar{\bar{Q}}_{mm} = 0;\ \alpha_2^c = 0$	$\bar{\bar{Q}}_{mm} = 0;\ \alpha_2^c \neq 0$
$\bar{\bar{Q}}_{nn} \neq 0$	case 1.1	case 1.2	case 1.3
$\bar{\bar{Q}}_{nn} = 0;\ \alpha_1^c = 0$	case 1.4	case 1.5	case 1.6
$\bar{\bar{Q}}_{nn} = 0;\ \alpha_1^c \neq 0$	case 1.7	case 1.8	case 1.9

Still, we have to check which surfaces are really active, because we are updating the Lagrange multipliers $\bar{\bar{\gamma}}_1$ and $\bar{\bar{\gamma}}_2$, which leads to a change in the softening variable

Table 2.3: Sub-cases for case two, when only the normal surface is active: $\bar{\bar{\phi}}_1^{trial} > 0$ and $\bar{\bar{\phi}}_2^{trial} \leq 0$.

CASE 2	$\bar{\bar{Q}}_{mm} \neq 0$	$\bar{\bar{Q}}_{mm} = 0;\ \alpha_2^c = 0$
$\bar{\bar{Q}}_{nn} \neq 0$	case 2.1	case 2.2
$\bar{\bar{Q}}_{nn} = 0;\ \alpha_1^c = 0$	case 2.3	case 2.4
$\bar{\bar{Q}}_{nn} = 0;\ \alpha_1^c \neq 0$	case 2.5	case 2.6

Table 2.4: Sub-cases for case three, when only the tangential surface is active: $\bar{\bar{\phi}}_1^{trial} \leq 0$ and $\bar{\bar{\phi}}_2^{trial} > 0$.

CASE 3	$\bar{\bar{Q}}_{mm} \neq 0$	$\bar{\bar{Q}}_{mm} = 0;\ \alpha_2^c = 0$	$\bar{\bar{Q}}_{mm} = 0;\ \alpha_2^c \neq 0$
$\bar{\bar{Q}}_{nn} \neq 0$	case 3.1	case 3.2	case 3.3
$\bar{\bar{Q}}_{nn} = 0;\ \alpha_1^c = 0$	case 3.4	case 3.5	case 3.6

$\bar{\bar{\xi}}$, and thus changes the value of $\bar{\bar{q}}$. So, the damage functions $\bar{\bar{\phi}}_1^{trial}$ and $\bar{\bar{\phi}}_2^{trial}$ will be updated again, which can lead to the activation or deactivation of a surface during the computation. Each case leads to a subsequent computation (1, 2, 3 or 4), in which the evolution equations of internal variables are solved in the Gauss point, and iterations k are performed until convergence is obtained.

Cases 1.2, 1.3, 2.1, and 2.2 lead to computation 1; cases 1.4, 1.7, 3.1, and 3.4 lead to computation 2; case 1.1 leads to computation 3, while all the other cases lead to computation 4 where the update of the internal variables is performed. The following equations in computations 1, 2, 3, and 4 are taken from [55].

Computation 1

Surface 1 is active, so our goal is to find a value of the Lagrange multiplier $\bar{\bar{\gamma}}_1$ that satisfies the following equation

$$\bar{\bar{\phi}}_1 = 0 \tag{2.75}$$

The initial value of $\bar{\bar{\gamma}}_1$ to enter the iterative procedure ($k = 0$) is then

$$\bar{\bar{\gamma}}_1^0 = \frac{\bar{\bar{\phi}}_1^{trial}}{\bar{\bar{Q}}_{nn}^{-1} + \bar{\bar{K}}^c} \tag{2.76}$$

From the Newton-Raphson procedure, we have

$$\Delta\bar{\bar{\gamma}}_1^{k+1} = -\frac{\bar{\bar{\phi}}_1}{\left(\bar{\bar{\phi}}_1\right)'} \quad \text{where} \quad \bar{\bar{\gamma}}_1^{k+1} = \bar{\bar{\gamma}}_1^{k} + \Delta\bar{\bar{\gamma}}_1^{k+1} \tag{2.77}$$

The damage function can be written as

$$\bar{\bar{\phi}}_1 = \bar{\bar{\phi}}_1^{trial} - \bar{\bar{\gamma}}_1 \bar{\bar{Q}}_{nn}^{-1} + \left(\bar{\bar{q}}_{n+1} - \bar{\bar{q}}_n\right) \tag{2.78}$$

with

$$\left(\bar{\bar{q}}_{n+1} - \bar{\bar{q}}_n\right) = \bar{\bar{\sigma}}_f \exp\left(-\frac{\bar{\bar{\beta}}^c}{\bar{\bar{\sigma}}_f}\bar{\bar{\xi}}_n\right)\left[1 - \exp\left(-\frac{\bar{\bar{\beta}}^c}{\bar{\bar{\sigma}}_f}\bar{\bar{\gamma}}_1\right)\right] \tag{2.79}$$

The derivative of the damage function is then

$$\left(\bar{\bar{\phi}}_1\right)' = \frac{\partial\bar{\bar{\phi}}_1}{\partial\bar{\bar{\gamma}}_1} = -\bar{\bar{Q}}_{nn}^{-1} - \bar{\bar{K}}^c \exp\left(-\frac{\bar{\bar{\beta}}^c}{\bar{\bar{\sigma}}_f}\bar{\bar{\gamma}}_1\right) \tag{2.80}$$

The softening modulus $\bar{\bar{K}}^c$ can be computed from Eq. (2.62)

$$\bar{\bar{K}}^c = \frac{d\bar{\bar{q}}}{d\bar{\bar{\xi}}} = -\bar{\bar{\beta}}^c \exp\left(-\frac{\bar{\bar{\beta}}^c}{\bar{\bar{\sigma}}_f}\bar{\bar{\xi}}_n\right) \tag{2.81}$$

We perform iterations k until convergence is obtained: $|\Delta\bar{\bar{\gamma}}_1| < \text{tol}$, where tol is the predefined tolerance.

Computation 2

Surface 2 is active, so we have a similar procedure as for computation 1, but for the tangential direction. Now, we have to find $\bar{\bar{\gamma}}_2$ that satisfies

$$\bar{\bar{\phi}}_2 = 0 \tag{2.82}$$

The initial value of $\bar{\bar{\gamma}}_2$ to enter iterations k is

$$\bar{\bar{\gamma}}_2^0 = \frac{\bar{\bar{\phi}}_2^{trial}}{\bar{\bar{Q}}_{mm}^{-1} + \bar{\bar{K}}^c\left(\frac{\bar{\bar{\sigma}}_s}{\bar{\bar{\sigma}}_f}\right)^2} \tag{2.83}$$

The damage function $\bar{\bar{\phi}}_2$ and its derivative are then

$$\bar{\bar{\phi}}_2 = \bar{\bar{\phi}}_2^{trial} - \bar{\bar{\gamma}}_2\bar{\bar{Q}}_{mm}^{-1} + \frac{\bar{\bar{\sigma}}_s}{\bar{\bar{\sigma}}_f}\left(\bar{\bar{q}}_{n+1} - \bar{\bar{q}}_n\right) \tag{2.84}$$

$$\left(\bar{\bar{\phi}}_2\right)' = \frac{\partial\bar{\bar{\phi}}_2}{\partial\bar{\bar{\gamma}}_2} = -\bar{\bar{Q}}_{mm}^{-1} - \bar{\bar{K}}^c\left(\frac{\bar{\bar{\sigma}}_s}{\bar{\bar{\sigma}}_f}\right)^2 \exp\left(-\frac{\bar{\bar{\beta}}}{\bar{\bar{\sigma}}_f}\frac{\bar{\bar{\sigma}}_s}{\bar{\bar{\sigma}}_f}\bar{\bar{\gamma}}_2\right) \tag{2.85}$$

Then, we have to update the value of the Lagrange multiplier

$$\bar{\bar{\gamma}}_2^{k+1} = \bar{\bar{\gamma}}_2^{k} + \Delta\bar{\bar{\gamma}}_2^{k+1} \quad \text{where} \quad \Delta\bar{\bar{\gamma}}_2^{k+1} = -\frac{\bar{\bar{\phi}}_2}{\left(\bar{\bar{\phi}}_2\right)'} \tag{2.86}$$

Computation 3

When both surfaces are active, we have to solve

$$\bar{\bar{\phi}}_1 = 0 \tag{2.87}$$

$$\bar{\bar{\phi}}_2 = 0 \tag{2.88}$$

The initial values of $\bar{\bar{\gamma}}_1$ and $\bar{\bar{\gamma}}_2$ to enter iterations k are

$$\bar{\bar{\gamma}}_1^0 = \frac{\bar{\bar{\phi}}_1^{trial}}{\bar{\bar{Q}}_{nn}^{-1} + \bar{\bar{K}}^{\mathrm{c}}} \tag{2.89}$$

$$\bar{\bar{\gamma}}_2^0 = \frac{\bar{\bar{\phi}}_2^{trial}}{\bar{\bar{Q}}_{mm}^{-1} + \bar{\bar{K}}^{\mathrm{c}}\left(\dfrac{\bar{\bar{\sigma}}_s}{\bar{\bar{\sigma}}_f}\right)^2} \tag{2.90}$$

The damage functions are defined as

$$\bar{\bar{\phi}}_1 = \bar{\bar{\phi}}_1^{trial} - \bar{\bar{\gamma}}_1\bar{\bar{Q}}_{nn}^{-1} + \left(\bar{\bar{q}}_{n+1} - \bar{\bar{q}}_n\right) \tag{2.91}$$

$$\bar{\bar{\phi}}_2 = \bar{\bar{\phi}}_2^{trial} - \bar{\bar{\gamma}}_2\bar{\bar{Q}}_{mm}^{-1} + \frac{\bar{\bar{\sigma}}_s}{\bar{\bar{\sigma}}_f}\left(\bar{\bar{q}}_{n+1} - \bar{\bar{q}}_n\right) \tag{2.92}$$

with

$$\left(\bar{\bar{q}}_{n+1} - \bar{\bar{q}}_n\right) = \bar{\bar{\sigma}}_f \exp\left(-\frac{\bar{\bar{\beta}}^{\mathrm{c}}}{\bar{\bar{\sigma}}_f}\bar{\bar{\xi}}_n\right)\left[1 - \exp\left(-\frac{\bar{\bar{\beta}}^{\mathrm{c}}}{\bar{\bar{\sigma}}_f}\left(\bar{\bar{\gamma}}_1 + \frac{\bar{\bar{\sigma}}_s}{\bar{\bar{\sigma}}_f}\bar{\bar{\gamma}}_2\right)\right)\right] \tag{2.93}$$

The derivatives of the damage functions over $\bar{\bar{\gamma}}_1$ and $\bar{\bar{\gamma}}_2$ are

$$d\bar{\bar{\phi}}_{1,1} = \frac{\partial\bar{\bar{\phi}}_1}{\partial\bar{\bar{\gamma}}_1} = -\bar{\bar{Q}}_{nn}^{-1} - \bar{\bar{K}}^{\mathrm{c}}\exp\left(-\frac{\bar{\bar{\beta}}^{\mathrm{c}}}{\bar{\bar{\sigma}}_f}\left(\bar{\bar{\gamma}}_1 + \frac{\bar{\bar{\sigma}}_s}{\bar{\bar{\sigma}}_f}\bar{\bar{\gamma}}_2\right)\right) \tag{2.94}$$

$$d\bar{\bar{\phi}}_{1,2} = \frac{\partial\bar{\bar{\phi}}_1}{\partial\bar{\bar{\gamma}}_2} = -\bar{\bar{K}}^{\mathrm{c}}\frac{\bar{\bar{\sigma}}_s}{\bar{\bar{\sigma}}_f}\exp\left(-\frac{\bar{\bar{\beta}}^{\mathrm{c}}}{\bar{\bar{\sigma}}_f}\left(\bar{\bar{\gamma}}_1 + \frac{\bar{\bar{\sigma}}_s}{\bar{\bar{\sigma}}_f}\bar{\bar{\gamma}}_2\right)\right) \tag{2.95}$$

$$d\bar{\bar{\phi}}_{2,1} = -d\bar{\bar{\phi}}_{1,2} \tag{2.96}$$

$$d\bar{\bar{\phi}}_{2,2} = \frac{\partial\bar{\bar{\phi}}_2}{\partial\bar{\bar{\gamma}}_2} = -\bar{\bar{Q}}_{mm}^{-1} - \bar{\bar{K}}^{\mathrm{c}}\left(\frac{\bar{\bar{\sigma}}_s}{\bar{\bar{\sigma}}_f}\right)^2\exp\left(-\frac{\bar{\bar{\beta}}^{\mathrm{c}}}{\bar{\bar{\sigma}}_f}\left(\bar{\bar{\gamma}}_1 + \frac{\bar{\bar{\sigma}}_s}{\bar{\bar{\sigma}}_f}\bar{\bar{\gamma}}_2\right)\right) \tag{2.97}$$

The update of the Lagrange multipliers is then

$$\bar{\bar{\gamma}}_1^{k+1} = \bar{\bar{\gamma}}_1^{k} + \Delta\bar{\bar{\gamma}}_1^{k+1} \tag{2.98}$$

$$\bar{\bar{\gamma}}_2^{k+1} = \bar{\bar{\gamma}}_2^{k} + \Delta\bar{\bar{\gamma}}_2^{k+1} \tag{2.99}$$

with

$$\Delta\bar{\bar{\gamma}}_1^{k+1} = -\frac{\bar{\bar{\phi}}_1 d\bar{\bar{\phi}}_{2,2} - \bar{\bar{\phi}}_2 d\bar{\bar{\phi}}_{1,2}}{d\bar{\bar{\phi}}_{1,1} d\bar{\bar{\phi}}_{2,2} - d\bar{\bar{\phi}}_{1,2} d\bar{\bar{\phi}}_{2,1}} \tag{2.100}$$

$$\Delta\bar{\bar{\gamma}}_2^{k+1} = -\frac{\bar{\bar{\phi}}_2 d\bar{\bar{\phi}}_{1,1} - \bar{\bar{\phi}}_1 d\bar{\bar{\phi}}_{2,1}}{d\bar{\bar{\phi}}_{1,1} d\bar{\bar{\phi}}_{2,2} - d\bar{\bar{\phi}}_{1,2} d\bar{\bar{\phi}}_{2,1}} \tag{2.101}$$

Computation 4

After convergence is obtained in local iterations k, computations 1, 2 and 3 lead to computation 4, as do the cases that were in which the surfaces were considered rigid from the beginning.

In computation 4, the internal variables are updated by solving the evolution equations from (2.58) with a backward Euler solution scheme. We get

$$\bar{\bar{\xi}}_{n+1} = \bar{\bar{\xi}}_n + \bar{\bar{\gamma}}_1 + \frac{\bar{\bar{\sigma}}_s}{\bar{\bar{\sigma}}_f}\bar{\bar{\gamma}}_2 \tag{2.102}$$

$$\bar{\bar{q}}_{n+1} = \bar{\bar{\sigma}}_f \left[1 - \exp\left(-\frac{\bar{\bar{\beta}}^c}{\bar{\bar{\sigma}}_f}\bar{\bar{\xi}}_{n+1}\right)\right] \tag{2.103}$$

$$\bar{\bar{K}}^c = -\bar{\bar{\beta}}^c \exp\left(-\frac{\bar{\bar{\beta}}^c}{\bar{\bar{\sigma}}_f}\bar{\bar{\xi}}_{n+1}\right) \tag{2.104}$$

$$\bar{\bar{Q}}_{nn,n+1} = \begin{cases} \bar{\bar{Q}}_{nn,n}, & \text{for } t_1 = 0 \\ \bar{\bar{Q}}_{nn,n} + \dfrac{\bar{\bar{\gamma}}_1}{t_1}, & \text{for } t_1 \neq 0 \end{cases} \tag{2.105}$$

$$\bar{\bar{Q}}_{mm,n+1} = \begin{cases} \bar{\bar{Q}}_{mm,n}, & \text{for } t_2 = 0 \\ \bar{\bar{Q}}_{mm,n} + \dfrac{\bar{\bar{\gamma}}_2}{t_2}, & \text{for } t_2 \neq 0 \end{cases} \tag{2.106}$$

and the final value of traction in the normal direction is computed from

$$t_1 = \begin{cases} t_1^{trial}, & \text{when surface 1 is not active} \\ \bar{\bar{\sigma}}_f - \bar{\bar{q}}, & \text{when surface 1 is active} \end{cases} \tag{2.107}$$

and so is the traction in the tangential direction

$$t_2 = \begin{cases} t_2^{trial}, & \text{when surface 2 is not active} \\ \dfrac{\bar{\bar{\sigma}}_s}{\bar{\bar{\sigma}}_f}\left(\bar{\bar{\sigma}}_f - \bar{\bar{q}}\right) * \text{sign}(t_2^{trial}), & \text{when surface 2 is active} \end{cases} \tag{2.108}$$

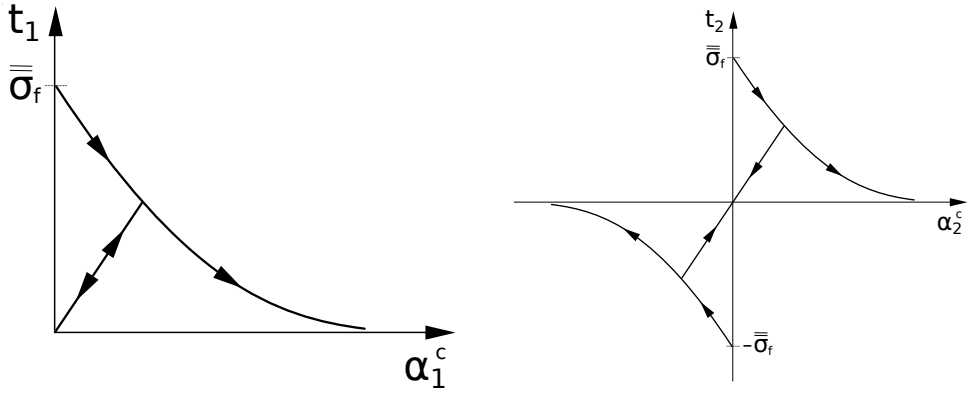

Figure 2.7: Traction at the discontinuity vs. crack opening (displacement jump): (a) normal direction; (b) tangential direction.

The relationship between the traction at the discontinuity and the crack opening for the normal direction is shown on Figure 2.7a, and for the tangential direction on Figure 2.7b. The latter describes the crack sliding in shear, where the sign denotes the direction of the sliding.

The elasto-damage modulus for the discontinuity when both surfaces are active is computed from

$$\bar{\bar{\mathbf{C}}}^{\mathrm{ed}} = \frac{1}{\mathrm{den}} \begin{bmatrix} \bar{\bar{K}}^{\mathrm{c}}_{n+1} & \bar{\bar{K}}^{\mathrm{c}}_{n+1} \frac{\bar{\bar{\sigma}}_s}{\bar{\bar{\sigma}}_f} \mathrm{sign}(t_2) \\ \bar{\bar{K}}^{\mathrm{c}}_{n+1} \frac{\bar{\bar{\sigma}}_s}{\bar{\bar{\sigma}}_f} \mathrm{sign}(t_2) & \bar{\bar{K}}^{\mathrm{c}}_{n+1} \left(\frac{\bar{\bar{\sigma}}_s}{\bar{\bar{\sigma}}_f} \right)^2 \end{bmatrix} \tag{2.109}$$

where den is the denominator that is defined as

$$\mathrm{den} = 1 + \bar{\bar{K}}^{\mathrm{c}}_{n+1} \left[\bar{\bar{Q}}_{nn,n} + \bar{\bar{Q}}_{mm,n} \left(\frac{\bar{\bar{\sigma}}_s}{\bar{\bar{\sigma}}_f} \right)^2 \right] \tag{2.110}$$

When only surface 1 is active, $\bar{\bar{\mathbf{C}}}^{\mathrm{ed}}$ is computed from

$$\bar{\bar{\mathbf{C}}}^{\mathrm{ed}} = \begin{bmatrix} \frac{1}{1+\bar{\bar{K}}^{\mathrm{c}}_{n+1} \bar{\bar{Q}}_{nn,n}} \bar{\bar{K}}^{\mathrm{c}}_{n+1} & 0 \\ 0 & \frac{1}{\bar{\bar{Q}}_{mm,n}} \end{bmatrix} \tag{2.111}$$

and analogously, when only surface 2 is active, it follows

$$\bar{\bar{\mathbf{C}}}^{\mathrm{ed}} = \begin{bmatrix} \frac{1}{\bar{\bar{Q}}_{nn,n}} & 0 \\ 0 & \frac{1}{1+\bar{\bar{K}}^{\mathrm{c}}_{n+1} \bar{\bar{Q}}_{mm,n} \left(\frac{\bar{\bar{\sigma}}_s}{\bar{\bar{\sigma}}_f} \right)^2} \bar{\bar{K}}^{\mathrm{c}}_{n+1} \left(\frac{\bar{\bar{\sigma}}_s}{\bar{\bar{\sigma}}_f} \right)^2 \end{bmatrix} \tag{2.112}$$

Solving the local equation

The final value of traction enters the computation for the residual $\mathbf{h}$ at the discontinuity, defined in (2.16). Now, the local equation (2.20) is solved with a fixed value of the concrete displacement, so $\Delta\mathbf{d}^{\mathrm{c}}_{n+1} = 0$. We compute the crack opening from

$$(\mathbf{H} + \mathbf{K}_{\alpha})\ \Delta\boldsymbol{\alpha}^{\mathrm{c}}_{n+1} = -\mathbf{h}_{n+1} \tag{2.113}$$

With the value of $\boldsymbol{\alpha}^{\mathrm{c}}_{n+1}$ in hand, we can compute the total strain

$$\boldsymbol{\varepsilon}^{\mathrm{c}}_{n+1} = \sum_{a=1}^{n} \mathbf{B}_a\, \mathbf{d}^{\mathrm{c}}_{n+1} + \mathbf{G}_{\mathrm{r}}\, \boldsymbol{\alpha}^{\mathrm{c}}_{n+1} \tag{2.114}$$

from which the final value of stress is obtained

$$\boldsymbol{\sigma}^{\mathrm{c}}_{n+1} = \mathbf{C}^{ed}\, \boldsymbol{\varepsilon}^{\mathrm{c}}_{n+1} \tag{2.115}$$

2.2 Fiber computation

In this work, we are considering the fibers to be linear elastic, seeing that in the experiments we have performed, the complete breaking of the fiber was not a predominant failure mechanism. However, the constitutive law could be easily extended to take into account plasticity, as it can appear on fibers with hooks at their ends (see Figure 2.13).

The stress in the fiber is computed from Hooke's law

$$\sigma^{\mathrm{f}} = E^{\mathrm{f}}\, \varepsilon^{\mathrm{f}} \tag{2.116}$$

where E^{f} is the Young's modulus for steel, and ε^{f} is the strain, computed as

$$\varepsilon^{\mathrm{f}} = \sum_{i=1}^{2} N^{\mathrm{f}}_i d^{\mathrm{f}}_i \tag{2.117}$$

In the above equation, N^{f}_i are the linear shape functions for a truss bar, and d^{f}_i are nodal values of fiber displacements. The area of the fiber is computed as $A^{\mathrm{f}} = \left(\phi^{\mathrm{f}}\right)^2 \pi/4$.

2.3 Interface (bond) treatment

Depending on the type of reinforcement, the activation of slip and the boundary conditions along the fiber change. In standard reinforced concrete, the reinforcement bar is usually anchored in concrete, which means that its ends are fixed, having zero

slip. In addition, the length of the bar makes it difficult to pull it out. The interface between the steel bar and the surrounding concrete is, in this case, described with an elastoplastic law, and the development of a plastic slip is considered. By having its ends fixed, the steel bar has the possibility to remain active and carry load even if a crack in concrete appears along it. In this case, the steel bar itself can reach the plastic phase, and even break.

The bond-slip description presented in this work is very simple, but depicts realistically enough the failure modes on the matrix-fiber interface. Moreover, we do not need to use a special interface element [31, 56, 57, 58] connecting the two components, which allows for an easier numerical implementation. Some authors have opted for a layered description of reinforced concrete, where each layer can represent a different material, as in [18, 59].

Also, we are computing the bond-slip stress in the element directly from the stress-strain diagram, so we do not need to resort to path-following arc-length solution algorithms, such as the ones described in [60] or [61].

2.3.1 Experimental testing of bond-slip

To investigate the behavior on the interface between concrete and the fiber, single-fiber pull-out tests have been performed. A part of these results has been presented in [62]. A numerical simulation of single-fiber pull-out tests can be found in [63].

Figure 2.8: Six specimens containing a fiber: three with 1/4 embedded length, and three with 1/2 embedded length.

Six specimens of dimensions 40x40x80 mm (Figure 2.8) were tested. Each concrete specimen has a steel fiber with hooked ends embedded into it, with the diameter $\phi^{\mathrm{f}} = 0.6$ mm and length $l^{\mathrm{f}} = 30$ mm. The experimental setup and the specimen are shown on Figure 2.9. Three specimens have an embedded length that is equal to one quarter of the fiber length $l^{\mathrm{fe}} = l^{\mathrm{f}}/4 = 7.5$mm, and three specimens have an embedded length equal to one half of the fiber length $l^{\mathrm{fe}} = l^{\mathrm{f}}/2 = 15$mm, as shown in Figure 2.10. The fiber is pulled out of concrete at a speed of 0.005 mm/s.

The concrete mixture is composed of aggregate fractions of 0 - 4 mm, which makes it more like a mortar, which is, in addition, micro-reinforced with short steel fibers of diameter $\phi = 0.2$ mm and length $l = 13$ mm.

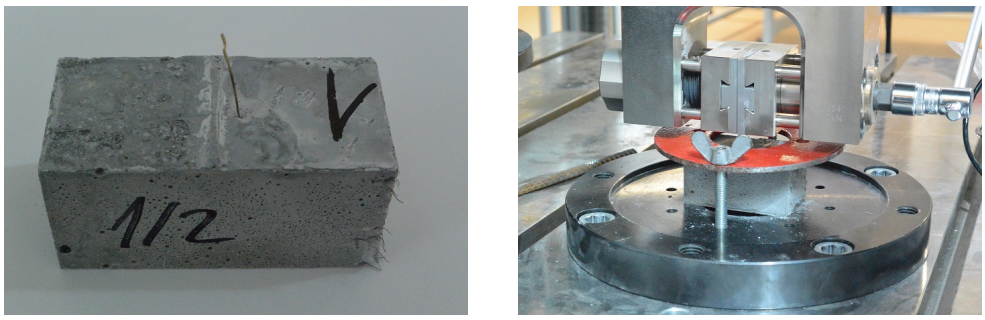

(a) (b)

Figure 2.9: Single-fiber pull-out tests: (a) specimen with embedded fiber; (b) experimental setup.

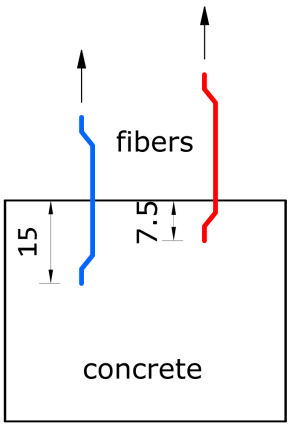

Figure 2.10: Different embedded lengths for the fiber: $l^{fe} = 7.5$ mm (one quarter of the fiber length), and $l^{fe} = 15$ mm (one half of the fiber length).

Force-displacement diagrams for specimens with different embedded lengths are shown on Figure 2.11. We can observe the different shape of the diagrams, with a steep post-peak response for the specimens with 1/4 embedded length (Figure 2.11a). The large area under the curve for the specimens with 1/2 embedded length (Figure 2.11b) shows that more energy was needed to pull out the fiber. This difference is due to different failure mechanisms. In the case of the larger embedded length, after the debonding of the fiber from the matrix, energy is dissipated by frictional effects on the surface, with additional mechanical friction due to the straightening of the hook at the end of the fiber. In the case of the smaller embedded length, the frictional

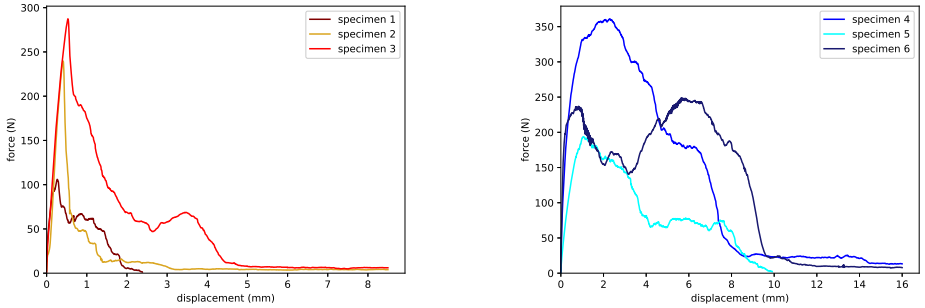

(a) (b)

Figure 2.11: Results for the single-fiber pull-out tests: (a) specimens with 1/4 embedded length; (b) specimens with 1/2 embedded length.

effects do not have time to develop and the fiber pull-out is caused by the failure of concrete around it, without the full straightening of the hook.

Despite the difference in peak pull-out force among the three specimens for a chosen embedded length, the shapes of the graphs are similar. The differences are due to the imperfections in the specimen production, and the imprecise positioning of the fiber inside the specimen. For example, specimen 1 (the red graph) has a very small pull-out force compared to the other two. This is due to the fact that a chunk of material around the fiber hook broke and separated, making room for the fiber to just slip out of the hole, without having to develop the whole set of failure mechanisms on the interface.

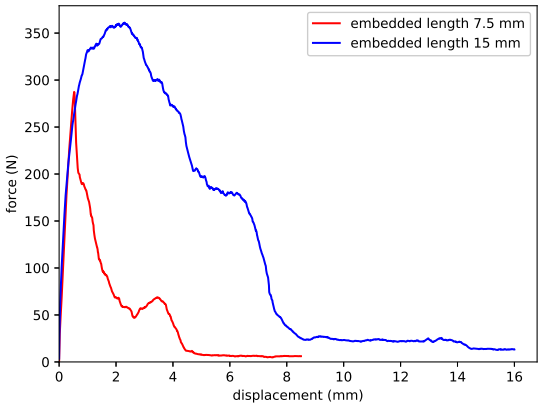

Figure 2.12: Results of single-fiber pull-out tests with different embedded lengths.

To provide a comparison between two different embedded lengths, let's take the two specimens with highest pull-out force from Figure 2.11, for both cases (specimens

3 and 4). The comparison, shown on Figure 2.12, confirms the explanations given above, as the area under the curve is approximately three times larger for the fiber that is half embedded, compared to the one that has just a quarter of its length inside concrete. The peak pull-out force for the specimen with 1/4 embedded length equals $F_{max} = 287.42$ N, while the one for the 1/2 embedded length equals $F_{max} = 361.12$ N.

Figure 2.13 shows a fiber after pull-out. This particular fiber was embedded into the concrete specimen with half its length. The straightening of the hook at the embedded end is clearly visible. This observations will be very useful for the model implementation.

Figure 2.13: Fiber at the end of the analysis, where the straightening of the hook is visible on the pull-out side.

2.3.2 Elasto-plastic model

We start by presenting the treatment of bond-slip through a one-dimensional elasto-plastic computation, that can be applied for standard reinforced concrete, as has been proposed in [64].

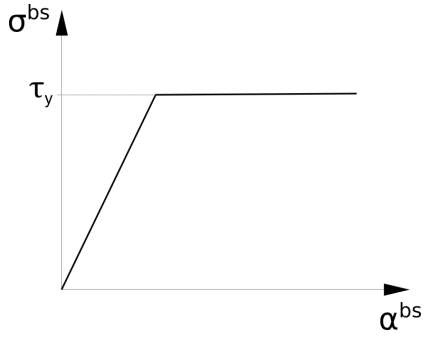

Figure 2.14: Elasto-plastic bond-slip law for standard reinforcement.

The bond-slip law (shown on Figure 2.14) is given as a relationship between the bond stress σ^{bs} and the slip α^{bs}, which is a displacement. That is why instead of the plastic strain ε^{p} that is usually employed in this kind of computations, we will have the plastic slip $\alpha^{bs,p}$. The computation is performed within a 1D plasticity framework,

as it has been described in [65]. Using the operator-split solution procedure, the evolution equations of internal variables are solved in the local phase, on the level of the Gauss numerical integration point of each element, and the equilibrium equations are solved globally, on the level of the whole structure. We start by performing an elastic trial step, in which the plastic multiplier γ^{bs} is equal to zero, and the values of all internal variables are frozen (they take the value from the previous time step)

$$\alpha_{n+1}^{\mathrm{bs,p},trial} = \alpha_n^{\mathrm{bs,p}} \tag{2.118}$$

$$\xi_{n+1}^{\mathrm{bs},trial} = \xi_n^{\mathrm{bs}} \tag{2.119}$$

$$q_{n+1}^{\mathrm{bs},trial} = q_n^{\mathrm{bs}} = -K^{\mathrm{bs,h}} \xi_n^{\mathrm{bs}} \tag{2.120}$$

In the above equations, ξ^{bs} represents the hardening variable, q^{bs} is the stress-like hardening variable for bond-slip, and $K^{\mathrm{bs,h}}$ is the hardening modulus. The trial value of bond stress is then computed as

$$\sigma_{n+1}^{\mathrm{bs},trial} = K^{\mathrm{bs}}(\alpha_{n+1}^{\mathrm{bs}} - \alpha_n^{\mathrm{bs,p}}) \tag{2.121}$$

where K^{bs} is the bond-slip modulus. The term in the brackets represents the elastic slip $\alpha^{\mathrm{bs,el}}$, since the total slip can be represented as the sum of the elastic and the plastic part: $\alpha^{\mathrm{bs}} = \alpha^{\mathrm{bs,el}} + \alpha^{\mathrm{bs,p}}$. The total slip is computed from the nodal values of slip, α_i^{bs}, which are obtained from local iteration of the macro-level computation that will be shown in the next chapter

$$\alpha_{n+1}^{\mathrm{bs}} = \sum_{a=1}^{2} N_a^{\mathrm{bs}} \alpha_{a,n+1}^{\mathrm{bs}} \tag{2.122}$$

The bond-slip shape functions N_i^{bs} are actually the product of the standard shape functions for concrete, and the X-FEM enrichment function ψ. For our case, they are equal to the linear shape functions for a truss bar, $N_a^{\mathrm{bs}} = N_a^{\mathrm{f}}$, as will be explained in section 3.1.1.

To check if the trial value of stress is admissible, we introduce the yield function

$$\phi_{n+1}^{\mathrm{bs},trial} = |\sigma_{n+1}^{\mathrm{bs},trial}| - (\tau_y - q_{n+1}^{\mathrm{bs},trial}) \tag{2.123}$$

where τ_y is the limit value of the bond stress. We have two cases to consider: if the trial value of the yield function is negative or zero, the step is indeed elastic and the trial values are accepted as final. If not, we have to proceed to the plastic step to correct the value of bond stress due to the plastic slip activation.

In the plastic step, we compute a new value for the plastic multiplier

$$\gamma_{n+1}^{\mathrm{bs}} = \frac{\phi_{n+1}^{\mathrm{bs},trial}}{K^{\mathrm{bs}} + K^{\mathrm{bs,h}}} \tag{2.124}$$

which is used to update the internal variables according to

$$\alpha_{n+1}^{\mathrm{bs,p}} = \alpha_n^{\mathrm{bs,p}} + \gamma_{n+1}^{\mathrm{bs}} \operatorname{sign}(\sigma_{n+1}^{\mathrm{bs},trial}) \tag{2.125}$$

$$\xi_{n+1}^{\mathrm{bs}} = \xi_n^{\mathrm{bs}} + \gamma_{n+1}^{\mathrm{bs}} \tag{2.126}$$

The final value of stress is then

$$\sigma_{n+1}^{\mathrm{bs}} = \sigma_{n+1}^{\mathrm{bs},trial} - K^{\mathrm{bs}} \gamma_{n+1}^{\mathrm{bs}} \operatorname{sign}(\sigma_{n+1}^{\mathrm{bs},trial}) \tag{2.127}$$

The elastoplastic tangent modulus in the elastic phase is equal to K^{bs}, and in the plastic phase, it has the value

$$C_{n+1}^{\mathrm{ep,bs}} = \frac{K^{\mathrm{bs}} K^{\mathrm{bs,h}}}{K^{\mathrm{bs}} + K^{\mathrm{bs,h}}} \tag{2.128}$$

2.3.3 Pull-out model

In this section, we present a pull-out bond-slip law, that can be applied for fiber reinforcement. Unlike the reinforcement bar, fibers are short and have a small diameter, and, what is even more important, their ends are not fixed. This leads to a completely different failure mechanism, compared to the one described previously, since the fiber's ends can be pulled out of concrete. We have to change the governing constitutive law to take into account the fiber pull-out as a crucial failure mechanism of the composite.

We assume that concrete and the fiber have a perfect bond until the first crack appears (described by the first, vertical part of the diagram). After that, the bond-slip stress σ^{bs} decreases with the increase of slip α^{bs}. As the bond stress approaches zero, the bond strength is deteriorating, and the influence of the fiber is diminishing, until it gets completely pulled out of concrete.

Linear pull-out law

The behavior at the interface between the steel fiber and the surrounding concrete can be described with a linear pull-out law shown in Fig. 2.15.

The bond-slip stress σ^{bs} can be defined from the diagram

$$\sigma^{\mathrm{bs}} = \left(\tau_y + K^{\mathrm{bs,s}} |\alpha^{\mathrm{bs}}|\right) \operatorname{sign}(\alpha^{\mathrm{bs}}); \quad \text{where} \quad K^{\mathrm{bs,s}} < 0 \tag{2.129}$$

where the value of slip in the Gauss point is computed from (2.122). The diagram for the negative values of σ^{bs} and α^{bs} is equivalent to the one shown in Figure 2.15.

In (2.129), $K^{\mathrm{bs,s}}$ is the bond-slip modulus for the pull-out part of the response (denoted with an "s" as in softening). The value of this modulus can be identified

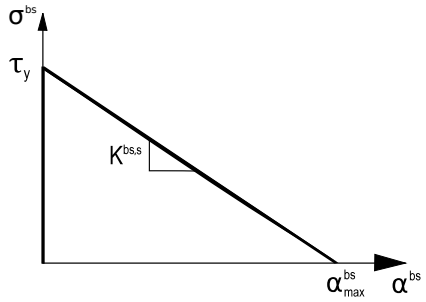

Figure 2.15: Linear bond-slip law for the complete pull-out of the fiber.

from experimental tests, like the ones shown in section 2.3.1, or presented in [66]. The maximal slip can be computed from

$$\alpha^{\mathrm{bs}}_{max} = -\frac{\tau_y}{K^{\mathrm{bs,s}}} \tag{2.130}$$

and when this value is reached, the bond stress equals zero. This can lead to problems in the model implementation, since the sign of the bond stress changes after this point, which is not in accordance with the physical processes happening on the interface. That is why we have to introduce a condition to handle the situation when in a particular element $\alpha^{\mathrm{bs}} = \alpha^{\mathrm{bs}}_{max}$, meaning that complete pull-out has taken place. Then, the influence of the fiber and bond-slip in that element is no longer taken into account in subsequent computations.

The bond-slip area is defined as the surface of the fiber that is in contact with the surrounding concrete, $A^{\mathrm{bs}} = \phi^{\mathrm{f}}\,\pi$, where ϕ^{f} is the fiber diameter.

Exponential pull-out law

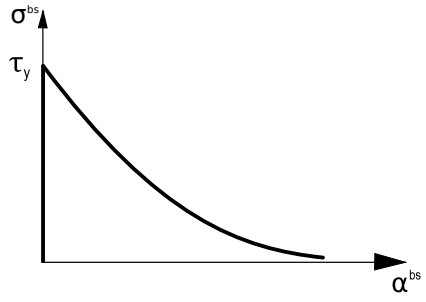

Figure 2.16: Exponential bond-slip law for the complete pull-out of the fiber.

To avoid complications regarding the introducing of a special condition when the stress reaches zero in the linear pull-out law, we describe the pull-out with an exponential function shown on Figure 2.16. Since it is getting close to zero, but

never reaches it, it provides a good way to handle pull-out. The exponential pull-out law is described with the following equation

$$\sigma^{\text{bs}} = \left[\tau_y - \tau_y\left(1 - \exp\left(-\beta^{\text{bs}}|\alpha^{\text{bs}}|\right)\right)\right] \text{sign}(\alpha^{\text{bs}}) \tag{2.131}$$

where β^{bs} is the parameter that controls the pull-out part of the response. The area under the curve on Figure 2.16 represents the energy needed to pull out the fiber completely.

The tangent modulus is equal to the derivative of the bond stress with respect to the slip, and in this case is equal to

$$C^{\text{bs}} = -\tau_y\, \beta^{\text{bs}}\, \exp\left(-\beta^{\text{bs}}|\alpha^{\text{bs}}|\right) \text{sign}(\alpha^{\text{bs}}) \tag{2.132}$$

This completes the description of the models for the composite's constituents, and we can proceed to the multi-scale framework.

3

Multi-scale framework for modeling fiber-reinforced composites

Contents

In this chapter we propose a multi-scale approach to handle the interaction between the fiber, concrete, and bond-slip. The micro-scale computations for each constituent that are presented in the previous chapter, are coupled on the macro-scale through an operator split solution procedure. The governing equations are derived from a displacement field approximation based on the X-FEM methodology. The details of the numerical implementation are shown, together with the comparison between a monolithic and a partitioned solution procedure. Applications to standard reinforcement and fiber reinforcement are presented in several numerical examples.

3.1 Model formulation

3.1.1 Displacement field approximation

In fiber-reinforced concrete, short fibers are randomly distributed throughout the domain, which leads to a problem of non-conforming meshes, as can be seen in Fig. 3.1a. It is obvious that one fiber can pass through multiple finite elements, which we can take into account by using the extended finite element method (X-FEM) [26]. The latter is based on the partition of unity principle $\sum_{a=1}^{n} N_a(\mathbf{x}) = 1$ over the domain Ω, a condition that standard shape functions naturally satisfy [24].

In Figure 3.1, white elements represent the standard concrete elements, while the grey ones are enriched elements with additional degrees of freedom in every node, accounting for the fiber influence inside the domain. In this way, the bond-slip along the fiber-matrix interface has a global representation, and its continuity is preserved through all the elements containing the fiber.

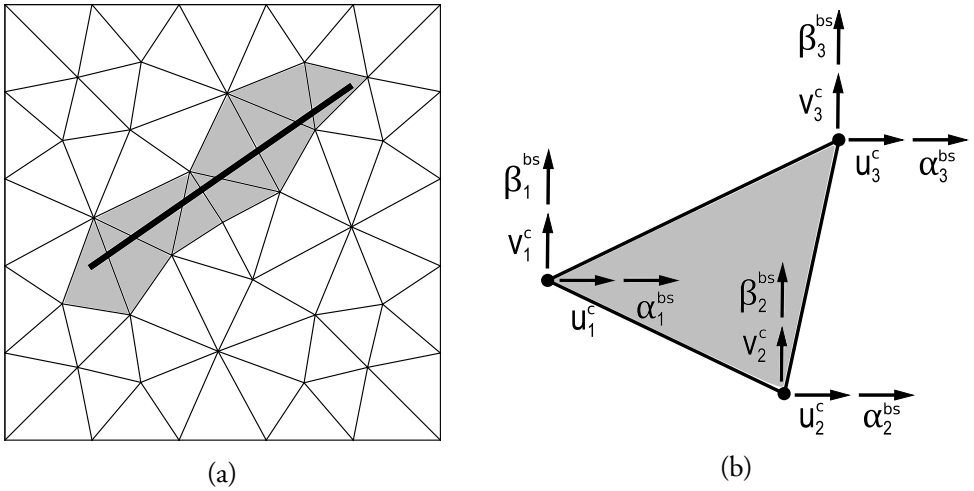

(a) (b)

Figure 3.1: Non-conforming mesh: (a) a randomly oriented fiber in the domain; (b) degrees of freedom of a fully enriched element.

In X-FEM, the displacement field $\mathbf{u}(\mathbf{x})$ can be represented as a sum of the standard and the enriched part

$$\begin{aligned}\mathbf{u}(\mathbf{x})|_{\Omega^e} &= \sum_{a=1}^{n} N_a(\mathbf{x}) \left(\mathbf{d}_a^{\mathrm{c}} + \psi(\mathbf{x})\, \boldsymbol{\alpha}_a^{\mathrm{bs}} \right) \\ &= \sum_{a=1}^{n} N_a(\mathbf{x})\, \mathbf{d}_a^{\mathrm{c}} + \sum_{a=1}^{n} N_a(\mathbf{x}) \psi(\mathbf{x})\, \boldsymbol{\alpha}_a^{\mathrm{bs}} \end{aligned} \tag{3.1}$$

where $\mathbf{d}_a^{\mathrm{c}}$ are standard degrees of freedom (concrete displacements), $\boldsymbol{\alpha}_a^{\mathrm{bs}}$ are enriched degrees of freedom (bond-slip displacements), $N_a(\mathbf{x})$ are standard isoparametric shape

functions for the triangular element ($n = 3$), and $\psi(\mathbf{x})$ is an enrichment function that accounts for the presence of the fiber inside the domain. The product $N_a(\mathbf{x})\psi(\mathbf{x})$ represents local enrichment functions that describe the part of the bond-slip field related to each element. Basically, the X-FEM methodology allows us to keep the global representation of bond-slip, by coupling all concrete elements along each fiber, without changing the standard finite element framework.

The bond-slip is defined as the relative displacement between the fiber and concrete

$$\boldsymbol{\alpha}^{\mathrm{bs}} = \mathbf{d}^{\mathrm{f}} - \mathbf{d}^{\mathrm{c}} \tag{3.2}$$

where the displacement vectors have the following form

$$\boldsymbol{\alpha}_a^{\mathrm{bs}} = \begin{bmatrix} \alpha_a^{\mathrm{bs}} \\ \beta_a^{\mathrm{bs}} \end{bmatrix}, \qquad \mathbf{d}_a^{\mathrm{c}} = \begin{bmatrix} u_a^{\mathrm{c}} \\ v_a^{\mathrm{c}} \end{bmatrix}, \qquad \mathbf{d}_a^{\mathrm{f}} = \begin{bmatrix} u_a^{\mathrm{f}} \\ v_a^{\mathrm{f}} \end{bmatrix}, \tag{3.3}$$

If we consider a case when the fiber is parallel to the x-axis and coincides with the elements' edges, as shown in Fig. 3.2, the number of enriched degrees of freedom is reduced from six to two, allowing us to simplify the formulation for the sake of clarity in explaining the methodology used. Now, only the first two nodes are enriched, and each one of them has just one additional degree of freedom α_a^{bs}. In this case, the enrichment function ψ is taken to be the Heaviside function, which is equal to one in the elements where the fiber is located, and equal to zero in the rest of the domain. For each element, we have

$$\psi(\mathbf{x}) = H(y) = \begin{cases} 1, & y \geq \bar{y} \\ 0, & y < \bar{y} \end{cases} \tag{3.4}$$

where $\bar{y}$ is the location of the fiber.

By exploiting the properties of the Heaviside function, we get

$$N_a(\mathbf{x})\psi(\mathbf{x}) = N_a(\mathbf{x})H(y) = N_a(x, 0) = N_a(x) \tag{3.5}$$

where $N_a(x)$ are the linear shape functions for a truss bar element. So, Eq. (3.1) can be simplified

$$\mathbf{u}(\mathbf{x})|_{\Omega^e} = \sum_{a=1}^{3} N_a(\mathbf{x})\, \mathbf{d}_a^{\mathrm{c}} + \sum_{a=1}^{2} N_a(x)\, \alpha_a^{\mathrm{bs}} \tag{3.6}$$

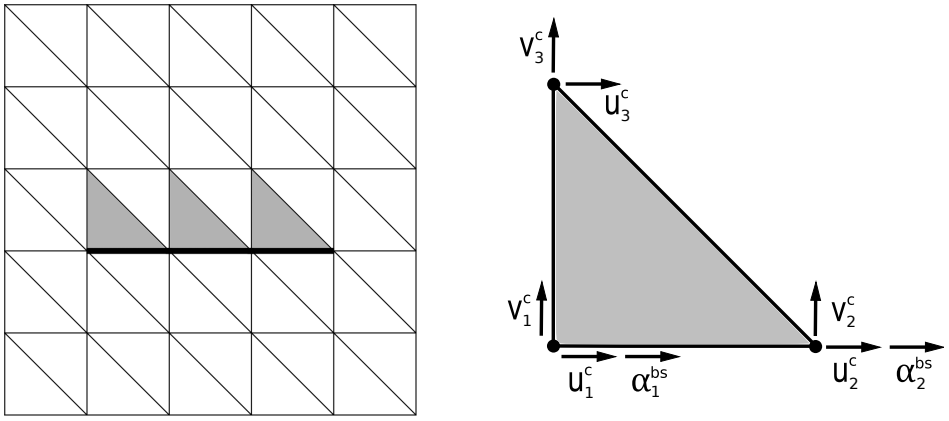

(a) (b)

Figure 3.2: Conforming mesh: (a) the fiber coincides with elements' edges; (b) degrees of freedom of a partially enriched element.

3.1.2 Principle of virtual work

To be able to handle the influence of the fiber inside the domain, we have to look closely at the behavior of the composite and its failure mechanisms that are depicted in Figure 3.3. In the elastic phase (Figure 3.3a), concrete and fiber move together, and since they remain mutually constrained (having the same displacement), bond-slip is not active. In this case, we can take into account only the standard part of the displacement field, and compute the fiber contribution to stiffness by using the constraint to enforce equality between concrete and fiber displacement with zero slip. Only when concrete starts to crack (Figure 3.3b), the bond-slip becomes active, and concrete and fiber will no longer have the same displacements. Hence, we have to take into account the enriched part of the displacement field as well.

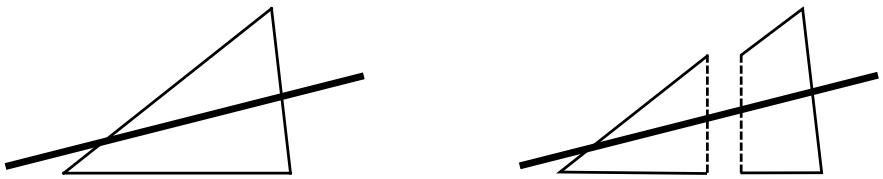

(a) (b)

Figure 3.3: Two phases of the composite behavior: (a) uncracked state; (b) cracked state.

By separating the contribution of standard and enriched degrees of freedom, the computation is divided into two phases: in the first (global) phase, we will take into account the influence of the concrete, the fiber and the external forces, and in the second (local) phase we will compute the redistribution of slip, with the fiber and bond-slip influence. The fiber is the only one that contributes to both phases, thus

representing the coupling term between them. By following the notation in [30], we will denote the first phase with the superscript $^{\text{cf}}$ (concrete + fiber), and the second phase with $^{\text{fbs}}$ (fiber + bond-slip).

From the principle of virtual work, as in (2.10), we have

$$G^{\text{int}} - G^{\text{ext}} = 0 \tag{3.7}$$

The virtual work of internal forces is defined as

$$G^{\text{int}} = \int_{\Omega} \nabla^{\text{s}} \mathbf{w}\, \boldsymbol{\sigma}\, d\Omega \tag{3.8}$$

where $\mathbf{w}$ represents the virtual displacement field that has a standard and an enriched part, as in (3.6)

$$\mathbf{w}(\mathbf{x})|_{\Omega^e} = \sum_{a=1}^{3} N_a(\mathbf{x})\, \mathbf{w}_a^{\text{c}} + \sum_{a=1}^{2} N_a(x)\, w_a^{\text{bs}} \tag{3.9}$$

In the above equation, $\mathbf{w}_a^{\text{c}}$ are virtual concrete displacements, and w_a^{bs} are virtual bond-slip displacements.

The virtual work of external forces is defined as

$$G^{\text{ext}} = \int_{\Omega} \mathbf{w}\, \mathbf{b}\, d\Omega + \int_{\Gamma_\sigma} \mathbf{w}\, \mathbf{t}_{\Gamma_\sigma}\, d\Gamma_\sigma \tag{3.10}$$

By inserting (3.8) and (3.10) into (3.7), we obtain the weak form of the governing boundary value problem

$$\int_{\Omega} \nabla^{\text{s}} \mathbf{w}\, \boldsymbol{\sigma}\, d\Omega - \int_{\Omega} \mathbf{w}\, \mathbf{b}\, d\Omega - \int_{\Gamma_\sigma} \mathbf{w}\, \mathbf{t}_{\Gamma_\sigma}\, d\Gamma_\sigma = 0 \tag{3.11}$$

Since we assume that all the external loads are applied through concrete, for the virtual work of external forces we use only the standard part of the virtual displacement field (3.9), with no enrichment

$$G^{\text{ext}} = \int_{\Omega} \sum_{a=1}^{3} N_a(\mathbf{x})\, \mathbf{w}_a^{\text{c}}\, \mathbf{b}\, d\Omega + \int_{\Gamma_\sigma} \sum_{a=1}^{3} N_a(\mathbf{x})\, \mathbf{w}_a^{\text{c}}\, \mathbf{t}_{\Gamma_\sigma}\, d\Gamma_\sigma \tag{3.12}$$

We can write the above equation as

$$G^{\text{ext}} = \sum_{a=1}^{3} \mathbf{w}_a^{\text{c}}\, \mathbf{f}_a^{\text{ext}} \tag{3.13}$$

where $\mathbf{f}_a^{\text{ext}}$ is the external force vector that is equal to

$$\mathbf{f}_a^{\text{ext}} = \int_\Omega N_a(\mathbf{x})\,\mathbf{b}\,d\Omega + \int_{\Gamma_\sigma} N_a(\mathbf{x})\,\mathbf{t}_{\Gamma_\sigma}\,d\Gamma_\sigma \tag{3.14}$$

For the virtual work of internal forces, we need both the standard and the enriched part of the displacement field approximation, since all three constituents have to be taken into account. By introducing (3.9) into (3.8), we get

$$G^{\text{int}} = \int_\Omega \nabla^s \Big(\sum_{a=1}^{3} N_a(\mathbf{x})\,\mathbf{w}_a^{\text{c}} + \sum_{a=1}^{2} N_a(x)\,w_a^{\text{bs}} \Big) \boldsymbol{\sigma}\,d\Omega \tag{3.15}$$

The enriched part of the finite element discretization is defined only along the fiber domain Γ_{f}, so we can separate Eq. (3.15) into two domains of integration

$$G^{\text{int}} = \int_\Omega \sum_{a=1}^{3} \nabla^s N_a(\mathbf{x})\,\mathbf{w}_a^{\text{c}}\,\boldsymbol{\sigma}\,d\Omega + \int_{\Gamma_{\text{f}}} \sum_{a=1}^{2} \frac{d}{dx} N_a(x) w_a^{\text{bs}}\,\sigma A\,d\Gamma_{\text{f}} \tag{3.16}$$

where the operator nabla in the second integral becomes the derivative along the fiber domain d/dx, the stress value becomes a scalar, and A represents the area of the fiber. We can write

$$G^{\text{int}} = \sum_{a=1}^{3} \mathbf{w}_a^{\text{c}}\,\mathbf{f}_a^{\text{cf,int}} + \sum_{a=1}^{2} w_a^{\text{bs}}\,f_a^{\text{fbs,int}} \tag{3.17}$$

The internal force vectors in (3.17) are defined as

$$\mathbf{f}_a^{\text{cf,int}} = \int_\Omega \nabla^s N_a(\mathbf{x})\,\boldsymbol{\sigma}\,dA \tag{3.18}$$

$$f_a^{\text{fbs,int}} = \int_{\Gamma_{\text{f}}} \frac{d}{dx} N_a(x)\sigma A\,dx \tag{3.19}$$

By putting (3.12) and (3.17) back into (3.7), we obtain

$$\sum_{a=1}^{3} \mathbf{w}_a^{\text{c}}\,\mathbf{f}_a^{\text{cf,int}} + \sum_{a=1}^{2} w_a^{\text{bs}}\,f_a^{\text{fbs,int}} - \sum_{a=1}^{3} \mathbf{w}_a^{\text{c}}\,\mathbf{f}_a^{\text{ext}} = 0 \tag{3.20}$$

which we can split into two equations by grouping together the terms related to $\mathbf{w}_a^{\text{c}}$, and the ones related to w_a^{bs}

$$\begin{aligned} \sum_{a=1}^{3} \mathbf{w}_a^{\text{c}} \Big(\mathbf{f}_a^{\text{cf,int}} - \mathbf{f}_a^{\text{ext}} \Big) = 0 \\ \sum_{a=1}^{2} w_a^{\text{bs}}\,f_a^{\text{fbs,int}} = 0 \end{aligned} \tag{3.21}$$

The global equation is obtained from the standard part of the displacement field, and the local equation is obtained from the enriched part. Since the virtual displacements are arbitrary, the above set of equations (3.21) can be written as

$$\begin{aligned} \mathbf{f}_a^{\text{cf,int}} - \mathbf{f}_a^{\text{ext}} &= 0 \\ f_a^{\text{fbs,int}} &= 0 \end{aligned} \tag{3.22}$$

The global internal force vector is composed of the concrete and the fiber part, while the local internal force vector has the fiber and the bond-slip contribution

$$\mathbf{f}_a^{\text{cf,int}} = \mathbf{f}_a^{\text{c,int}} + f_a^{\text{f,int}} \tag{3.23}$$

$$f_a^{\text{fbs,int}} = f_a^{\text{f,int}} + f_a^{\text{bs,int}} \tag{3.24}$$

where

$$\mathbf{f}_a^{\text{c,int}} = \int_\Omega \nabla^s N_a(\mathbf{x})\, \boldsymbol{\sigma}^c \, dA \tag{3.25}$$

$$f_a^{\text{f,int}} = \int_{\Gamma_\text{f}} \frac{d}{dx} N_a(x)\, \sigma^\text{f} A^\text{f} dx \tag{3.26}$$

$$f_a^{\text{bs,int}} = \int_{\Gamma_\text{f}} \frac{d}{dx} N_a(x) \sigma^{bs} A^{bs} dx \tag{3.27}$$

Now that the internal force vectors are defined, we can write the equilibrium for the whole structure by assembling the contributions from the standard (n) and the enriched elements (n_en).

- **Global equation:** concrete, fiber & external force contribution

$$\mathbf{r}^\text{cf} = \mathop{\mathbb{A}}_{e=1}^{n} \mathbf{f}^{\text{c,int},e} + \mathop{\mathbb{A}}_{e=1}^{n_\text{en}} \mathbf{f}^{\text{f,int,gl},e} - \mathbf{f}^\text{ext} = \mathbf{0} \tag{3.28}$$

- **Local equation:** fiber & bond-slip contribution

$$\mathbf{r}^\text{fbs} = \mathop{\mathbb{A}}_{e=1}^{n_\text{en}} \left(\mathbf{f}^{\text{f,int,loc},e} + \mathbf{f}^{\text{bs,int},e} \right) = \mathbf{0} \tag{3.29}$$

3.1.3 Linearization and operator-split solution procedure

Since Eqs. (3.28) and (3.29) are nonlinear, an incremental and iterative solution procedure is employed, and the pseudo-time parameter t is introduced. By linearizing (3.28 - 3.29) around the displacement values at time t_{n+1} we obtain the following

system of equations, where the unknowns are the incremental values of $\mathbf{d}^{\mathrm{c}}_{n+1}$ and $\boldsymbol{\alpha}^{\mathrm{bs}}_{n+1}$ at time t_{n+1}

$$\begin{bmatrix} \mathbf{K}^{\mathrm{cf}} & \mathbf{F}^{\mathrm{cf}} \\ \mathbf{F}^{\mathrm{fbs}} & \mathbf{H}^{\mathrm{fbs}} \end{bmatrix} \begin{bmatrix} \Delta\mathbf{d}^{\mathrm{c}}_{n+1} \\ \Delta\boldsymbol{\alpha}^{\mathrm{bs}}_{n+1} \end{bmatrix} = - \begin{bmatrix} \mathbf{r}^{\mathrm{cf}}_{n+1} \\ \mathbf{r}^{\mathrm{fbs}}_{n+1} \end{bmatrix} \tag{3.30}$$

where the tangent stiffness matrices are defined as

$$\mathbf{K}^{\mathrm{cf}} = \frac{\partial \mathbf{r}^{\mathrm{cf}}}{\partial \mathbf{d}^{\mathrm{c}}} = \mathbf{K}^{\mathrm{c}} + \mathbf{K}^{\mathrm{f}} = \hat{\mathbf{K}}^{\mathrm{c}} + \int_{\Gamma_{\mathrm{f}}} \mathbf{B}^{\mathrm{f},T} E^{\mathrm{f}} A^{\mathrm{f}} \mathbf{B}^{\mathrm{f}} \, dx \tag{3.31}$$

$$\mathbf{F}^{\mathrm{cf}} = \frac{\partial \mathbf{r}^{\mathrm{cf}}}{\partial \boldsymbol{\alpha}^{\mathrm{bs}}} = \int_{\Gamma_{\mathrm{f}}} \mathbf{B}^{\mathrm{f},T} E^{\mathrm{f}} A^{\mathrm{f}} \mathbf{B}^{\mathrm{f}} \, dx \tag{3.32}$$

$$\mathbf{F}^{\mathrm{fbs}} = \frac{\partial \mathbf{r}^{\mathrm{fbs}}}{\partial \mathbf{d}^{\mathrm{c}}} = \mathbf{F}^{\mathrm{cf}} \tag{3.33}$$

$$\mathbf{H}^{\mathrm{fbs}} = \frac{\partial \mathbf{r}^{\mathrm{fbs}}}{\partial \boldsymbol{\alpha}^{\mathrm{bs}}} = \mathbf{H}^{\mathrm{f}} + \mathbf{H}^{\mathrm{bs}} = \int_{\Gamma_{\mathrm{f}}} \mathbf{B}^{\mathrm{f},T} E^{\mathrm{f}} A^{\mathrm{f}} \mathbf{B}^{\mathrm{f}} \, dx + \int_{\Gamma_{\mathrm{f}}} \mathbf{B}^{\mathrm{f},T} C^{\mathrm{bs}} A^{\mathrm{bs}} \mathbf{B}^{\mathrm{f}} \, dx \tag{3.34}$$

In the above equations, $\mathbf{B}^{\mathrm{c}}$ denotes the shape functions for concrete, and $\mathbf{B}^{\mathrm{f}}$ the shape functions for the fiber. $\hat{\mathbf{K}}^{\mathrm{c}}$ is the condensed stiffness matrix for concrete obtained from (2.27).

The system of equations (3.30) can be solved simultaneously, but since both the computations for concrete and for bond-slip are nonlinear, it is more suitable to solve them sequentially, using the operator-split solution procedure. From (3.30), we have

$$\mathbf{K}^{\mathrm{cf}} \Delta\mathbf{d}^{\mathrm{c}}_{n+1} + \mathbf{F}^{\mathrm{cf}} \Delta\boldsymbol{\alpha}^{\mathrm{bs}}_{n+1} = -\mathbf{r}^{\mathrm{cf}}_{n+1} \tag{3.35}$$

$$\mathbf{F}^{\mathrm{fbs}} \Delta\mathbf{d}^{\mathrm{c}}_{n+1} + \mathbf{H}^{\mathrm{fbs}} \Delta\boldsymbol{\alpha}^{\mathrm{bs}}_{n+1} = -\mathbf{r}^{\mathrm{fbs}}_{n+1} \tag{3.36}$$

From (3.36), we can express the increment of the bond-slip displacement

$$\Delta\boldsymbol{\alpha}^{\mathrm{bs}}_{n+1} = -(\mathbf{H}^{\mathrm{fbs}})^{-1} \left(\mathbf{r}^{\mathrm{fbs}}_{n+1} + \mathbf{F}^{\mathrm{fbs}} \Delta\mathbf{d}^{\mathrm{c}}_{n+1} \right) \tag{3.37}$$

and introduce it into (3.36)

$$\mathbf{K}^{\mathrm{cf}} \Delta\mathbf{d}^{\mathrm{c}}_{n+1} - \mathbf{F}^{\mathrm{cf}} (\mathbf{H}^{\mathrm{fbs}})^{-1} \left(\mathbf{r}^{\mathrm{fbs}}_{n+1} + \mathbf{F}^{\mathrm{fbs}} \Delta\mathbf{d}^{\mathrm{c}}_{n+1} \right) = -\mathbf{r}^{\mathrm{cf}}_{n+1} \tag{3.38}$$

Since we are solving the global equation (3.38) for a fixed value of bond-slip, the local residual is equal to zero, $\mathbf{r}^{\mathrm{fbs}}_{n+1} = \mathbf{0}$. Then, it follows

$$\mathbf{K}^{\mathrm{cf}} \Delta\mathbf{d}^{\mathrm{c}}_{n+1} - \mathbf{F}^{\mathrm{cf}} (\mathbf{H}^{\mathrm{fbs}})^{-1} \mathbf{F}^{\mathrm{fbs}} \Delta\mathbf{d}^{\mathrm{c}}_{n+1} = -\mathbf{r}^{\mathrm{cf}}_{n+1} \tag{3.39}$$

that can be written as

$$\tilde{\mathbf{K}} \, \Delta\mathbf{d}^{\mathrm{c}}_{n+1} = -\mathbf{r}^{\mathrm{cf}}_{n+1} \tag{3.40}$$

where $\tilde{\mathbf{K}}$ is the condensed stiffness matrix

$$\tilde{\mathbf{K}} = \mathbf{K}^{\mathrm{cf}} - \mathbf{F}^{\mathrm{cf}}(\mathbf{H}^{\mathrm{fbs}})^{-1}\mathbf{F}^{\mathrm{fbs}} \tag{3.41}$$

Equation (3.36) is solved with a fixed value of concrete displacement $\Delta\mathbf{d}^{\mathrm{c}}_{n+1} = \mathbf{0}$, so the local equation becomes

$$\mathbf{H}^{\mathrm{fbs}}\Delta\boldsymbol{\alpha}^{\mathrm{bs}}_{n+1} = -\mathbf{r}^{\mathrm{fbs}}_{n+1} \tag{3.42}$$

The system of equations to solve sequentially is then

$$\begin{aligned} \tilde{\mathbf{K}}\,\Delta\mathbf{d}^{\mathrm{c}}_{n+1} &= -\mathbf{r}^{\mathrm{cf}}_{n+1} \\ \mathbf{H}^{\mathrm{fbs}}\Delta\boldsymbol{\alpha}^{\mathrm{bs}}_{n+1} &= -\mathbf{r}^{\mathrm{fbs}}_{n+1} \end{aligned} \tag{3.43}$$

The computation is performed in the following manner: we start by solving the first equation in (3.43), from which the concrete displacements are obtained

$$\mathbf{d}^{\mathrm{c}}_{n+1} = \mathbf{d}^{\mathrm{c}}_{n} + \Delta\mathbf{d}^{\mathrm{c}}_{n+1} \tag{3.44}$$

When convergence is obtained for the global equation, we proceed to solving the second equation in (3.43), from which we obtain the bond-slip displacements

$$\boldsymbol{\alpha}^{\mathrm{bs}}_{n+1} = \boldsymbol{\alpha}^{\mathrm{bs}}_{n} + \Delta\boldsymbol{\alpha}^{\mathrm{bs}}_{n+1} \tag{3.45}$$

When convergence is obtained, we proceed to the next time step.

3.2 Numerical implementation

The proposed formulation is implemented in the computer program *FEAP - Finite Element Analysis Program* [44], developed by R.L. Taylor at UC Berkeley.

The response and failure modes' activation for all three components – concrete, steel, and bond-slip – are handled within a single encapsulated triangular element. That means that the stiffness matrices and residuals are assembled from the element contributions of all three parts. One of the advantages of using the operator-split solution procedure, is the handling of systems of equations of different sizes. Namely, on the element level, the displacement vector for concrete $\Delta\mathbf{d}^{\mathrm{c}}$ and the residual for the global part $\mathbf{r}^{\mathrm{cf}}$ in the first equation in (3.43), are of size [6x1], while the displacement vector for bond-slip $\Delta\boldsymbol{\alpha}^{\mathrm{bs}}$ and the residual for the local part $\mathbf{r}^{\mathrm{fbs}}$ in the second equation in (3.43), are of size [2x1]. The stiffness matrix for concrete $\mathbf{K}^{\mathrm{c}}$ is of size [6x6], while the other matrices, $\mathbf{K}^{\mathrm{f}}$, $\mathbf{F}^{\mathrm{cf}}$, $\mathbf{F}^{\mathrm{fbs}}$, $\mathbf{H}^{\mathrm{f}}$, and $\mathbf{H}^{\mathrm{bs}}$, are of size [2x2]. Special care has to be taken when assigning the fiber contributions to the right places in the global stiffness matrix and residual, since the fiber acts only in nodes 1 and 2 of the element,

in x-direction. This means that the fiber contributes only to positions $(1,1)$, $(1,3)$, $(3,1)$ and $(3,3)$ of the matrix $\mathbf{K}^{\mathrm{cf}}$, and to positions $(1,1)$ and $(3,1)$ of the residual $\mathbf{r}^{\mathrm{cf}}$. A similar process has to be employed when computing the fiber and bond-slip contributions in the condensed stiffness matrix $\tilde{\mathbf{K}}$. A graphical representation of the concrete, fiber, and bond-slip arrays on the element level is shown here, where $\times$ stands for a non-zero value.

$$\mathbf{f}^{\mathrm{c,int}} = \begin{bmatrix} \times \\ \times \\ \times \\ \times \\ \times \\ \times \end{bmatrix}; \quad \mathbf{f}^{\mathrm{f,int}} = \begin{bmatrix} \times \\ 0 \\ \times \\ 0 \\ 0 \\ 0 \end{bmatrix}; \quad \Delta\mathbf{d}^{\mathrm{c}} = \begin{bmatrix} \times \\ \times \\ \times \\ \times \\ \times \\ \times \end{bmatrix}; \quad \mathbf{r}^{\mathrm{fbs}} = \begin{bmatrix} \times \\ \times \end{bmatrix}; \quad \Delta\boldsymbol{\alpha}^{\mathrm{bs}} = \begin{bmatrix} \times \\ \times \end{bmatrix}$$

$$\mathbf{K}^{\mathrm{c}} = \begin{bmatrix} \times & \times & \times & \times & \times & \times \\ \times & \times & \times & \times & \times & \times \\ \times & \times & \times & \times & \times & \times \\ \times & \times & \times & \times & \times & \times \\ \times & \times & \times & \times & \times & \times \\ \times & \times & \times & \times & \times & \times \end{bmatrix}; \quad \mathbf{K}^{\mathrm{f}} = \begin{bmatrix} \times & 0 & \times & 0 & 0 & 0 \\ 0 & 0 & 0 & 0 & 0 & 0 \\ \times & 0 & \times & 0 & 0 & 0 \\ 0 & 0 & 0 & 0 & 0 & 0 \\ 0 & 0 & 0 & 0 & 0 & 0 \\ 0 & 0 & 0 & 0 & 0 & 0 \end{bmatrix}$$

$$\mathbf{F}^{\mathrm{cf}} = \begin{bmatrix} \times & \times \\ \times & \times \end{bmatrix}; \quad \mathbf{F}^{\mathrm{fbs}} = \begin{bmatrix} \times & \times \\ \times & \times \end{bmatrix}; \quad \mathbf{H}^{\mathrm{fbs}} = \begin{bmatrix} \times & \times \\ \times & \times \end{bmatrix}$$

$$\mathbf{F}^{\mathrm{cf}}(\mathbf{H}^{\mathrm{fbs}})^{-1}\mathbf{F}^{\mathrm{fbs}} = \begin{bmatrix} \times & 0 & \times & 0 & 0 & 0 \\ 0 & 0 & 0 & 0 & 0 & 0 \\ \times & 0 & \times & 0 & 0 & 0 \\ 0 & 0 & 0 & 0 & 0 & 0 \\ 0 & 0 & 0 & 0 & 0 & 0 \\ 0 & 0 & 0 & 0 & 0 & 0 \end{bmatrix}$$

When we compare the computational time required for the operator-split solution procedure (3.43) and for the monolithic approach (3.30), we obtain the graph shown in Figure 3.4. This graph is obtained by solving an example from section 3.4.1 using both approaches, and then plotting the total computational time against the number of time steps in the analysis. In this case, the operator-split solution procedure turns out to be more than six times faster than the monolithic approach. Also, while solving many examples with both approaches, it has been observed that the partitioned computation is more robust compared to the monolithic one. That is to say, when solving the equations simultaneously, in several cases the computation did not converge until the end, so the execution was not completed. It is due to the fact that the nonlinear behavior exhibited by concrete and by bond-slip is solved simultaneously, which can lead to numerical problems. In contrast, the partitioned

computation divides the nonlinearities in two phases, and thus handles them more efficiently. Yet, for the partitioned approach to give accurate results, the chosen time step has to be small enough to allow for a proper redistribution of stresses between the global and the local phase in each increment.

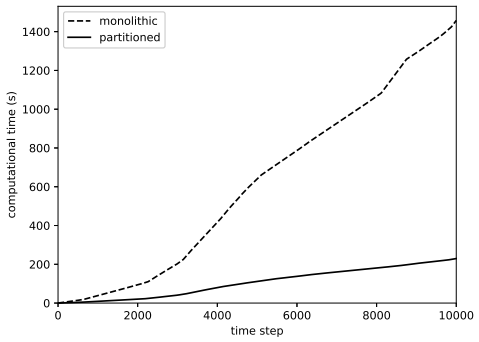

Figure 3.4: Comparison of total computational time for a monolithic and partitioned approach, obtained from an example in section 3.4.1.

The multi-scale approach for a typical time step is illustrated on Figure 3.5, where it can be seen how the macro-scale computations are divided into a macro-global and macro-local phase, and how the micro-scale computations are connected to them. Concrete and the fiber contribute to global iterations i (shown in a green rectangle), while the fiber and the bond-slip contribute to local iterations j (shown in a red rectangle). The fiber is the only component to contribute to both phases (brown intersection between the two rectangles).

Also, as has been explained in detail in Chapter 2, each micro-scale computation can have its own subdivision in a micro-local and micro-global phase. It is the case for concrete, where the internal variables for hardening and softening, including the crack opening $\boldsymbol{\alpha}^{\mathrm{c}}$, are computed at the element level, and the concrete displacements are computed at the global level. The same is true for the elasto-plastic bond-slip computation, where the internal variables and plastic slip $\alpha^{\mathrm{bs,p}}$ are computed at the micro-local level.

3.2.1 A few details regarding bond-slip treatment

In addition to the explanations given in section 2.3 regarding the treatment of bond-slip, a few additional remarks have to be made. First of all, the boundary conditions along the fiber are not always the same. In the case of standard reinforced concrete, the slip is equal to zero at the ends of the reinforcement bar, since it is anchored in the surrounding concrete. In the case of fibers, their ends can be pulled out, and the

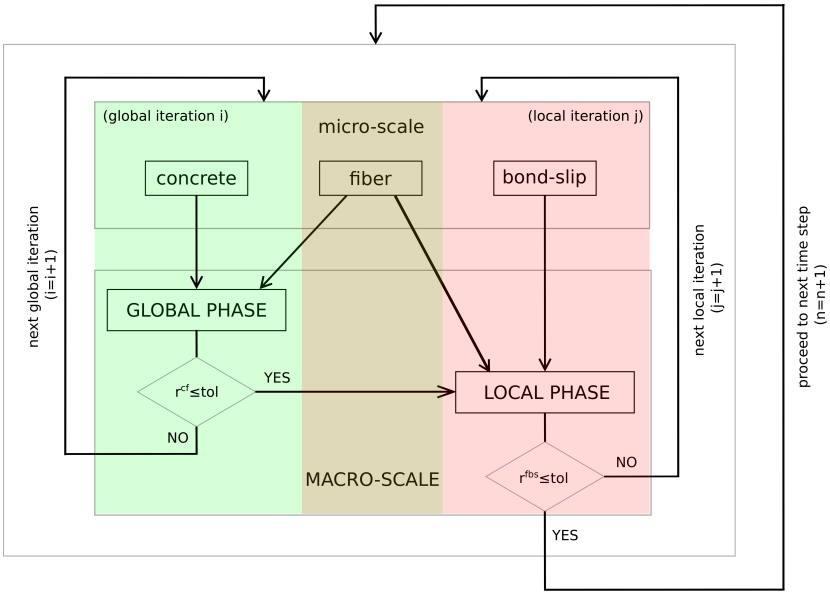

Figure 3.5: Algorithm flow-chart for the multi-scale framework.

fixed point is chosen to be where the crack in concrete appears. This behavior has been observed during experimental tests which are shown in section 2.3.1.

Another difference is in the activation of bond-slip. In numerical examples for standard reinforced concrete, the bond-slip is active from the beginning of the analysis. First, it exhibits a linear elastic behavior, and when it reaches the limit value τ_y, the plastic slip activates. This procedure is performed on the local level of each element, and the admissibility of the bond stress is checked with the function ϕ^{bs}.

When we deal with fiber reinforcement, we are assuming a perfect bond between the fiber and the concrete until the first crack in concrete in an enriched element appears. At that moment, the crack opening that happens at the local level of the element, activates the bond-slip globally, in all the elements containing the fiber. This is due to the "cooperation" of the ED-FEM and the X-FEM approach: the ED-FEM takes care of the crack $\boldsymbol{\alpha}^{\text{c}}$ in the concrete element, while the X-FEM deals with the global distribution of slip α^{bs} along the fiber. In practice, this means that we have to run the computation two times: in the first run, we get the crack location and the time step in which the first enriched element fails. Then, in the second run, we set the bond-slip flag to be active from that particular time step onwards, with the boundary conditions for bond-slip fixed in the cracked element.

To avoid rigid-body modes in the bond-slip computation, we have to introduce a global fixed point for the enriched degrees of freedom, where the value of slip will be set to zero. Regarding its exact placement on the fiber, it would be ideal to put it in the middle of the element, where the crack in concrete appears. But, since the

boundary condition has to be applied in nodes, we have a choice of fixing either the left or the right node, or both of them. The latter has proven not to be a good choice, because by fixing both nodes at the same time, the global behavior of the composite changes, and there are some spurious stresses in the central element. The comparison of different fixed points will be shown in numerical examples in section 3.4.1.

3.2.2 Pseudo-code for a typical time step

A brief description of the solution scheme for time step $n+1$ and iteration (i) is given below.

Central Problem Computation in a typical time step $[t_n, t_{n+1}]$:

- Given: $\mathbf{d}^c_n$, $\boldsymbol{\alpha}^{bs}_n$, internal variables at t_n
- Find: $\mathbf{d}^c_{n+1}$, $\boldsymbol{\alpha}^{bs}_{n+1}$, internal variables at t_{n+1}
  where: $\mathbf{d}^{c,(i)}_{n+1} = \mathbf{d}^c_n$, $\boldsymbol{\alpha}^{bs,(i)}_{n+1} = \boldsymbol{\alpha}^{bs}_n$

1. Micro-scale computations
   - Concrete computation
     - ▹ In the bulk
       compute values of internal variables $\bar{\gamma}, \bar{\xi}, \bar{q}, \bar{\mathbf{D}}, \bar{\phi}$
       IF: $\bar{\boldsymbol{\sigma}}^{\mathrm{c}} < \sigma_u \implies$ proceed to fiber computation
       ELSE IF: $\bar{\boldsymbol{\sigma}}^{\mathrm{c}} \geq \sigma_u \implies$ *crack* = true (softening starts), proceed to computation at the discontinuity
     - ▹ At the discontinuity
       compute values of internal variables $\bar{\bar{\gamma}}, \bar{\bar{\xi}}, \bar{\bar{q}}, \bar{\bar{\mathbf{Q}}}, \bar{\bar{\phi}}, \boldsymbol{\alpha}^{\mathrm{c}}$

     compute concrete strain and stress $\boldsymbol{\varepsilon}^{\mathrm{c}}, \boldsymbol{\sigma}^{\mathrm{c}}$
   - Fiber computation
     compute fiber strain and stress $\varepsilon^{\mathrm{f}}, \sigma^{\mathrm{f}}$
   - Bond-slip computation (computed only if *crack* = true)
     compute bond-slip strain and stress $\varepsilon^{\mathrm{bs}}, \sigma^{\mathrm{bs}}$
2. Macro-scale computations
   - Compute tangent stiffness matrices and residuals
     $\mathbf{K}^{\mathrm{cf}}, \mathbf{F}^{\mathrm{cf}}, \mathbf{F}^{\mathrm{fbs}}, \mathbf{H}^{\mathrm{fbs}}, \mathbf{r}^{\mathrm{cf}}, \mathbf{r}^{\mathrm{fbs}}$
   - Global phase

- ▹ Solve global equation

$$\tilde{\mathbf{K}}\,\Delta\mathbf{d}^{\mathrm{c}}_{n+1} = -\mathbf{r}^{\mathrm{cf}}_{n+1}$$

- ▹ Update concrete displacement

$$\mathbf{d}^{\mathrm{c}}_{n+1} = \mathbf{d}^{\mathrm{c}}_{n} + \Delta\mathbf{d}^{\mathrm{c}}_{n+1}$$

- ▹ Check global convergence
  IF: $||\mathbf{r}^{\mathrm{cf}}_{n+1}|| >$ tolerance $\implies$ perform another global iteration
  ELSE IF: $||\mathbf{r}^{\mathrm{cf}}_{n+1}|| \leq$ tolerance $\implies$ proceed to local phase

- Local phase
  - ▹ Solve local equation

$$\mathbf{H}^{\mathrm{fbs}}\Delta\boldsymbol{\alpha}^{\mathrm{bs}}_{n+1} = -\mathbf{r}^{\mathrm{fbs}}_{n+1}$$

  - ▹ Update bond-slip displacement

$$\boldsymbol{\alpha}^{\mathrm{bs}}_{n+1} = \boldsymbol{\alpha}^{\mathrm{bs}}_{n} + \Delta\boldsymbol{\alpha}^{\mathrm{bs}}_{n+1}$$

  - ▹ Check local convergence
    IF: $||\mathbf{r}^{\mathrm{fbs}}_{n+1}|| >$ tolerance $\implies$ perform another local iteration
    ELSE IF: $||\mathbf{r}^{\mathrm{fbs}}_{n+1}|| \leq$ tolerance $\implies$ proceed to next time step

3.3 Application to standard reinforcement

To test the performance of the developed formulation, we have performed a tension test on a concrete specimen of dimensions 400x100x100 mm^2, reinforced by a steel bar of diameter $\phi = 16$ mm. This example is presented in [64]. Since our model is 2D (as shown of Figure 3.6), the area of the bar and the bond-slip area are divided by the thickness of the specimen.

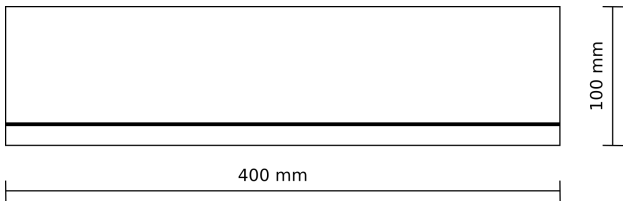

Figure 3.6: Geometry of the reinforced concrete specimen in 2D.

We consider the steel bar to be fixed at both ends, as it is anchored in concrete. The material properties used in the model are listed here:

- for concrete: $E^{\mathrm{c}} = 45700\,\mathrm{MPa}$, $\nu^{\mathrm{c}} = 0.2$, $\bar{\sigma}_f = 3.5\,\mathrm{MPa}$, $\bar{K}^{\mathrm{c}} = 1000\,\mathrm{MPa}$, $\bar{\bar{\sigma}}_f = 4\,\mathrm{MPa}$, $\bar{\bar{\sigma}}_{f,weak} = 3.8\,\mathrm{MPa}$, $\bar{\bar{\beta}}^{\mathrm{c}} = 20\,\mathrm{MPa/mm}$;
- for the steel bar: $E^{\mathrm{f}} = 210000\,\mathrm{MPa}$, $A^{\mathrm{f}} = 2.01\,\mathrm{mm}^2$;
- for the bond: $K^{\mathrm{bs}} = 30\,\mathrm{N/mm}^3$, $\tau_y = 6\,\mathrm{MPa}$, $K^{\mathrm{bs,h}} = 0.03\,\mathrm{N/mm}^3$, $A^{\mathrm{bs}} = 0.5\,\mathrm{mm}$.

Here, $\bar{\bar{\sigma}}_{f,weak}$ is the ultimate stress for a strip of weakened elements in the middle of the specimen where the crack appears.

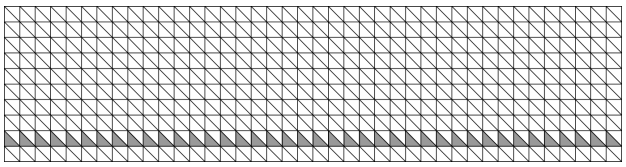

Figure 3.7: Finite element mesh with enriched elements shown in grey.

The specimen is fixed at the left-hand side, and there is an imposed displacement $\bar{u} = 0.5\,\mathrm{mm}$ acting on the right-hand side. The finite element mesh shown on Figure 3.7 consists of 800 CST elements, where the triangle sides of each element have the dimension 10 mm. There are 40 enriched elements along the reinforcement bar.

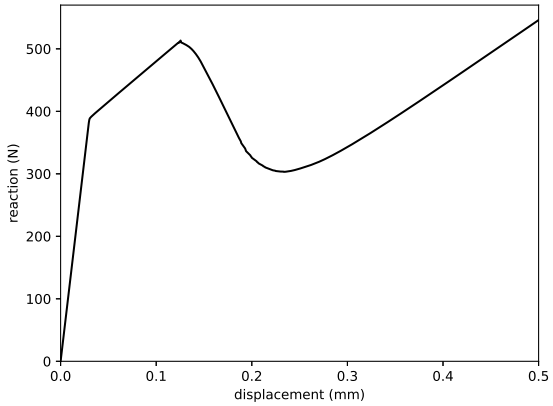

Figure 3.8: Force-displacement diagram for the tension test on a reinforced concrete specimen.

The force-displacement diagram shown on Figure 3.8. plots the reaction in the x-direction at the left-hand side against the imposed displacement on the right-hand side. We can observe several particular phases of the composite behavior: the linear elastic phase is followed by a hardening phase when micro-cracks start do appear in

concrete. After the ultimate load of about 500 N is reached, the crack develops in the weak zone in the middle of the specimen, so we enter the softening phase. After a while, the reaction starts ascending, due to the redistribution of stresses and the reinforcement activation. This resembles the typical diagrams that are found in the literature, which are obtained for a specimen with a single crack.

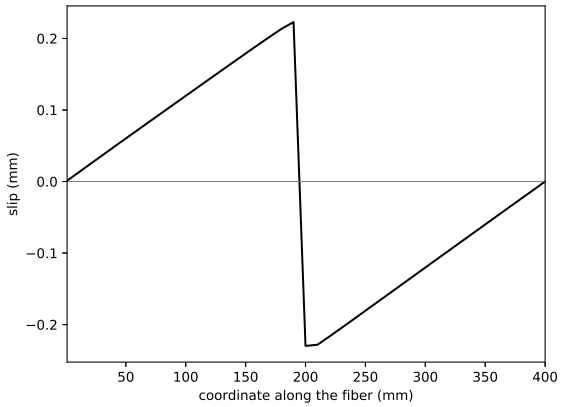

Figure 3.9: Distribution of slip α^{bs} along the reinforcement bar at the end of the analysis (nodal values).

On Figure 3.9 we can see the distribution of slip along the reinforcement bar, where the largest slips are taking place near the crack, and at the ends the slip is zero. On the left of the crack, α^{bs} has a positive value, and on the right side it is negative, because the reinforcement is moving (relatively to the concrete) from the ends to the centre (in other words, towards the crack).

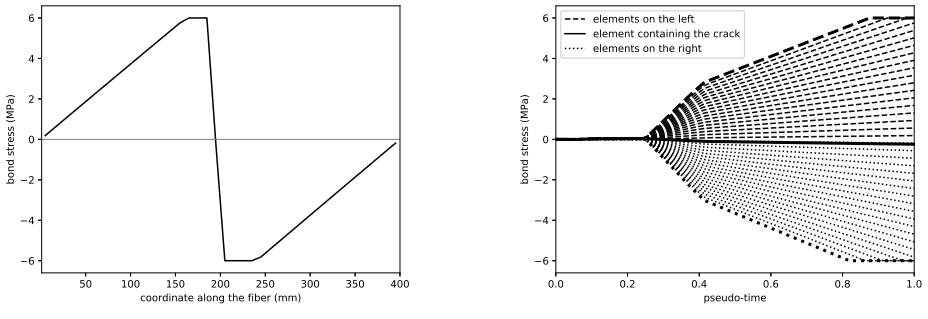

(a) (b)

Figure 3.10: Bond stress: (a) distribution of σ^{bs} along the reinforcement bar (values at Gauss points); (b) evolution of σ^{bs} in time for all enriched elements.

The bond stress has a very similar distribution (Figure 3.10a), according to the chosen bond-slip law on the interface. The evolution of bond stress in time gives rise

to an interesting plot (Figure 3.10b), where the dashed lines represent the elements left of the crack, and the dotted lines represent the ones on the right. We can see that the elements on the left have a positive value of bond-stress, and for the elements on the right the bond stress is negative. The bold solid line represents the value of bond stress in the cracked element, that is very near to zero, since it is the inflection point of the curve shown on Figure 3.10a. The bold dashed and bold dotted line represent the elements nearest to the crack, where the bond stress is largest, and where the ultimate value of bond stress, σ^{bs}, has been reached.

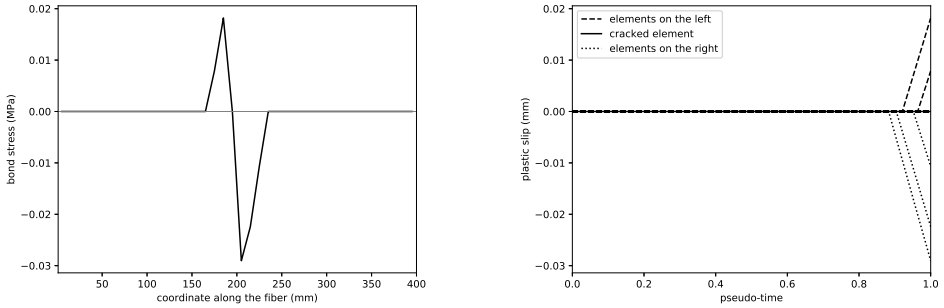

(a) (b)

Figure 3.11: Plastic slip: (a) distribution of $\alpha^{\mathrm{bs,p}}$ along the reinforcement bar at the end of the analysis (values at Gauss points); (b) evolution of $\alpha^{\mathrm{bs,p}}$ in time for the enriched elements that have entered the plastic phase.

Related to that is the plastic slip development shown on Figure 3.11b, where it can be observed that the plasticity occurs only at the end of the analysis, in five elements that are nearest to the crack (two on the left side, and three on the right). The same can be seen on Figure 3.11a, where the plastic slip is plotted in Gauss points along the reinforcement bar. The plastic slip is equal to zero in most of the enriched elements, since they have not yet entered the plastic phase and the interface is behaving elastically.

Figure 3.12 gives the representation of the crack opening in concrete, that reaches the value of 0.47 mm at the end of the analysis. As it has been already explained, the macro-crack starts to open when the material reaches the ultimate stress, which happens around time 0.25. There are also two small crack in the elements right next to the main crack, but their size is negligible compared to the main crack.

It is interesting to point out that the crack opening in concrete coincides with the slip activation, which can be compared on Figure 3.10b and Figure 3.12b. This is in accordance with our model assumption that there is no slip when the concrete and the steel have the same displacement. So, the crack opening in concrete, $\boldsymbol{\alpha}^{\mathrm{c}}$, is

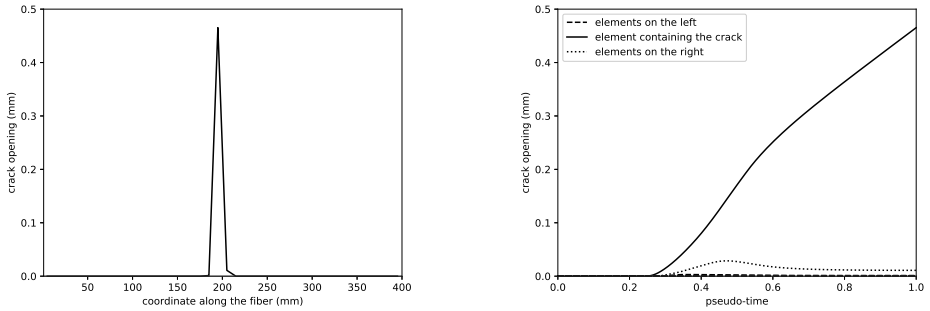

(a) (b)

Figure 3.12: Crack opening in concrete: (a) distribution of α^{c} along the reinforcement bar at the end of the analysis (values at Gauss points); (b) evolution of α^{c} in time for the cracked element in the middle of the specimen.

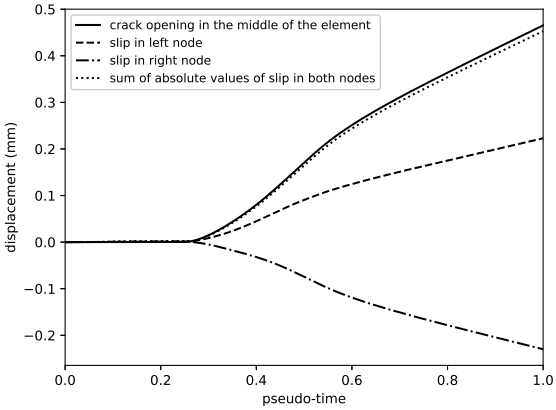

Figure 3.13: Comparison of the evolution in time of α^{c} and α^{bs}: the crack opening in concrete in the middle of the element is nearly equal to the sum of the absolute values of slip in the left and right node of the same element.

giving rise to the difference between the concrete and steel strain field, that is, in turn, activating the bond-slip α^{bs}. Moreover, we can test this notion by plotting the crack opening evolution and the slip evolution on the same diagram, as has been done on Figure 3.13. We are plotting the values of $\boldsymbol{\alpha}^{\mathrm{c}}$ in the Gauss point of the cracked element (represented by the solid line), and the values of α^{bs} in left and right node of the same element (dashed and dotted line, respectively). While we have already noted that the two nodes in question have the displacements of opposite sign, it is even more compelling that, quantitatively, the absolute values of the two slips add up to give nearly the same value as the crack opening at a given time. The sum of two slips is represented by a dotted line on Figure 3.13.

3.4 Application to fiber reinforcement

In order to illustrate the performance of the proposed model with pull-out, we have run numerical simulations for several different examples, including a specimen subjected to tension, or to three-point bending. The latter also serves as a validation test since it can be compared with the experimental results.

3.4.1 Tension test

We start by modelling a sample loaded in tension containing a horizontal fiber (see Figure 3.14). The sample, of dimensions 4x4 mm^2, is fixed at the left end, and subjected to imposed displacement $\bar{u} = 0.05$ mm at the right end. The example is taken from [23]. We will first run a simulation with the matrix material taken to be linear elastic, and then perform different analyses with a nonlinear behavior of the matrix, where the bond-slip is taken into account.

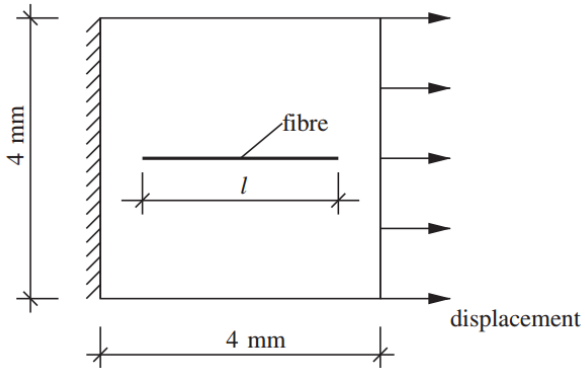

Figure 3.14: Sample with horizontal fiber [23].

Linear elastic case

We analyze four different cases: with no fiber, with a short ($l^f = 1$ mm), medium ($l^f = 2$ mm) and long ($l^f = 3$ mm) fiber. The Young's modulus of the matrix material is $E^c = 20000$ MPa, and the Poisson's ratio $\nu^c = 0.2$. The fiber has a diameter $\phi^f = 0.05$ mm, and Young's modulus $E^f = 500000$ MPa. Unlike [23], we assume a perfect bond on the fiber-matrix interface, so we do not consider bond stiffness for a linear elastic case.

We choose a mesh of 512 triangular elements, shown in Figure 3.15a. The elements shown in black contain the fiber, and are thus enriched accordingly. Here, we show the example with the medium fiber of length $l^f = 2$ mm. In Figure 3.15b, the contour plot of the displacements in x-direction at the end of the analysis is shown, where the influence of the fiber can be clearly seen.

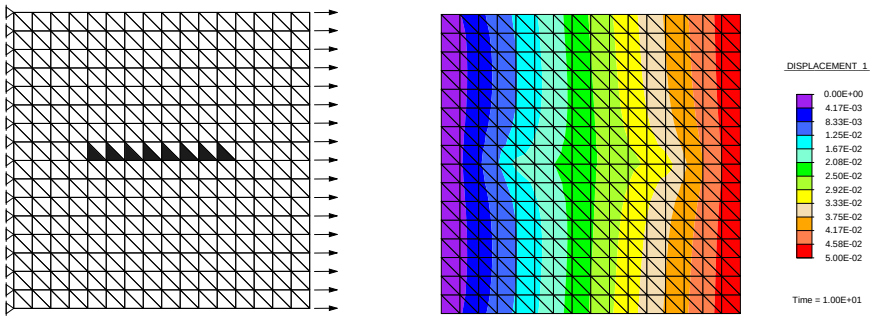

(a) (b)

Figure 3.15: Linear elastic analysis for the domain with a medium fiber ($l^{\mathrm{f}} = 2$ mm): (a) Finite element mesh with enriched elements shown in black ; (b) Contour plot of displacements in x-direction at the end of the analysis.

In Figure 3.16, the force-displacement diagram plots the imposed displacement on the right end vs. the reaction in x-direction on the left end of the specimen, for the case with no fiber, with a short, medium and long fiber. We can notice that the increase in the fiber length leads to an increase in stiffness, providing a stiffer response of the whole sample, with higher stress at the same strain. In Figure 3.17, it can be seen that our result for the sample with medium fiber is in a good agreement with the one obtained in [23], despite our assumption of a perfect bond between the fiber and concrete.

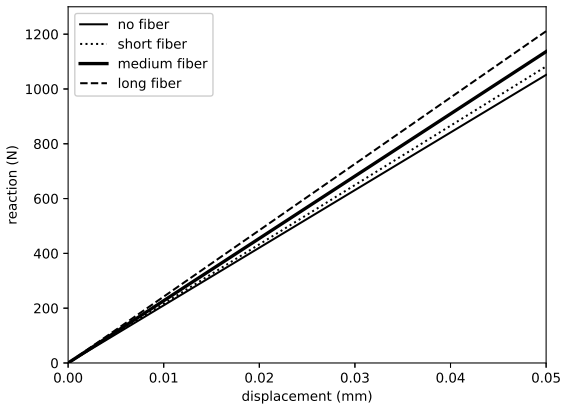

Figure 3.16: Force-displacement diagram for the linear elastic behavior of the matrix material, for different fiber lengths.

Damage case

We can now consider the nonlinear behavior of the matrix material, where the chosen material parameters are the following: Young's modulus $E^{\mathrm{c}} = 2000$ MPa, Poisson's

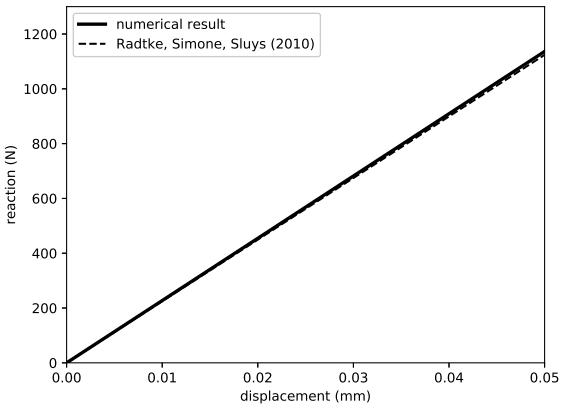

Figure 3.17: Comparison with [23] for a medium fiber ($l^{\mathrm{f}} = 2$ mm).

ratio $\nu^{\mathrm{c}} = 0.2$, the stress at the first cracking $\bar{\sigma}_f = 4.5$ MPa, the hardening modulus $\bar{K} = 1000$ MPa, the ultimate stress $\bar{\bar{\sigma}}_f = 10$ MPa. The ratio of the softening parameter and the ultimate stress is $\bar{\bar{\beta}}^{\mathrm{c}}/\bar{\bar{\sigma}}_f = 20$. The shear/tension ratio (the ratio between the ultimate stress in the tangential and the normal direction) is chosen to be $\bar{\bar{\sigma}}_s/\bar{\bar{\sigma}}_f = 0.3$. There is a weak stripe near the middle of the specimen (shown in grey in Figure 3.18a), whose ultimate stress is chosen to be half the value of the one in the other elements $\bar{\bar{\sigma}}_{f,\mathrm{weak}} = 5$ MPa. This will lead to the formation of the crack in one of the enriched elements containing the fiber, that will allow us to observe the bond-slip behavior that we want to examine.

The Young's modulus for the fiber is $E^{\mathrm{f}} = 500000$ MPa, and its diameter $\phi^{\mathrm{f}} = 0.05$ mm, like in the previous example. The material parameters for bond-slip are $\tau_y = 6$ MPa, and $\beta^{\mathrm{bs}} = 20$.

In Figure 3.19, we can see the force-displacement curves for different fiber lengths, where the reaction on the left edge of the specimen is plotted against the displacement imposed at the right edge. It is clearly visible that the addition of the fiber increases the ductility of the specimen, and the length of the fiber influences the post-peak response. The macro-crack has developed in the weak zone, and micro-craks have appeared around the fiber edges (Figure 3.18b). The direction of the "bump" in the middle of the contour plot marks the side on which pull-out is taking place. The bond-slip activation happens when the enriched element located in the weak zone cracks, which causes a jump in the force-displacement diagrams shown on Figure 3.18.

The slip along the fiber for three different fiber lengths is shown on Figure 3.20. In all three cases, the fixed point is in the node left of the crack, and it can be seen that it has zero slip. The short (dotted line) and the medium fiber (thick solid line)

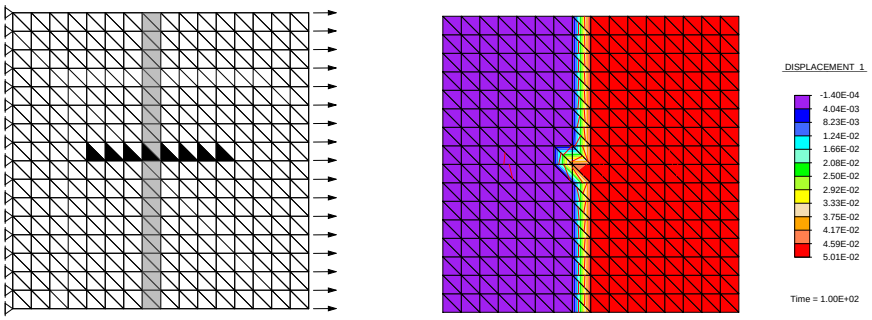

(a) (b)

Figure 3.18: Damage analysis for the domain with a medium fiber ($l^{\mathrm{f}} = 2$ mm): (a) finite element mesh with enriched elements shown in black and weakened elements shown in grey; (b) contour plot of displacements in x-direction at the end of the analysis, where the cracks are shown with red lines.

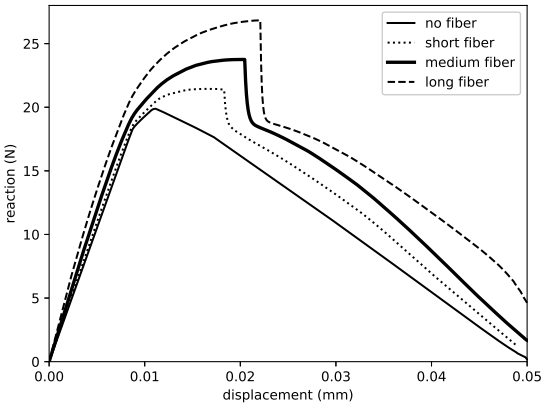

Figure 3.19: Force-displacement curves for the damage case for different fiber lengths.

have a pronounced pull-out on the left side, with the right side is almost fixed, while the long fiber (dashed line) has a more balanced distribution of slip on both sides. In all cases, the slips on the left side of the crack are positive, while the slips on the right side are negative, as has been already explained in the reinforced concrete example (see Figure 3.9).

When we consider a case without bond-slip, we get the result without a jump, as shown on Figure 3.21. Of course, this is not a realistic representation, because it would suppose a perfect bond between the fiber and the matrix even after the cracking, which has been shown experimentally not to be the case. On Figure 3.22, we can see the stress distribution in concrete in x-direction for the case with and without bond-slip. When we do not consider bond-slip (Figure 3.22b), the fiber is constrained to move with concrete throughout the whole analysis, and the largest

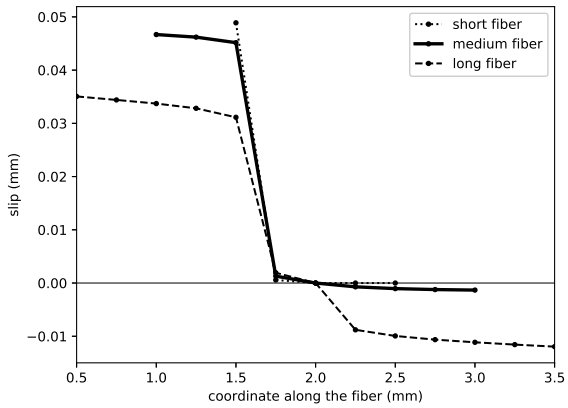

Figure 3.20: Slip distribution along the fiber for different fiber lengths.

stresses appear around the fiber ends. In the case with bond-slip (Figure 3.22a), the redistribution of stresses takes place, and the stress is concentrating around the point where the slip is fixed.

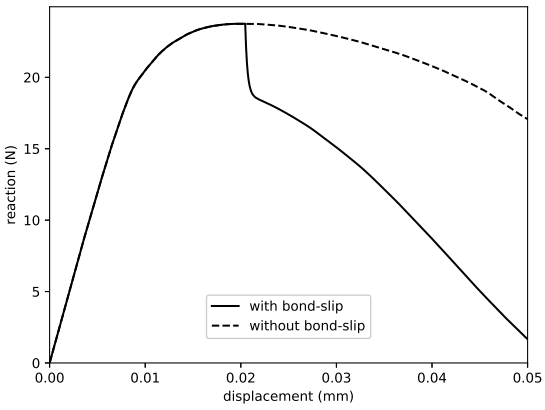

Figure 3.21: Force-displacement curve with and without bond-slip for the medium fiber.

In section 3.2.1, we have already mentioned the importance of choosing an appropriate fixed point for the enriched degrees of freedom, where the slip takes zero value. The solid line and the dotted line on Figure 3.23 represent the case when either the right, or the left node is fixed, and it can be seen that there is no big difference between them. In contrast, when both nodes are fixed, the result changes, which can be especially visible on the local level of the fiber (Figure 3.23b).

The exponential pull-out bond-slip law depends on the parameter β^{bs}: the larger it is, the steeper the descent of the curve, meaning that less energy is needed to pull-out the fiber completely. Figure 3.24 shows the bond stress vs. slip diagram for four

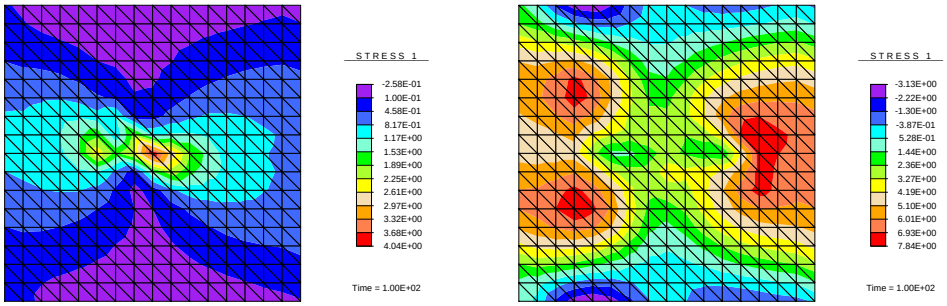

(a) (b)

Figure 3.22: Stress distribution in concrete in x-direction: (a) with bond-slip; (b) without bond-slip.

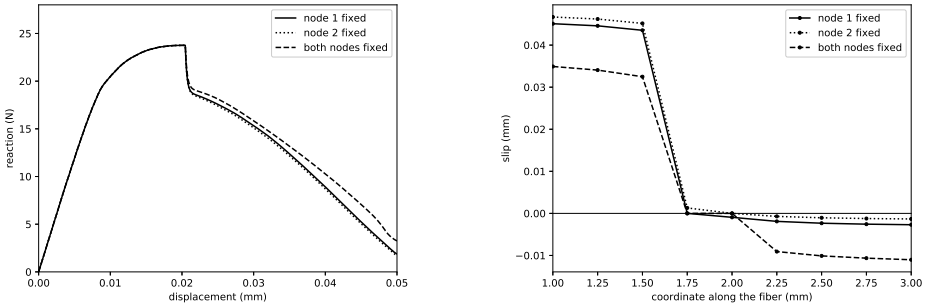

(a) (b)

Figure 3.23: Influence of the choice of the fixed node: (a) on the global level (force-displacement diagram); (b) on the local level of the fiber (slip distribution).

different values of the bond-slip parameter. When $\beta^{\text{bs}} = 2$, the stress-slip relation is almost linear, whether for $\beta^{\text{bs}} = 2000$, the stress drops immediately, starting for very small values of slip. When the stress σ^{bs} gets close to zero, that means that the interface has no residual strength whatsoever, and the fiber is pulled out of concrete.

The distribution of bond stresses along the fiber is shown on Figure 3.25 for the same four cases. For the smallest value of β^{bs}, the bond stress is still close to the starting value of 6 MPa on both sides. When we increase β^{bs} to 20, the slip activates on the left side, but the values of stress remain larger than zero in all the elements, so complete pull-out has not happened yet. For $\beta^{\text{bs}} = 200$, the fiber has been completely pulled out from the three elements on the left side, as the bond stress in them has approached zero. For the largest value of β^{bs}, complete pull-out is happening on both sides of the crack.

It is interesting to show the relationship between the bond stress σ^{bs}, and the stress in the fiber σ^{f}, that is given on Figure 3.26. Here, the sign of the stress just denotes the direction in which it is acting: since both ends of the fiber are moving

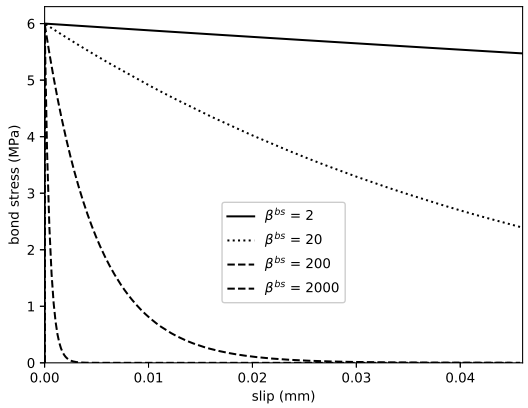

Figure 3.24: Bond stress vs. bond strain for different values of the parameter β^{bs}.

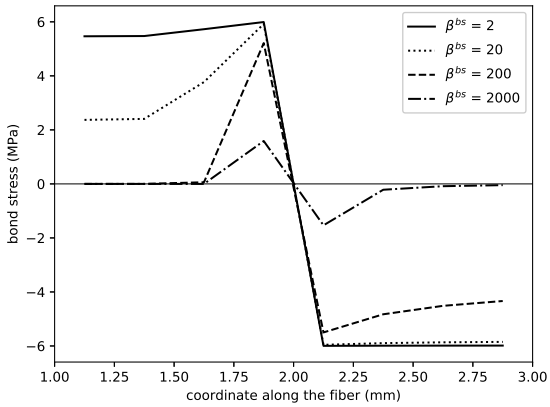

Figure 3.25: Bond stress along the fiber for different values of the tangent modulus β^{bs}.

towards the crack (relatively to concrete), the bond stress has a positive value on the left side, and a negative value on the right side. The opposite is true for the fiber stress. Before the bond-slip activation, the fiber has the same displacements as concrete, and the fiber stress slowly increases in time. When the crack in concrete appears, and the bond-slip activates, the stress in the fiber suddenly drops to the same value of the bond-slip stress, but of the opposite sign. This is in accordance with the local equilibrium equation (3.29), which gives the relationship between the internal force vectors for the fiber and for bond-slip. In this example we have taken that the area of the fiber is equal to the fiber diameter [25], as is the bond-slip area $A^{\text{bs}} = A^{\text{f}} = \phi^{\text{bs}}$. Since the shape functions are the same, it follows that $\sigma^{\text{f}} = -\sigma^{\text{bs}}$. In our example, the enriched element on the far left (element 1) is the first one from which the fiber is being completely pulled out, as it is the first one to reach $\sigma^{\text{bs}} \approx \sigma^{\text{f}} \approx 0$. It can be seen on Figure 3.27, where the evolution of bond stress in time is plotted for the

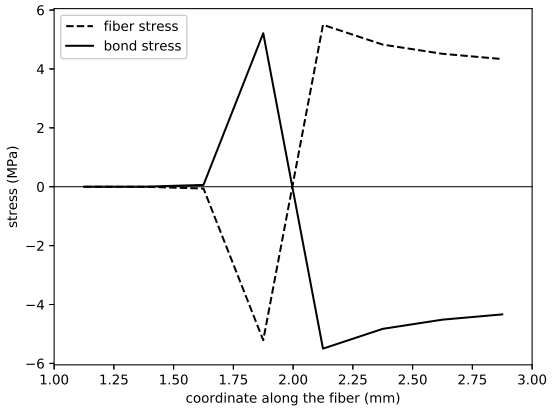

Figure 3.26: Bond stress and fiber stress along the fiber at the end of the analysis for the example with medium fiber and $\beta^{\text{bs}} = 200$.

three elements left of the crack. We did not show the evolution of bond stress in the elements right of the crack, since they do not get close to complete pull-out, as it can be seen on Figure 3.26.

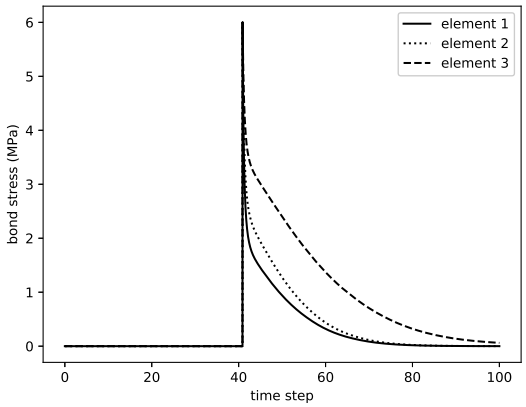

Figure 3.27: Evolution of bond stress in time for three elements on the left.

Now let's consider a case when the crack does not appear in the middle of the specimen, but has a different location. We are controlling this by varying the position of the weak zone (Figure 3.28).

On Figure 3.29 we can see the influence of the crack location on the global response of the specimen, and on Figure 3.30 its influence on the local distribution of slip along the fiber. It can be observed that the crack in the middle-left part of the specimen (in element 3) results with the largest slip on the left side, and the crack in the middle-right (in element 6) results with the largest slip on the right side,

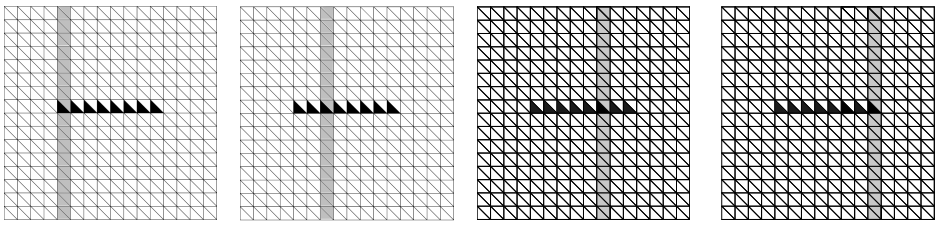

Figure 3.28: Position of the weak zone in the specimen (a) completely on the left - element 1; (b) in the middle-left - element 3; (c) in the middle-right - element 6; (d) completely on the right - element 8.

since it is always the shorter part of the fiber that gets pulled out. This is explained by the fact that the longer part of the fiber needs more energy to break the bond and get pulled-out, as has been shown experimentally in our single-fiber pull-out tests presented in section 2.3.1. When the crack appears completely on the right (in element 8), the bond-slip does not get activated at all and is equal to zero along the whole fiber. A similar scenario happens when the crack is completely on the left (in element 1), when the slip gets barely activated, which is in accordance with the experimentally observed phenomena.

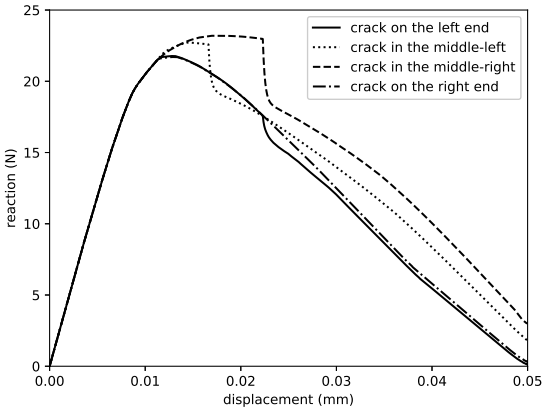

Figure 3.29: Force-displacement diagrams for different crack locations.

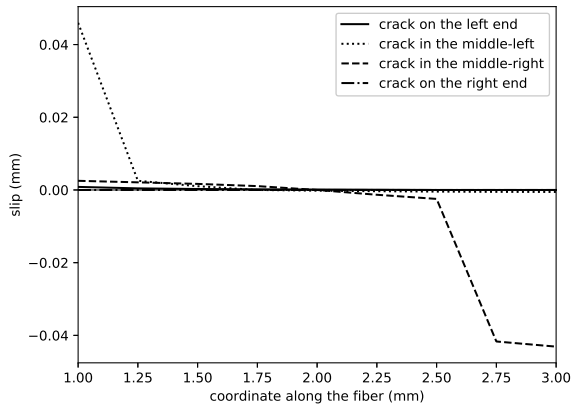

Figure 3.30: Slip along the fiber for different crack locations.

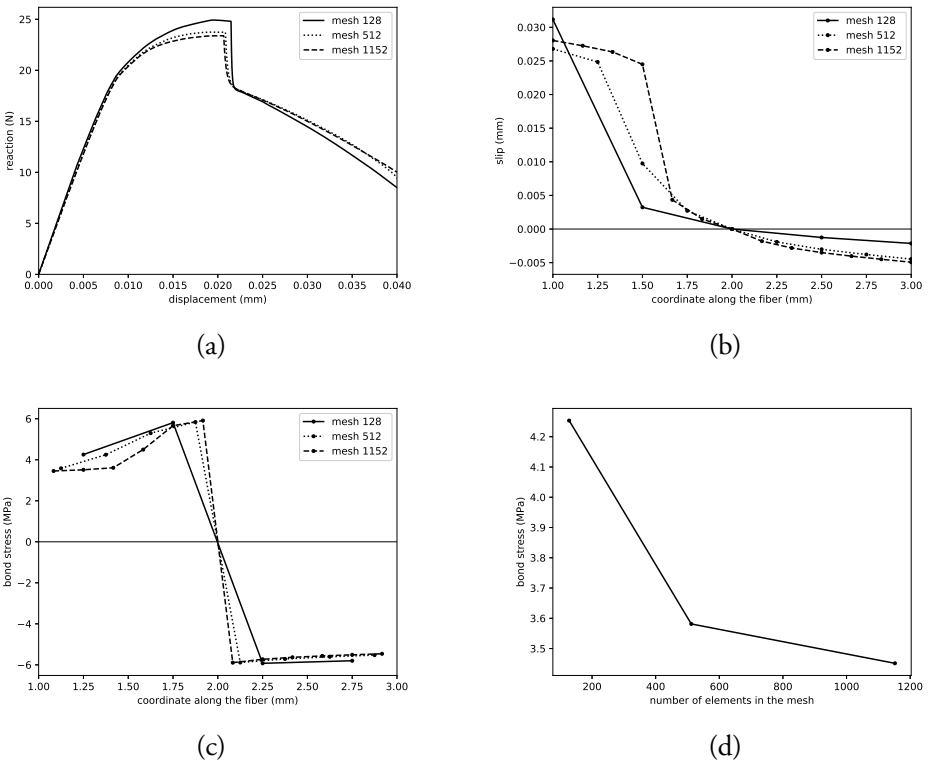

Figure 3.31: Mesh refinement study for three different meshes (128, 512 and 2048 elements): (a) force-displacement diagrams; (b) slip distribution along the fiber; (c) bond stress along the fiber; (d) convergence: bond stress at the left end of the fiber plotted against the number of elements in the mesh.

In the mesh refinement study (Figure 3.31) we compare the force-displacement diagrams for three different meshes: a coarse mesh that consists of 128 elements

(where the fiber is represented by 4 elements), a fine mesh that consists of 512 elements (where the fiber is represented by 8 elements), and an extra fine mesh that consists of 1152 elements (where the fiber is represented by 12 elements). On the force-displacement diagrams (Figure 3.31a), on the slip and stress distribution along the fiber (Figures 3.31b and 3.31c), we can see that all three meshes give similar results. The convergence for the bond stress at the left end of the fiber compared to the number of elements in the mesh is shown on Figure (3.31d). Since we wanted to keep the same width of the weak stripe for all the meshes, for mesh 128 it consisted of one column of elements, for mesh 512 two columns, and for mesh 1152 three. Not all the elements in the weak stripe cracked for every case, and here could lie the slight difference in the results. Also, mesh 128 could be considered too coarse, since the fiber is represented by only four enriched elements, which is not enough for a sufficiently precise description of bond-slip along the fiber.

3.4.2 Three-point bending test on notched specimens

Experimental results

To test the influence of fiber pull-out in a more realistic setting than the one provided by the single-fiber pull-out tests, three-point bending tests on special specimens have been performed. The results and figures for this experimental part are taken from [41].

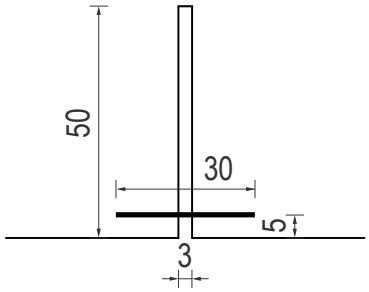

Figure 3.32: The fiber bridging the notch.

The specimens are of dimensions 400x100x100 mm^3, with a 3 mm wide and 50 mm long notch placed in the middle of the specimen. The specimen is simply supported 5 cm from each edge. There are 10 equidistantly placed fibers bridging the notch, and their dimensions are: length $l^f = 30$ mm and diameter $\phi^f = 0.6$ mm. The fibers are placed 5 mm from the lower edge of the specimen, as shown on Figure 3.32. The experimental setup and the specimen are shown on Figure 3.33. The tests have been performed under displacement control, with a speed of 0.002 mm/s.

The load-displacement curve for three specimens can be seen in Figure 3.34. There is a difference in the results due to small imperfections during the pouring

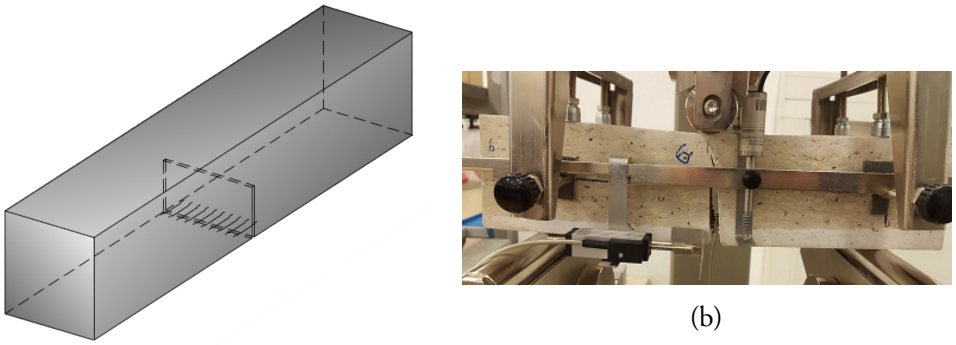

(a) (b)

Figure 3.33: Three-point bending test [41]: (a) specimen; (b) experimental setup.

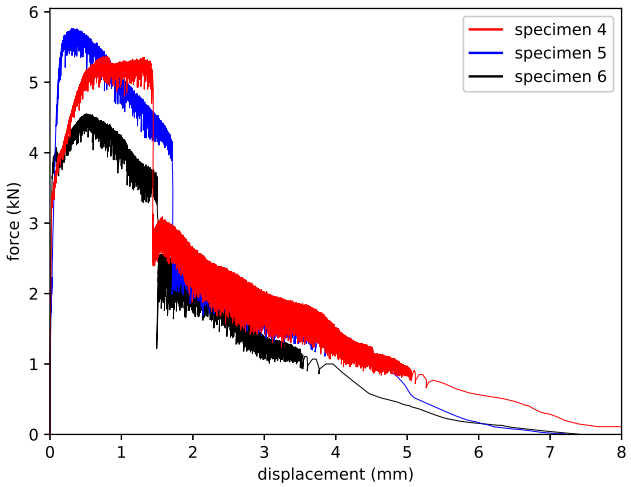

Figure 3.34: Results of the three point bending test [41]: load-displacement curve for three specimens.

of concrete in moulds, and insufficiently precise positioning of the fibers over the notch. Nevertheless, specimens exhibit similar behaviour, and distinct phases of the computed response and failure mechanisms can be observed. First, there is a linear elastic phase, followed by the hardening of the material due to the formation of micro-cracks around the notch. Then, a macro-crack starts to appear in concrete, leading to material softening. There is a jump in force for the value of displacement between 1.5 and 2 mm, due to the bond-slip activation, so the fibers get pulled out while the concrete cracks above the notch.

During the tests, the fibers did not break, but they all got pulled-out of concrete. That means that the fibers have not reached their ultimate strength, because the interface between the steel and concrete was the weakest link that failed first. Figure

Figure 3.35: Steel fibers at the end of the test [41].

3.35 shows the pulled-out fibers at the end of the test.

Numerical simulation

Several insights gained from these experimental tests have been already implemented in our model, such as the slip activation condition, or the fact the main failure mechanism for fibers is their pull-out. In this part we will apply our developed finite elements with enriched degrees of freedom to simulate the three-point bending tests shown in the previous part.

Since the experimental results shows a scattering of results, and as for constructing the model we are making more than a few approximations (3D vs. 2D, number of fibers in the specimen, chosen material properties, etc.), our goal is not to obtain an exact match between the numerical and the experimental results, but rather provide a qualitative comparison of the failure mechanisms exhibited by the specimen.

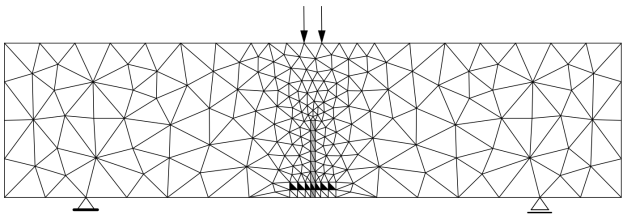

Figure 3.36: Mesh and boundary conditions for the modeled specimen, where the notch is represented with grey elements, and the enriched elements containing fiber are shown in black.

In this numerical model we consider the specimen in Figure 3.36 to be a 2D plane-strain representation of the real 3D specimen. To be able to implement in the mesh the fiber that is crossing the notch (in accordance with our conforming description of the fiber position along the element's edge), two rows of elements at the bottom of the notch are straight. The mesh in the other parts of the domain is unstructured, and is finer around the notch, to give a better representation of crack development.

Also, we are modeling the notch with a stripe of very weak elements, whose ultimate strength is 1/100 of the value for the other elements. We have chosen to do it this way to allow for the continuity of the enriched elements representing the fiber.

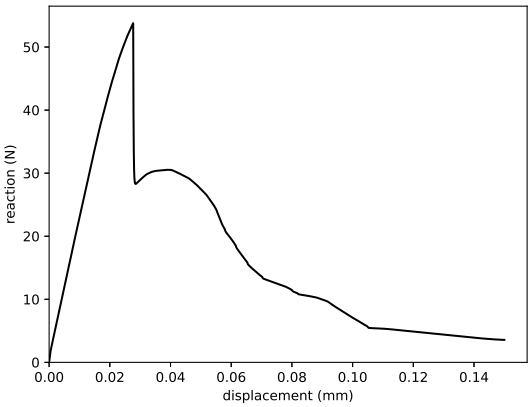

Figure 3.37: Results of the numerical simulation for the three-point bending test.

The chosen material parameters for our model are: for concrete: $E^{\mathrm{c}} = 36000$ MPa, $\nu^{\mathrm{c}} = 0.2$, $\bar{\sigma}_f = 3.5\,\mathrm{MPa}$, $\bar{K} = 1000\,\mathrm{MPa}$, $\bar{\bar{\sigma}}_f = 4\,\mathrm{MPa}$, $\bar{\sigma}_{f,weak} = 0.035\,\mathrm{MPa}$, $\bar{\bar{\sigma}}_{f,weak} = 0.04\,\mathrm{MPa}$, $\bar{\bar{\beta}}/\bar{\bar{\sigma}}_f = 50$; for the fiber: $E^{\mathrm{f}} = 210000\,\mathrm{MPa}$, $A^{\mathrm{f}} = 0.0283\,\mathrm{mm}^2$; for the bond: $\beta^{\mathrm{bs}} = 30$, $\tau_y = 6\,\mathrm{MPa}$, $A^{\mathrm{bs}} = 0.1885\,\mathrm{mm}$. For computing the area of the fiber A^{f}, we take the area of ten fibers divided by the specimen thickness. A similar calculation is performed for the bond-slip area A^{bs}.

To clarify one point regarding the bond-slip activation: since here the notch (or "opening") is present from the beginning, we will not consider the cracking of the central enriched element that crosses the notch to be a valid trigger for the slip activation. Rather, the slip will be activated when the first among the other elements containing the fiber cracks.

On Figure 3.37, the force-displacement diagram for the three-point bending test is shown. The characteristic jump that has been observed in the experimental results is also present here. The reaction force is increasing until it reaches 53.8 N, and then suddenly drops to the value of 28.5 N. The following part of the diagram exhibits a minor increase in force, and then slowly decreases to almost reach zero. This part of the composite response comprises the fiber pull-out, along with the development of the crack above the notch.

Our diagram resembles the graph obtained for specimen 4 in Figure 3.34, and even the values are comparable, since on the real specimen the force drops from around 5 kN to around 3 kN. On our specimen the values are similar, but just divided by 100, a value that stands for the thickness of the specimen.

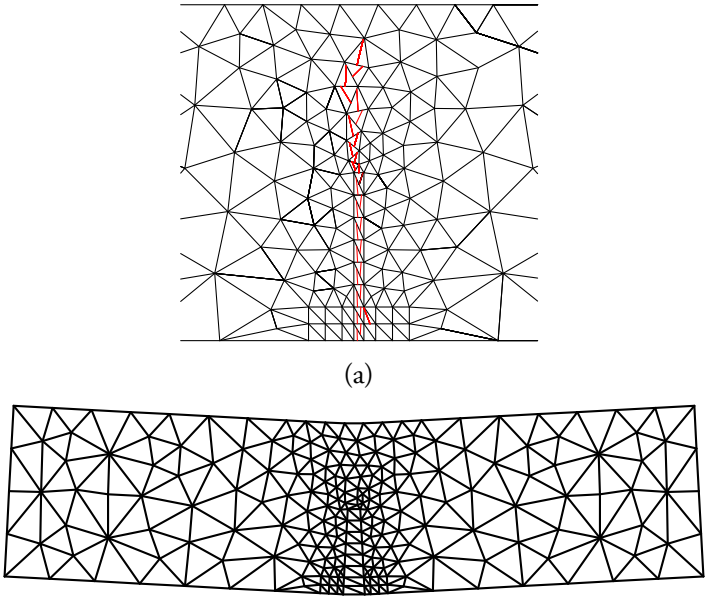

(a)

(b)

Figure 3.38: Three point bending test with a fiber bridging the notch: (a) crack pattern; (b) deformed mesh (scale = 50).

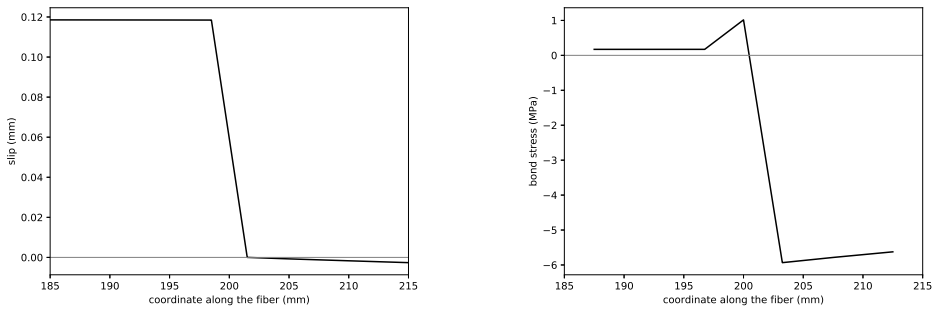

(a) (b)

Figure 3.39: Numerical simulation of the three-point bending test - distribution along the fiber at the end of the analysis: (a) slip; (b) bond stress.

The crack pattern is shown on Figure 3.38a, where the cracks in the elements representing the notch develop in the first few time steps, since the elements in the notch are very weak. The crack above the notch is clearly visible, and it represents the main failure mechanism of concrete. Also, the enriched element right of the notch has a crack that develops around time 0.028, which serves as a trigger for bond-slip activation. The deformed configuration at the end of the analysis is shown on Figure 3.38b.

From Figure 3.39, where the slip and the bond stress along the fiber at the end of the analysis are shown, it is easily seen that the fiber is getting pulled out from the left side. The maximum slip reached in the elements on the left is 0.12 mm, while the bond stress on the same side is almost equal to zero. The right side of the fiber stays in place, with a negligible slip, and still high values of bond stress.

In this section, we have shown that our methodology is able to provide a realistic description of the failure mechanisms of composites reinforced by fibers. The distinctive phases and the jump due to the bond-slip activation exhibited by real specimens have been properly represented in our numerical examples.

4

Inverse model for fiber-reinforced concrete

Contents

In this chapter, an inverse model for fiber-reinforced concrete is proposed, where it is shown how model parameters can be obtained from measurement results. First we explain the Levenberg-Marquardt method for solving inverse problems, and show its performance on two examples: for finding the stiffness of a damaged bar, and for relating beam and truss displacements. After that, the random generation of fiber distribution in the domain is explained, with its application on 2D and 3D examples. This serves as an input for the final part, where parameter identification is performed for a model based on order statistics.

The multi-scale model presented in Chapter 3, together with the micro-scale models for each constituent from Chapter 2, is quite detailed, since it takes into account a number of failure modes for the whole composite. This is, for now, implemented for a straight fiber that coincides with the element's edge. The X-FEM methodology would allow us to extend our approach to the case when the fiber is randomly oriented in the domain, and then the general displacement field approximation (3.1) should be used, to account for all the enriched degrees of freedom shown on Figure 3.1. This would also require some modifications in the computer code, regarding the boundary conditions and the bond-slip activation.

The number of fibers in a specimen can get very large, and, for example, for a specimen of dimensions 40x10x40 cm and a volume fraction of fibers of 1%, there are approximately 10000 fibers. If we would like to model such a case with our detailed multi-scale approach, the complexity of the numerical implementation would substantially increase. Then, we have to ask whether this cost in computational resources would be worth it, considering the output that we get from the model. Of course, this depends on the desired objective. In Chapters 2 and 3, our goal was to couple the failure modes of each composite ingredient, and to investigate how the processes happening at the interface affect the behavior of the composite as a whole. In this chapter the emphasis is on inverse modeling, for which a simpler model is needed for the procedure to be efficient.

That is why we are trying to see if fiber-reinforced concrete can be modeled with a stochastic approach, that would allow us to obtain a realistic behavior of the composite, and perform the identification of parameters.

4.1 Levenberg-Marquardt method for inverse problems

To model the behavior of a system subjected to mechanical loading, we use the following system of equations

$$\mathbf{K}\mathbf{u} = \mathbf{F} \tag{4.1}$$

where $\mathbf{K}$ is the stiffness matrix, $\mathbf{u}$ is the displacement vector, and $\mathbf{F}$ is the external force vector. The most common case is when the stiffness of the structure and the imposed force are known, and we want to find the values of the displacements. The solution of such a direct problem is straightforward, and we obtain it by inverting the stiffness matrix and multiplying it by the external force vector

$$\mathbf{u} = \mathbf{K}^{-1}\mathbf{F} \tag{4.2}$$

But what if we have a case when the displacements and the forces are known, and we want to find the stiffness of the structure? Then we are dealing with an inverse problem, whose solution can be obtained by an optimization procedure, or curve-fitting problem, where the best agreement possible between predicted and measured values has to be obtained. So, the problem comes down to minimizing the error between them, and different methods can be employed for doing it.

One of the methods that is often used is the Levenberg-Marquardt method, which provides an iterative and incremental way of solving the nonlinear least squares problems. The Levenberg-Marquardt method is a combination of the gradient decent method and the Gauss-Newton method [67]. When the parameters are far from their optimal value, the method behaves more like the gradient method, and performs updates by the steepest descent. When the parameters' values get closer, it is assumed that the function is locally quadratic, as in the Gauss-Newton method.

We start by defining the sum of squares

$$S = \sum_{i=1}^{n} (\mathbf{u}_i^m - \mathbf{u}_i)^2 \tag{4.3}$$

where $\mathbf{u}_i^m$ are the known values of displacements (measured experimentally) and $\mathbf{u}_i$ are the predicted values of displacements (obtained from the model). Our goal is to minimize S

$$\frac{dS}{dk} = 0 \tag{4.4}$$

where k is the parameter we want to obtain (in this case it denotes the stiffness). From (4.4) an (4.3), it follows

$$\frac{dS}{dk} = -2 \sum_{i=1}^{n} (\mathbf{u}_i^m - \mathbf{u}_i) \frac{d\mathbf{u}_i}{dk} \tag{4.5}$$

The sensitivity coefficient X_k is equal to

$$X_k = \frac{d\mathbf{u}_i}{dk} \tag{4.6}$$

and it can be introduced in (4.5) to obtain

$$\sum_{i=1}^{n} (\mathbf{u}_i^m - \mathbf{u}_i) X_k = 0 \tag{4.7}$$

From Taylor's series it follows

$$\mathbf{u}_i(k + \Delta k) = \mathbf{u}_i(k) + \frac{d\mathbf{u}_i}{dk} \Delta k \tag{4.8}$$

By introducing (4.8) into (4.7), we get

$$\sum_{i=1}^{n} \left(\mathbf{u}_i^m - \mathbf{u}_i(k) - \frac{d\mathbf{u}_i}{dk} \Delta k \right) X_k = 0 \tag{4.9}$$

By applying (4.34), and separating (4.9) into two parts, we obtain

$$\sum_{i=1}^{n} \left(\mathbf{u}_i^m - \mathbf{u}_i(k) \right) X_k - \sum_{i=1}^{n} \Delta k \, X_k^2 = 0 \tag{4.10}$$

From here, we can express the increment of k as

$$\Delta k = \frac{\sum_{i=1}^{n} (\mathbf{u}_i^m - \mathbf{u}_i) \, X_k}{\sum_{i=1}^{n} (X_k)^2} \tag{4.11}$$

The sensitivity coefficient from (4.34) can be expressed as

$$X_k = \frac{\mathbf{u}(k + \delta k) - \mathbf{u}(k)}{\delta k} = \frac{\mathbf{u}_{n+1} - \mathbf{u}_n}{\delta k} \tag{4.12}$$

where $\mathbf{u}_{n+1}$ and $\mathbf{u}_n$ are the displacement values in subsequent iterations, denoted by n.

4.1.1 Determining the stiffness of a damaged bar

To show how the described method can be applied to inverse problems, we take a simple example of a truss with a damaged bar, shown in Figure 4.1.

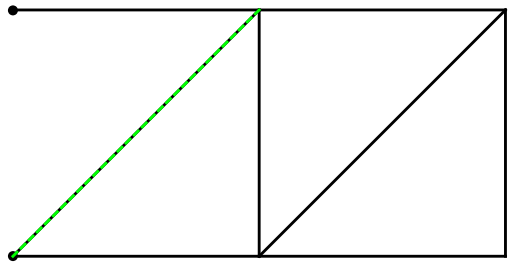

Figure 4.1: A truss with a damaged bar (shown in green).

The problem is the following: the axial stiffness of all the bars was $EA = 1000$, but one of the diagonal bars got damaged (the one shown in green on Figure 4.1), and now we want to know the reduced value of stiffness of that bar. The truss structure is fixed in nodes 1 and 2, and is subjected to an external force $F = 1$ acting in the lower right node, in y-direction. Displacements are measured in three nodes, as

shown on Figure 4.2. We simulate the measurement with error by computing the real displacements $\mathbf{u}^r$ of the structure

$$\mathbf{u}^r = \begin{bmatrix} -0.001 \\ -0.00582843 \\ 0.002 \\ -0.00482843 \\ -0.001 \\ -0.0136569 \end{bmatrix} \tag{4.13}$$

and then rounding the values to the third digit after the decimal point, to get the simulated measurements

$$\mathbf{u}^m = \begin{bmatrix} -0.001 \\ -0.006 \\ 0.002 \\ -0.005 \\ -0.001 \\ -0.014 \end{bmatrix} \tag{4.14}$$

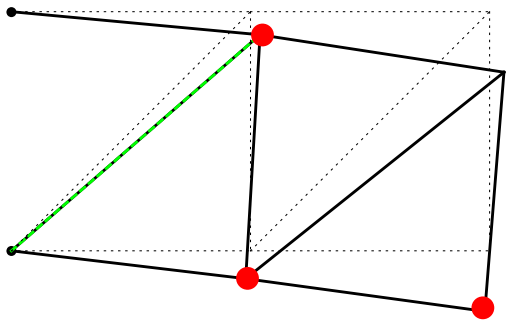

Figure 4.2: Displacements of the truss bar, with measurement points shown with red dots.

To determine the stiffness of the damaged bar, we use the Levenberg-Marquardt method, as presented in section 4.1. The whole procedure for a typical iteration can be described in the following manner. First we assume an initial stiffness of the damaged bar k_0, and compute the stiffness matrix $\mathbf{K}_0$ for the whole structure. Displacements are then computed from

$$\mathbf{u}_0 = \mathbf{K}_0^{-1}\mathbf{F} \tag{4.15}$$

We introduce a perturbation of stiffness $\delta k = 0.001\, k_0$, with which we compute the new stiffness $kk = k_0 + \delta k$. With this value in hand, we compute the new stiffness matrix $\mathbf{K}_1$.The new values of displacements are then

$$\mathbf{u}_1 = \mathbf{K}_1^{-1}\mathbf{F} \tag{4.16}$$

Table 4.1: Computation of stiffness of a damaged bar for the assumed initial stiffness $k_0 = 900$.

iteration	k_n	δk	kk	Δk	k_{n+1}
1	900	0.009	900.9	24.512	924.512
2	924.512	0.00924	925.436	0.660573	925.172
3	925.172	0.00925	926.097	-0.000189	925.172

The sensitivity coefficient is computed from (4.12)

$$X_{k,1} = \frac{\mathbf{u}_1 - \mathbf{u}_0}{\delta k} \tag{4.17}$$

The stiffness increment from (4.11) is then

$$\Delta k_1 = \frac{\sum_{i=1}^{n} (\mathbf{u}_i^m - \mathbf{u}_i)\, X_{k,1}}{\sum_{i=1}^{n} (X_{k,1})^2} \tag{4.18}$$

so we can update the stiffness and obtain the final value for this iteration

$$k_1 = k_0 + \Delta k_0 \tag{4.19}$$

Then, we proceed to the new iteration, and perform these steps again. The computation stops when two subsequent iterations yield the same value of parameter k, according to a predefined tolerance.

In our example, we have taken the initial guess for the stiffness of the damaged bar to be $k_0 = 0.9EA = 900$. We obtain the final value of stiffness $k = 925.17$ in three iterations, as shown in Table 4.1.

If we assume an initial guess that is further away from the true stiffness, we require more iterations to get to the solution. For example, for the initial stiffness $k_0 = 200$, we need 7 iterations to converge, as shown in Table 4.2.

4.1.2 Relating beam and truss displacements

In this section, an example is presented in which we want to relate two different structures: a beam and a truss, shown on Figures 4.3 and 4.4. The goal is to choose the stiffness of the diagonal bars of the truss to obtain the same displacements as the beam. This example has been presented in [43], where a methodology for relating two different structures has been presented.

Table 4.2: Computation of stiffness of a damaged bar for the assumed initial stiffness $k_0 = 200$.

iteration	k_n	δk	kk	Δk	k_{n+1}
1	200	0.2	200.2	156.922	356.922
2	356.922	0.356922	357.278	219.444	576.366
3	576.366	0.576366	576.942	217.517	793.883
4	793.883	0.793883	794.677	112.771	906.654
5	906.654	0.906654	907.56	18.1657	924.819
6	924.819	0.924819	925.744	0.35273	925.172
7	925.172	0.925172	926.097	-0.0002	925.172

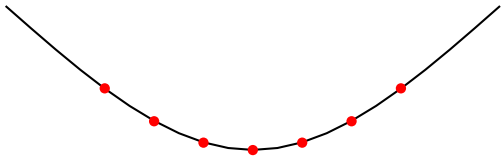

Figure 4.3: Beam with measurement points shown in red.

We observe the displacement only in seven nodes, shown with red circles on Figures 4.3 and 4.4, so for the truss we have to perform a static condensation. The stiffness of the truss bars is $EA = 1000$, and the applied force is $F_{\text{truss}} = 1$.

The simply supported beam of length $L = 10$, and stiffness $EI = 1000$, is subjected to an applied force $F_{\text{beam}} = 0.000125$ in the three central nodes. The displacements of the beam in the seven chosen nodes are

$$\mathbf{u}_{\text{beam}} = \begin{bmatrix} -0.035 \\ -0.048 \\ -0.057 \\ -0.060 \\ -0.057 \\ -0.048 \\ -0.035 \end{bmatrix} \tag{4.20}$$

so we want to get the same displacements for the truss.

We do that by changing the stiffness of the diagonals (Figure 4.5), and we perform three different analyses: first we change the stiffness of just the lower diagonals (shown in green), then we change the stiffness of only the upper diagonals (shown in yellow), and in the end we change the stiffness of both the upper and the lower diagonals.

In the first case, when we are changing just the stiffness of the upper diagonals, by using the described Levenberg-Marquardt procedure, we obtain the final result

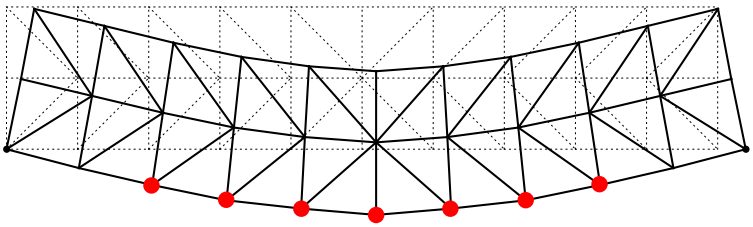

Figure 4.4: Displacements of a truss structure with measurement points shown in red.

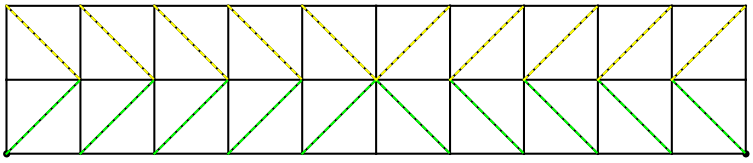

Figure 4.5: Upper diagonals (yellow) and lower diagonals (green) in a truss structure.

$EA = 168.603$ in five iterations, as shown in the second column of Table 4.3. For the case when we change just the stiffness of the upper diagonals (third column in Table 4.3), we obtain their final stiffness $EA = 166.239$ in five iterations, also.

But, when we change the stiffness of both the lower and the upper diagonals to obtain the same displacements as the beam, we do not converge to the same value in two subsequent iterations, since there are many possible combinations of stiffness that yield good results, as can be seen in the fourth column of Table 4.3. The illustration of this observation can be found on Figure 4.6 where the error in displacement as a function of diagonal stiffness is shown in semi-log plot. It is visible that many combinations of diagonal stiffness minimize the error, represented by the "valley" on the function plot.

Table 4.3: Computation of stiffness for the diagonal elements to obtain the same displacements as a beam, for three different cases.

	lower diagonals	upper diagonals	both diagonals
EA_0	100	100	$\{100, 100\}$
EA_1	146.629	145.612	$\{238.707, 169.768\}$
EA_2	166.348	164.247	$\{437.863, 236.798\}$
EA_3	168.579	166.222	$\{486.892, 247.776\}$
EA_4	168.603	166.239	$\{460.242, 241.960\}$
EA_5	168.603	166.239	$\{476.705, 245.332\}$

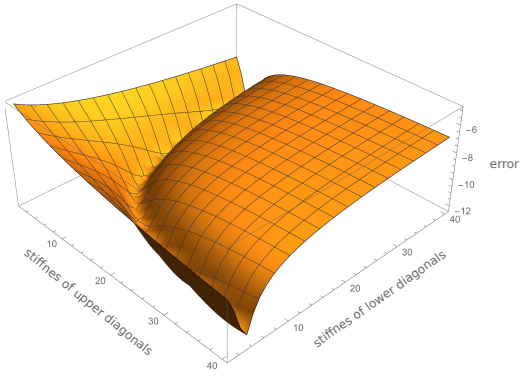

Figure 4.6: Error minimization for different combinations of diagonal stiffness.

4.2 Modeling the fiber distribution inside the domain

In this section we explain the probability distribution function of fibers inside the domain, and develop an algorithm for generating random distributions that can be applied to any given specimen. This part has been developed according to [42], and has been implemented in *Wolfram Mathematica* [45].

Processes can be assumed to be random when they are independent from each other, and have the same probability of occurring. Specifically, when modeling fiber-reinforced materials, three criteria have to be satisfied [42]:

1. the fibers are deposited independently of one another;
2. they have an equal probability of landing at all points in the domain;
3. they have an equal probability of making all possible angles with a fixed axis.

During the material fabrication in the laboratory or by industrial processes, the distribution of fibers cannot be considered completely random, since there exist imperfections in the production process. For our purposes, we will consider an ideal case where the processes can be assumed to be random. For modeling such processes, the Poisson distribution is used.

4.2.1 Poisson distribution

Poisson distribution is a limit case of the binomial distribution, when the number of trials is large, with n approaching infinity, and p approaching zero. Here, p represents the probability of a success (a positive outcome of the trial).

The probability distribution of a Poisson random variable X is

$$P(X) = \frac{e^{-\mu}\mu^{x}}{x!} \tag{4.21}$$

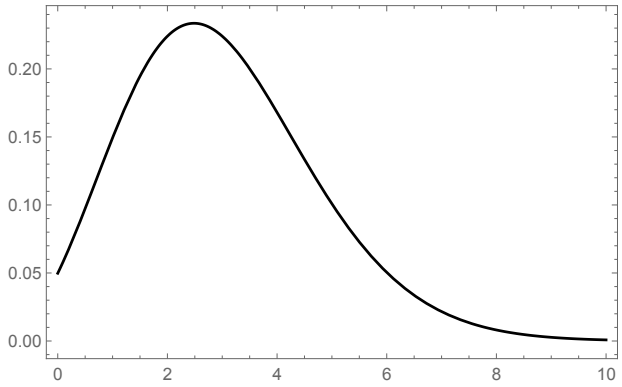

Figure 4.7: Poisson distribution with mean $\bar{x} = 3$.

where x is the number of successes, μ is the mean number of successes for a given interval or region, and $e = 2.71828$.

The mean and variance of this distribution are equal to μ, so we have

$$\bar{x} = \mu; \quad \sigma^2 = \mu \tag{4.22}$$

A graphical representation of Poisson's distribution with mean 3 is given on Figure 4.7. Poisson distribution is usually applied for modeling processes with a large number of trials and a small probability of success.

4.2.2 Modeling fiber distribution in 2D

First, we will show how to model the fiber distribution in 2D. For the sake of clarity, we will neglect the fiber thickness, and will model the fibers with lines that represent their axes.

The position of every fiber inside the domain is defined by the coordinates of its midpoint (x, y), and by the angle θ between the fiber axis and a chosen arbitrary axis. We can start by generating a random distribution of fiber midpoints in the domain, for which just the coordinates are needed.

Let's take a square of sides 10, and distribute $n = 1000$ fibers inside it. The coordinates of the fiber midpoints are generated as pseudo-random numbers in [45]. This results with 1000 pairs of numbers (x, y) obtained from the uniform distribution on the interval $\{0, 10\}$, as shown in Figure 4.8a.

When fibers are assigned length, the angle θ has to be taken into account. θ is also generated as a pseudo-random number from the interval $\{-\pi, \pi\}$. For a length $l^{\mathrm{f}} = 0.5$, we get the distribution shown on Figure 4.8b. The coordinates of the fiber

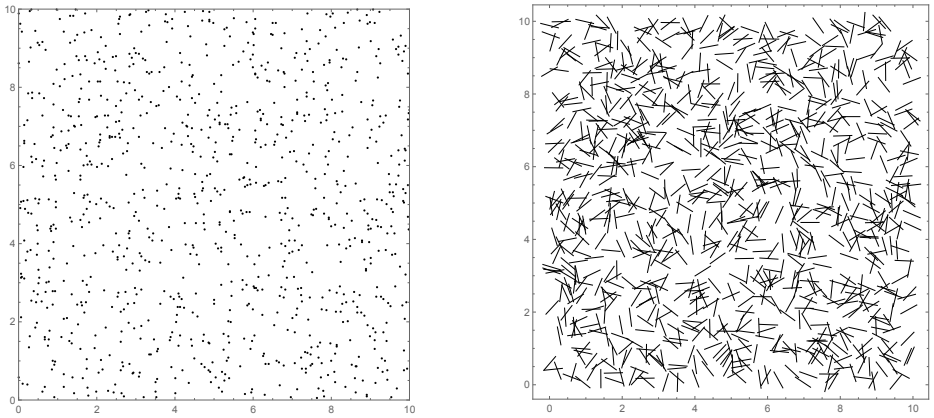

(a) (b)

Figure 4.8: Distribution of $n = 1000$ fibers inside a square domain: (a) fiber midpoints; (b) whole fibers.

ends are computed from the geometry of the fiber, from

$$x_1 = x - \frac{l^{\mathrm{f}}}{2}\cos\theta; \quad y_1 = y - \frac{l^{\mathrm{f}}}{2}\sin\theta; \tag{4.23}$$

$$x_2 = x + \frac{l^{\mathrm{f}}}{2}\cos\theta; \quad y_2 = y + \frac{l^{\mathrm{f}}}{2}\sin\theta; \tag{4.24}$$

In Figure 4.8, it can be observed that fibers are not uniformly distributed throughout the domain, but have a tendency for clustering. To look more closely into it, let's divide the square in smaller squares, as shown in Figure 4.9a.

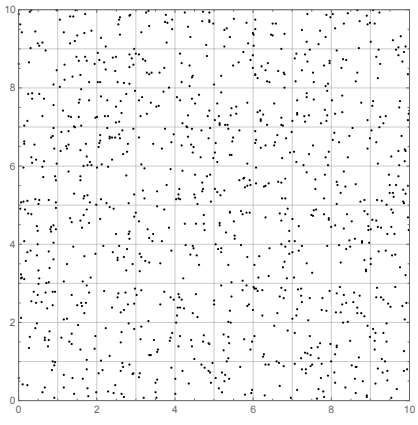

(a)

11	11	9	10	10	8	9	8	11	7
5	11	17	9	8	8	12	14	6	9
9	12	11	8	10	13	11	15	6	11
12	14	18	7	12	10	12	8	8	10
13	10	6	6	16	11	10	5	9	15
14	7	9	9	5	13	7	11	13	12
16	7	9	7	7	8	11	7	7	8
12	10	10	7	13	8	12	13	15	10
9	9	7	10	9	10	6	12	8	9
10	9	13	8	10	11	7	14	11	10

(b)

Figure 4.9: Square domain with fibers: (a) subdivision of square in zones; (b) number of points in each zone.

If we count the number of points in each zone, we get the representation in Figure 4.9b. The minimal value in this table is 5, and the maximal 18, while the mean is

equal to 10. The variance is given as

$$\sigma^2(x) = \sum_{i=1}^{n} \frac{(x_i - \bar{x})^2}{n} = 7.677 \tag{4.25}$$

The frequency of appearance of specific numbers in the table shown on Figure 4.9b is graphically represented in Figure 4.10. We can see that there are 5 zones that contain 6 points, 15 zones that contain 10 points, only one zone has 18 points, etc.

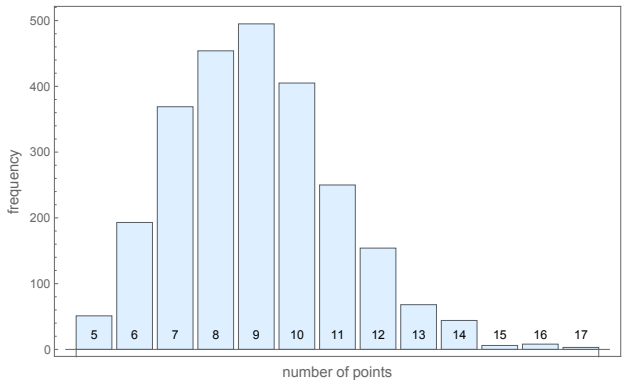

Figure 4.10: Frequency of appearance of numbers from table shown in Figure 4.9b.

The bar graph on Figure 4.10 has a shape that resembles the Poisson distribution, but since the number of zones is quite small, it cannot be represented properly. If we take a larger number of points, $n = 10000$, and decrease the size of the zones (0.2x0.2), as shown on Figure 4.11, we get a more representative sample.

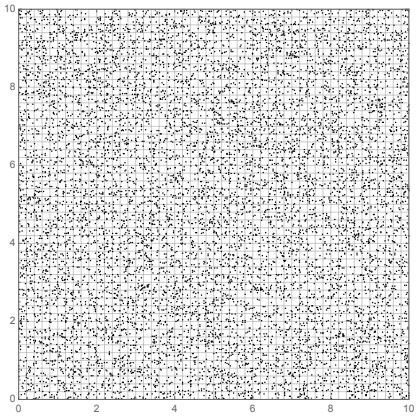

Figure 4.11: Sample with $n = 10000$ points, and 2500 zones.

Now we can compare the frequency of our points with the Poisson distribution with the same mean, which is equal to 4 in this case. The comparison is shown on Figure 4.12, where a good accordance can be observed.

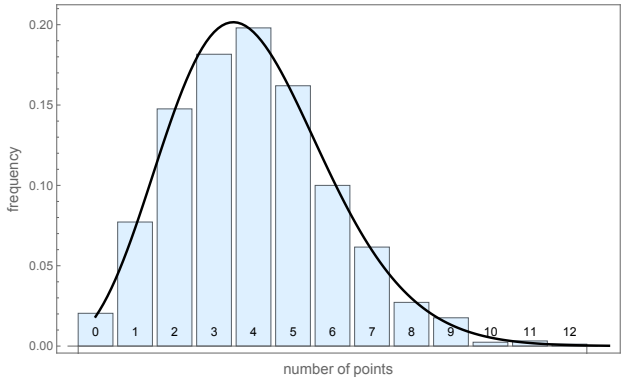

Figure 4.12: Comparison of the Poisson distribution with the frequency of appearance for the example from Figure 4.11.

The variance for this set of data is equal to $\sigma^2 = 4.106$, which is very close to the mean value $\bar{x} = 4$. On Figure 4.13, the relationship between the mean and the variance is shown for different zone sizes, varying from 10000 zones of size 0.1x0.1, to 100 zones of size 1x1. It is visible that their ratio approaches the value 1, that is a characteristic of the Poisson distribution.

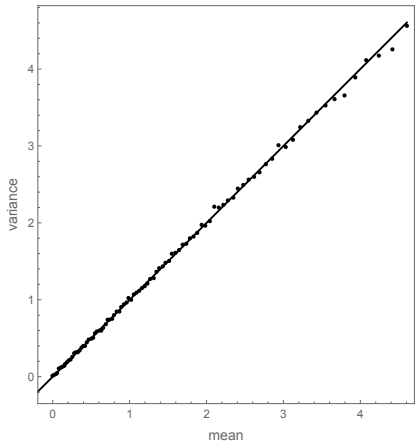

Figure 4.13: Plot of variance vs. mean in logarithmic scale for different zone sizes.

On Figure 4.14, the variance of the number of points plotted against the zone size is shown, where it can be observed that the variance decreases with the increase of the zone size.

4.2.3 Modeling fiber distribution in 3D

The fiber distribution in 3D can be generated according to a Poisson distribution, analogously to the 2D case. Of course, fiber midpoints are now defined with three coordinates, (x, y, z), and two angles, θ and ϕ.

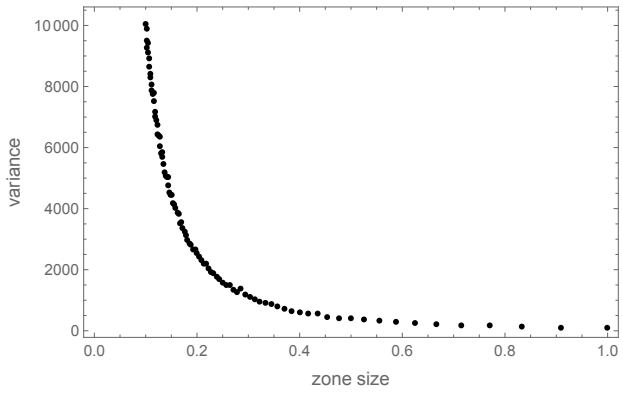

Figure 4.14: Plot of variance of number of points vs. zone size.

We take a cube of dimensions 10x10x10, and we distribute $n = 1000$ points inside it, as shown in Figure 4.15a.

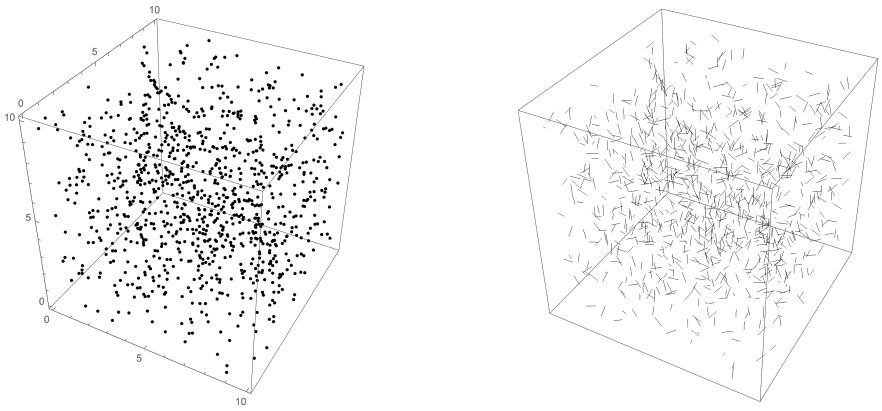

(a) (b)

Figure 4.15: Distribution of fibers in 3D: (a) fiber midpoints; (b) whole fibers.

The coordinate of the fiber ends are computed as in (4.23), but with an additional dimension

$$x_1 = x - \frac{l^{\mathrm{f}}}{2} \cos\theta \cos\phi;\ y_1 = y - \frac{l^{\mathrm{f}}}{2} \sin\theta \cos\phi;\ z_1 = z - \frac{l^{\mathrm{f}}}{2} \sin\theta; \quad (4.26)$$

$$x_2 = x + \frac{l^{\mathrm{f}}}{2} \cos\theta \cos\phi;\ y_2 = y + \frac{l^{\mathrm{f}}}{2} \sin\theta \cos\phi;\ z_1 = z + \frac{l^{\mathrm{f}}}{2} \sin\theta; \quad (4.27)$$

For fibers of length $l^{\mathrm{f}} = 0.5$, and angles from the interval $\{-Pi, Pi\}$, the distribution is shown on Figure 4.15b.

We can apply the presented procedure for generating the distribution of fibers in a real specimen. The dimensions of the concrete specimen are 40x10x10 cm, while the fiber length is equal to $l^{\mathrm{f}} = 13$ mm. We model $n = 10000$ fibers in the specimen.

After generating pseudo-random numbers (x, y, z) that represent fiber midpoints, and the angles θ and ϕ, we obtain the distribution shown in Figure 4.16.

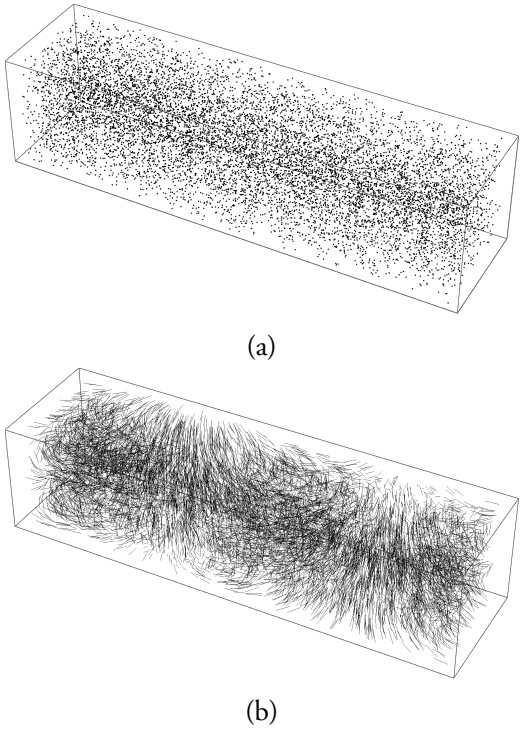

(a)

(b)

Figure 4.16: Distribution of fibers in a concrete specimen of dimensions $40x10x10$ cm: (a) fiber midpoints; (b) whole fibers.

A remark regarding the 2D fiber distribution is due, since on the graphical representation it seems that the fibers are intersecting each other, as it is shown in 4.17. Obviously, in real life this is not the case, and we can assume that the 2D specimen is just a projection on a plane, or a section cut, of a 3D specimen.

Another remark is concerning the fiber distribution near the edges of the domain is needed. Since we are generating the midpoints first, the fiber ends can sometimes fall out of the domain boundaries. We handle that type of cases by introducing a modification in the algorithm, which for a "problematic" point near the edge tries different angles until it reaches admissible values for the fiber ends' coordinates.

On Figure 4.17 it can be noticed that the fibers are clustered, and there is some free space without fibers in some parts of the domain. This is in accordance with the experimentally observed data, as shown in Figure 4.18, where fiber-reinforced specimens have been scanned with X-rays in [68].

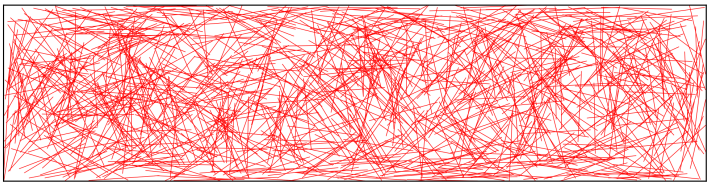

Figure 4.17: Fiber distribution in 2D.

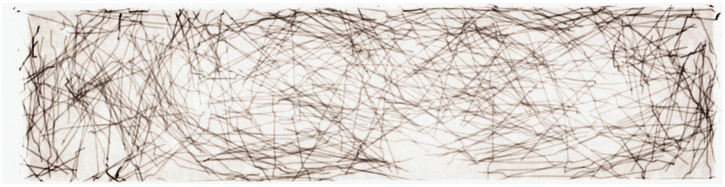

Figure 4.18: X-ray image of a fiber-reinforced concrete specimen [68].

4.3 Parameter identification for randomly oriented fibers

In this section we present a modeling approach based on order statistics and the fiber bundle model. This approach allows us to formulate an inverse model from which parameter identification can be performed.

In the fiber bundle model [69, 70], the constitutive law for each fiber contributes to the global force-displacement curve. In our model, only the fiber behavior is taken into account for now, but it could be extended to model damage in the matrix material. Fibers are taken to be linear-elastic, until a sudden fall happens, when the force in the fiber goes to zero. This could be a rough simulation of the pull-out behavior, as it has been shown in section 3.4.1 where the influence of the fiber diminishes together with the bond degradation.

The examples shown in this section have been developed in *Wolfram Mathematica* [45] and *Mathcad* [46], and are shown in [71].

4.3.1 Forward stochastic model

The fiber distribution inside the domain can be generated by the algorithm explained in section 4.2, which distributes fiber midpoints inside the domain and asigns them lengths and orientation, defined by the angle θ.

To be able to form a model that relates material parameters of the fiber with the global force-displacement diagram, we have to know the probability distribution function of either the fiber length or the fiber stiffness. Since the distribution of stiffness and lengths follows $x = \cos\theta$, we can define their probability distribution

function according to the cosine distribution [71], which is defined as follows

$$pdf(x) = \begin{cases} \dfrac{1}{\pi\sqrt{1-x^2}}, & -1 < x < 1 \\ 0, & \text{otherwise} \end{cases} \tag{4.28}$$

For our inverse model, we will use the order statistics approach in which values are arranged in ascending order. In order statistics, the size of bins, or chosen intervals on the probability distribution function, controls the precision of the method. In Figure 4.19, a graphical representation of sorted fiber lengths is shown, with their bin subdivision. On Figure 4.20, a comparison between a histogram obtained from the order statistics probability density function for 50 bins (shown in red), and the Gauss distribution (shown in blue) is given. The good agreement between the two functions shows that the sorting of random variables does not change their statistics.

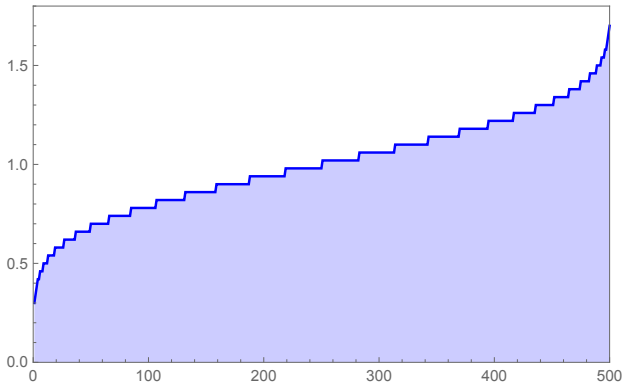

Figure 4.19: Sorted fiber lengths and their subdivision in bins.

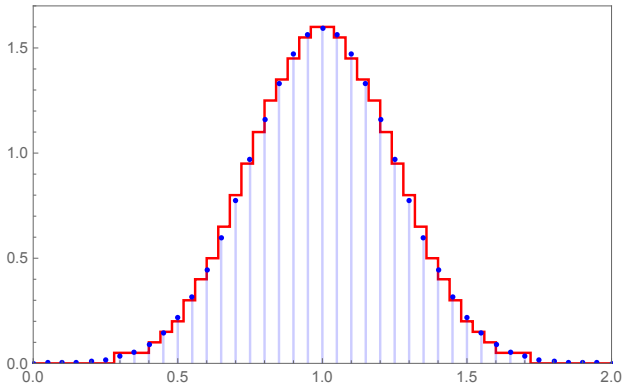

Figure 4.20: Comparison of the Gauss distribution (blue) and a histogram obtained from order statistics (red), for 50 bins.

The force-displacement diagram in the forward model is obtained as the sum of forces in individual fibers. The contribution of each fiber to the force-displacement

diagram can be defined through the following equation for the force in the fiber

$$F^{\mathrm{f}} = \begin{cases} \dfrac{EA}{l}\, u, & \text{if} \quad \dfrac{EA}{l}\, u < \mathrm{thr} \\ 0, & \text{otherwise} \end{cases} \tag{4.29}$$

where EA is the fiber stiffness, l is the fiber length, u is the displacement, and thr is the damage threshold which can be defined in stress or in strain, as will be shown in the following part.

Since we want to have a stochastic representation of the model parameters, we can choose either the length or the stiffness of the fibers as random parameters, which will be elaborated in the following part.

Length stochastic model

If we choose the length to be a random parameter, (4.29) is modified according to

$$F^{\mathrm{f}} = \begin{cases} \dfrac{EA_{\mu}}{l_{\mathrm{stoch}}}\, u, & \text{if} \quad \dfrac{u}{l} < d_{\mathrm{t}} \\ 0, & \text{otherwise} \end{cases} \tag{4.30}$$

where d_{t} is the damage threshold in strain.

We generate 500 values of fiber lengths from the normal distribution, as shown in Figure 4.21a. Their mean is equal to $\bar{x} = 1.02357$, and their standard deviation is $\sigma = 0.254297$. The sorted length values are shown in Figure 4.21b.

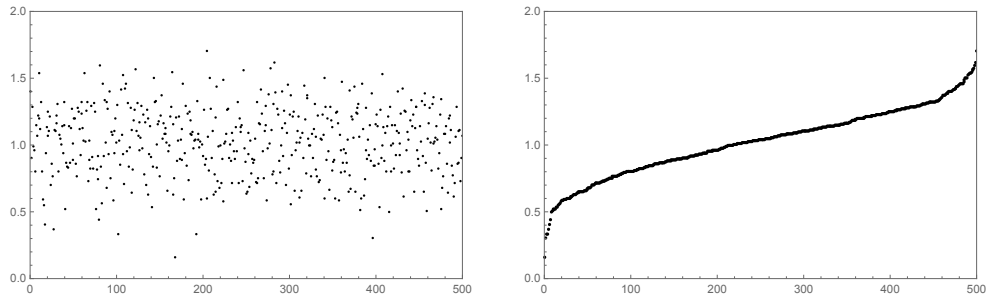

(a) (b)

Figure 4.21: 500 values of length generated from the normal distribution: (a) unsorted; (b) sorted.

Individual contributions for three randomly chosen fibers are shown on Figure 4.22a, and the force-displacement diagram generated by the sum of all the fiber contributions is shown on Figure 4.22b. We see that the combination of the "linear + sudden failure" behavior for each fiber, results with a realistic force-displacement diagram where the softening part could be considered exponential.

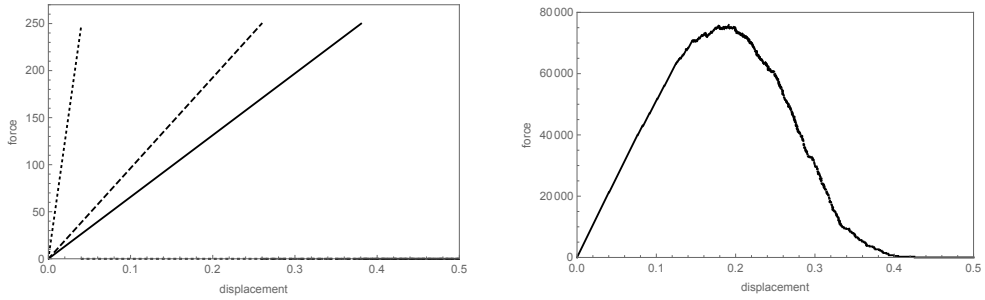

(a) (b)

Figure 4.22: Length based model: (a) individual constitutive behavior for three fibers; (b) force-displacement diagram obtained from the contribution of all the fibers' responses.

Stiffness stochastic model

If we choose the length to be a random parameter, (4.29) is modified according to

$$F^{\mathrm{f}} = \begin{cases} \dfrac{EA_{stoch}}{l_{\mu}}\, u, & \text{if} \quad \dfrac{EA_{stoch}}{l}\, u < F_{\mathrm{t}} \\ 0, & \text{otherwise} \end{cases} \tag{4.31}$$

where F_{t} is the damage threshold in stress.

As in the length model, we generate 500 values of stiffness, whose mean is $\bar{x} = 997.379$, and standard deviation $\sigma = 488.848$. The sorted and unsorted fiber stiffnesses are shown on Figure 4.23. Three individual fiber contributions for the stiffness model are shown on Figure 4.24, together with the cumulative force-displacement diagram for all the fibers.

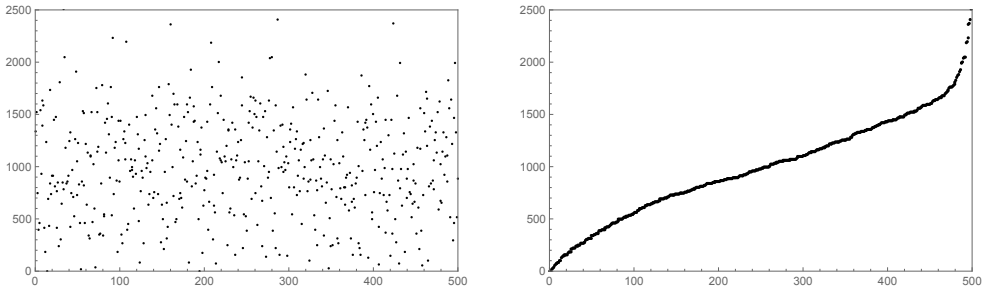

(a) (b)

Figure 4.23: 500 values of stiffness generated from the normal distribution: (a) unsorted; (b) sorted.

The stiffness stochastic model can be considered more realistic than the length model, since we assume that the randomly generated values of stiffness actually represent directional stiffness. For example, for a simple tension test, that would mean that each fiber contributes to the global response through its stiffness in the direction of the loading.

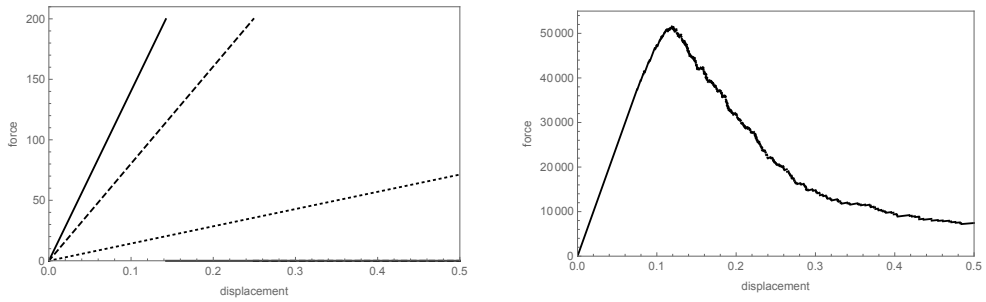

(a) (b)

Figure 4.24: Stiffness based model: (a) individual constitutive behavior for three fibers; (b) force-displacement diagram obtained from the contribution of all the fibers' responses.

4.3.2 Parameter identification

The inverse procedure used here is based on the Levenberg-Marquardt algorithm presented in section 4.1. We perform the same steps as in the two examples shown earlier, regarding the identification of stiffness of a damaged bar, and relating the beam and truss displacements by changing the stiffness of the diagonals. We follow the same procedure, but now the parameter we want to identify is not the stiffness k, but other parameters can be chosen, such as variance, mean, etc. For the general case, we will denote the parameter by σ.

From (4.3), it follows

$$S = \sum_{i=1}^{n} (F\delta_i^m - F\delta_i)^2 \tag{4.32}$$

where $F\delta_i^m$ are measured values, and $F\delta_i$ are values that will be estimated from the model. Here, i denotes the number of measurement points on the force-displacement curve.

From the minimization procedure we obtain the increment of the estimated parameter

$$\Delta\sigma = \frac{\sum_{i=1}^{n} (F\delta_i^m - F\delta_i)\, X_\sigma}{\sum_{i=1}^{n} (X_\sigma)^2} \tag{4.33}$$

where the sensitivity coefficient X_σ is defined as

$$X_\sigma = \frac{dF\delta_i}{d\sigma} \tag{4.34}$$

Figure 4.25 presents the results for parameter estimation of fiber parameters obtained from the inverse procedure for the cosine distribution. The force-displacement

curve that represents the experimental results (shown in red on Figure 4.25) is obtained from Monte Carlo simulations with the following input parameters: mean stiffness $EA_{\text{mean}} = 100$, variance $\sigma_{\text{EA}} = 500$, damage threshold $F_{\text{tol}} = 200$.

The orange dots on Figure 4.25 represent the chosen measurement points on the diagram, from which the input for the inverse model is derived. To obtain a proper representation of all the phases of the response, the points have to be selected along the whole diagram.

The purple line in Figure 4.25 (denoted as "model exact") represents the results of the inverse procedure obtained for the same value of damage threshold, $F_{\text{tol}} = 200$. A good agreement between predicted and measured values can be observed, even though the inverse procedure could become more precise by choosing smaller bins in the order statistics model. The other lines on Figure 4.25 represent the results of the inverse model obtained by varying the damage threshold from 50 to 300.

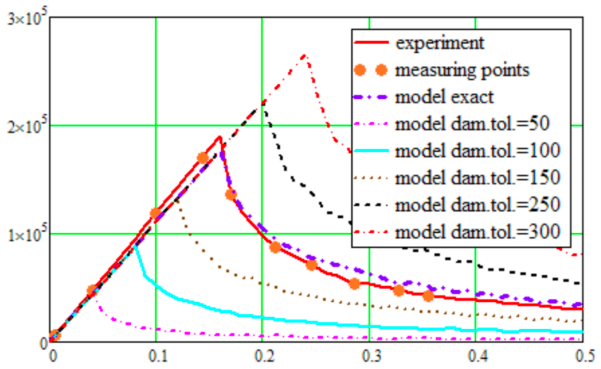

Figure 4.25: Results of the parameter identification procedure, for different values of the damage threshold [71].

Figure 4.26 represents the results of the parameter identification procedure for three different cases. In all graphs, the results of the forward model (denoted by "experiment") are shown in red. As in the previous example, the purple curve is obtained by having the same parameters in the order statistics model as in the forward model.

On Figure 4.26a, we are comparing the force-displacement diagrams for different stiffness variance, ranging from 10% to 100%. On Figure 4.26b, the damage threshold is varying from 50 to 300. On Figure 4.26, we are comparing the results for different values of stiffness mean, from 50% to 180% of the exact value.

In [71], a sensitivity analysis has been performed, in which it has been shown that the minima for the Levenberg-Marquardt procedure are clearly visible, allowing for a robust and efficient computation.

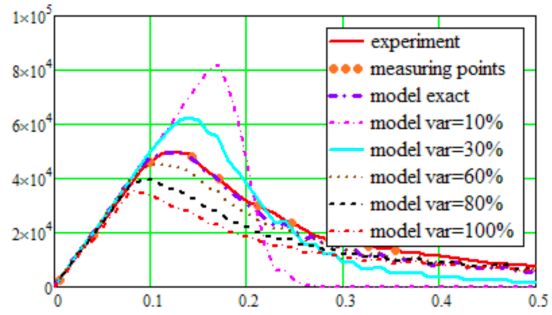

(a)

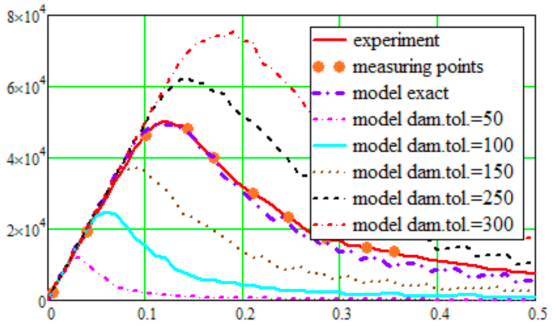

(b)

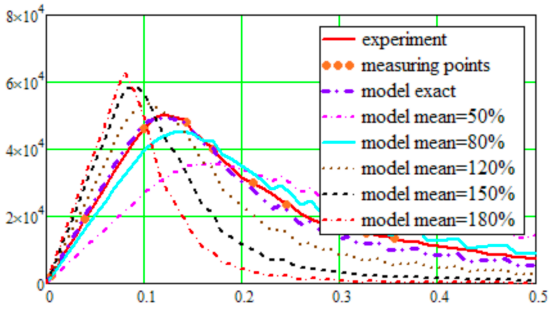

(c)

Figure 4.26: Results for the parameter identification procedure from [71]: (a) different stiffness variance; (b) different force damage threshold; (c) different stiffness mean.

5
Conclusion

In this section we give a commentary on the obtained results, and provide an overview of the proposed methodology. Original scientific contributions are stated, together with the perspectives for future work.

In this thesis, a multi-scale framework for modeling damage in fiber-reinforced composites has been presented. It is based on a combination of two different approaches: the embedded discontinuity finite element method (ED-FEM), for taking into account localized failure in concrete; and the extended finite element method (X-FEM), that takes care of the presence of the fiber in the domain. Our goal was to combine the best of each approach to achieve good results without sacrificing model consistency or computational robustness.

The behavior of concrete is described with a damage constitutive law to describe the development of micro-cracks, and a discontinuity in the displacement field which represents a macro-crack. In the hardening phase, volume dissipation takes place, and in the softening phase, surface dissipation happens. The slip between the fiber and the concrete is described with the extended finite element method, which takes into account the discontinuities and inclusions at the global level. For an element that contains the fiber, the displacement field is composed of the standard and the enriched part.

During experimental tests, we have observed that the ends of the fiber can get pulled out of the surrounding concrete. That is why we have proposed a new approach for handling bond-slip, where the boundary condition for the enriched degrees of freedom is positioned in the cracked element. That results with zero slip in the fixed node, with the largest slip taking place at the fiber ends.

We have performed several numerical simulations to test our approach. The first is a tensile test with different fiber lengths, for a linear elastic and a damage case. We have observed that the increase of the fiber length leads to a stiffer model response and increases the ductility in the softening part.

To better understand the failure mechanisms of fiber-reinforced concrete and to validate our model, single-fiber pull-out tests and three-point bending tests on notched specimens have been performed. During the experiments, it has been observed that fibers do not break, but they get pulled out of concrete, as has been implemented in our model.

The original scientific contributions of this work include the following: the development of a novel finite element where the presented multi-scale approach is implemented; the treatment of bond-slip without the need for an interface element; development of a model for bond-slip that can take into account the complete fiber pull-out; outlining the differences regarding bond-slip activation and boundary conditions along the fiber; development of an inverse model for fiber-reinforced concrete based on the stochastic representation of fibers.

The proposed model could be extended to take into account the plasticity in the fiber behavior. For bond-slip, a complete constitutive law could be defined by

combining the elasto-plastic model for standard reinforcement with the pull-out law for fiber reinforcement. Also, the case with a randomly oriented fiber could be considered, with the extension for taking care of multiple fibers inside the domain, and for more than one fiber in each element. Regarding the inverse model, extensions could go in the direction of changing the chosen behavior of the fibers to take into account more complex constitutive relations. Also, the behavior of the matrix material could be added into the model, which would give a more realistic representation of the composite's failure mechanisms.

For now, the focus of our work has been on the durability of structures in quasi-fragile composite materials, such as fiber-reinforced concrete. Nevertheless, the same approach could be easily extended to take into account different types of constitutive laws of materials and different types of fibers (including the longer ones, as in woven materials). We can also consider the application of the methodology developed in this thesis to other areas of applied mechanics, such as biomechanics, or the fabrication of materials with engineered microstructures.

Bibliography

[1] World Nuclear Association, Nuclear Power in FRANCE. http://www.world-nuclear.org/information-library/country-profiles/countries-a-f/france.aspx. Accessed: 2018-10-30.

[2] Brandt, A. M. Fibre reinforced cement-based (FRC) composites after over 40 years of development in building and civil engineering. *Composite structures 86*, 1 (2008), 3–9.

[3] Torquato, S. Modeling of physical properties of composite materials. *International Journal of Solids and Structures 37*, 1 (2000), 411–422.

[4] Xu, H., Li, Y., Brinson, C., and Chen, W. A descriptor-based design methodology for developing heterogeneous microstructural materials system. *Journal of Mechanical Design 136*, 5 (2014), 051007.

[5] Savvas, D., Stefanou, G., Papadrakakis, M., and Deodatis, G. Homogenization of random heterogeneous media with inclusions of arbitrary shape modeled by XFEM. *Computational Mechanics 54*, 5 (Nov 2014), 1221–1235.

[6] Unger, J. F., and Eckardt, S. Multiscale modeling of concrete. *Archives of Computational Methods in Engineering 18*, 3 (2011), 341–393.

[7] Ibrahimbegovic, A., and Markovic, D. Strong coupling methods in multi-phase and multi-scale modeling of inelastic behavior of heterogeneous structures. *Computer Methods in Applied Mechanics and Engineering 192*, 28 (2003), 3089–3107.

[8] Kouznetsova, V., Brekelmans, W., and Baaijens, F. An approach to micro-macro modeling of heterogeneous materials. *Computational Mechanics 27*, 1 (2001), 37–48.

[9] Niekamp, R., Markovic, D., Ibrahimbegovic, A., Matthies, H. G., and Taylor, R. L. Multi-scale modelling of heterogeneous structures with inelastic constitutive behavior: Part II–software coupling implementation aspects. *Engineering computations 26*, 1/2 (2009), 6–28.

[10] Ren, X., and Li, J. Multi-scale based fracture and damage analysis of steel fiber reinforced concrete. *Engineering Failure Analysis 35* (2013), 253–261.

[11] Bažant, Z. P., Caner, F. C., Carol, I., Adley, M. D., and Akers, S. A. Microplane model M4 for concrete. I: Formulation with work-conjugate deviatoric stress. *Journal of Engineering Mechanics 126*, 9 (2000), 944–953.

[12] Pijaudier-Cabot, G., and Mazars, J. Damage models for concrete. *Handbook of materials behavior models 2* (2001), 500–512.

[13] Schlangen, E., and Garboczi, E. Fracture simulations of concrete using lattice models: computational aspects. *Engineering fracture mechanics 57*, 2 (1997), 319–332.

[14] Nikolić, M., Karavelić, E., Ibrahimbegovic, A., and Miščević, P. Lattice element models and their peculiarities. *Archives of Computational Methods in Engineering* (2017), 1–32.

[15] Ibrahimbegovic, A., and Delaplace, A. Microscale and mesoscale discrete models for dynamic fracture of structures built of brittle material. *Computers & Structures 81*, 12 (2003), 1255–1265.

[16] Rena, C. Y., Ruiz, G., and Chaves, E. W. A comparative study between discrete and continuum models to simulate concrete fracture. *Engineering Fracture Mechanics 75*, 1 (2008), 117–127.

[17] Ibrahimbegovic, A., and Wilson, E. A modified method of incompatible modes. *Communications in applied numerical methods 7*, 3 (1991), 187–194.

[18] Jukic, M., Brank, B., and Ibrahimbegovic, A. Failure analysis of reinforced concrete frames by beam finite element that combines damage, plasticity and embedded discontinuity. *Engineering structures 75* (2014), 507–527.

[19] Do, X. N., Ibrahimbegovic, A., and Brancherie, D. Dynamics framework for 2D anisotropic continuum-discrete damage model for progressive localized failure of massive structures. *Computers & Structures 183* (2017), 14–26.

[20] Ibrahimbegovic, A., and Melnyk, S. Embedded discontinuity finite element method for modeling of localized failure in heterogeneous materials with structured mesh: an alternative to extended finite element method. *Computational Mechanics 40*, 1 (2007), 149–155.

[21] Gal, E., and Kryvoruk, R. Meso-scale analysis of FRC using a two-step homogenization approach. *Computers & Structures 89*, 11 (2011), 921–929.

[22] Bolander, J. E., and Sukumar, N. Irregular lattice model for quasistatic crack propagation. *Physical Review B 71*, 9 (2005), 094106.

[23] Radtke, F., Simone, A., and Sluys, L. A partition of unity finite element method for obtaining elastic properties of continua with embedded thin fibres. *International Journal for Numerical Methods in Engineering 84*, 6 (2010), 708–732.

[24] Babuska, I., and Melenk, J. M. The partition of unity method. *International Journal for Numerical Methods in Engineering 40* (1997), 727–758.

[25] Radtke, F. K. F., Simone, A., and Sluys, L. J. A partition of unity finite element method for simulating non-linear debonding and matrix failure in thin fibre composites. *International Journal for Numerical Methods in Engineering 86*, 4-5 (2011), 453–476.

[26] Fries, T.-P., and Belytschko, T. The extended/generalized finite element method: an overview of the method and its applications. *International Journal for Numerical Methods in Engineering 84*, 3 (2010), 253–304.

[27] Hickman, M., and Basu, P. Stochastic multiscale characterization of short-fiber reinforced composites. *Technische Mechanik 36*, 1-2 (2016), 13–31.

[28] Pike, M. G., and Oskay, C. XFEM modeling of short microfiber reinforced composites with cohesive interfaces. *Finite Elements in Analysis and Design 106* (2015), 16–31.

[29] Pike, M. G., and Oskay, C. Three-dimensional modeling of short fiber-reinforced composites with extended finite-element method. *Journal of Engineering Mechanics 142*, 11 (2016), 04016087.

[30] Ibrahimbegovic, A., Boulkertous, A., Davenne, L., and Brancherie, D. Modelling of reinforced-concrete structures providing crack-spacing based on X-FEM, ED-FEM and novel operator split solution procedure. *International Journal for Numerical Methods in Engineering 83*, 4 (2010), 452–481.

[31] Dominguez, N., Brancherie, D., Davenne, L., and Ibrahimbegović, A. Prediction of crack pattern distribution in reinforced concrete by coupling a strong discontinuity model of concrete cracking and a bond-slip of reinforcement model. *Engineering Computations 22*, 5/6 (2005), 558–582.

[32] Ben-David, O., Cohen, G., and Fineberg, J. The dynamics of the onset of frictional slip. *Science 330*, 6001 (2010), 211–214.

[33] Kammer, D. S., Radiguet, M., Ampuero, J.-P., and Molinari, J.-F. Linear elastic fracture mechanics predicts the propagation distance of frictional slip. *Tribology letters 57*, 3 (2015), 23.

[34] Sciegaj, A., Larsson, F., Lundgren, K., Nilenius, F., and Runesson, K. A multiscale model for reinforced concrete with macroscopic variation of reinforcement slip. *Computational Mechanics* (2018), 1–20.

[35] Wriggers, P., Zavarise, G., and Zohdi, T. A computational study of interfacial debonding damage in fibrous composite materials. *Computational Materials Science 12*, 1 (1998), 39–56.

[36] Hutchinson, J. W., and Jensen, H. M. Models of fiber debonding and pullout in brittle composites with friction. *Mechanics of materials 9*, 2 (1990), 139–163.

[37] Beckert, W., and Lauke, B. Critical discussion of the single-fibre pull-out test: does it measure adhesion? *Composites science and technology 57*, 12 (1998), 1689–1706.

[38] Jankowiak, T., and Lodygowski, T. Identification of parameters of concrete damage plasticity constitutive model. *Foundations of civil and environmental engineering 6*, 1 (2005), 53–69.

[39] Rosic, B. V., Kucerova, A., Sykora, J., Pajonk, O., Litvinenko, A., and Matthies, H. G. Parameter identification in a probabilistic setting. *Engineering Structures 50* (2013), 179–196.

[40] Brancherie, D., and Ibrahimbegovic, A. Novel anisotropic continuum-discrete damage model capable of representing localized failure of massive structures: Part I:

theoretical formulation and numerical implementation. *Engineering Computations 26*, 1/2 (2009), 100–127.

[41] Grbac, M. Nonlinear analysis of a fiber-reinforced beam (Nelinearni proračun gredice armirane vlaknima). Master's thesis, University of Rijeka, Faculty of Civil Engineering, 2016.

[42] Sampson, W. W. *Modelling Stochastic Fibrous Materials with Mathematica®*. Springer Science & Business Media, 2008.

[43] Kožar, I., Rukavina, T., and Malić, N. T. Similarity of structures based on matrix similarity. *Tehnicki vjesnik/Technical Gazette 24*, 1 (2017).

[44] Taylor, R. *FEAP - Finite Element Analysis Program*, 2014.

[45] Wolfram Research, Inc. Mathematica, wolfram language and system, documentation center, 2015.

[46] PTC Mathcad. Mathcad 14, electronic documentation: Mathcad user's guide, 2007.

[47] Geuzaine, C., and Remacle, J.-F. Gmsh: a three-dimensional finite element mesh generator with built-in pre-and post-processing facilities (2008).

[48] Ibrahimbegovic, A., and Brancherie, D. Combined hardening and softening constitutive model of plasticity: precursor to shear slip line failure. *Computational Mechanics 31*, 1 (2003), 88–100.

[49] Benkemoun, N., Ibrahimbegovic, A., and Colliat, J.-B. Anisotropic constitutive model of plasticity capable of accounting for details of meso-structure of two-phase composite material. *Computers & Structures 90* (2012), 153–162.

[50] Kozar, I., Ibrahimbegovic, A., and Rukavina, T. Material model for load rate sensitivity. *Coupled Systems Mechanics 7*, 2 (2018), 141–162.

[51] Kozar, I., and Rukavina, T. The effect of material density on load rate sensitivity in nonlinear viscoelastic material models. *Archive of Applied Mechanics 8* (2018).

[52] Kucerova, A., Brancherie, D., Ibrahimbegovic, A., Zeman, J., and Bittnar, Z. Novel anisotropic continuum-discrete damage model capable of representing localized failure of massive structures: Part ii: identification from tests under heterogeneous stress field. *Engineering Computations 26*, 1/2 (2009), 128–144.

[53] Kožar, I., Rukavina, T., and Ibrahimbegović, A. Method of incompatible modes–overview and application. *Građevinar 70*, 1 (2018), 19–29.

[54] Zienkiewicz, O. C., Taylor, R. L., and Zhu, J. Z. *The Finite Element Method: Its Basis and Fundamentals*. Butterworth-Heinemann, 2005.

[55] Brancherie, D. *Modéles continus et discrets pour les problémes de localisation et de rupture fragile et/ou ductile*. PhD thesis, École normale supérieure de Cachan-ENS Cachan, 2003.

[56] Smolčić, Ž., and Ožbolt, J. Meso scale model for fiber-reinforced-concrete: Microplane based approach. *Computers and Concrete 17*, 4 (2017), 375.

[57] Ožbolt, J., Lettow, S., and Kožar, I. Discrete bond element for 3D finite element analysis of reinforced concrete structures. In *Proceedings of the 3rd International Symposium: Bond in Concrete-from research to standards. Budapest: University of Technology and Economics* (2002), p. 4.

[58] Kohnehpooshi, O., and Jaafar, M. Non-linear three dimensional finite elements for composite concrete structures. *Latin American Journal of Solids and Structures 14*, 3 (2017), 398–421.

[59] Šćulac, P., Jelenić, G., and Škec, L. Kinematics of layered reinforced-concrete planar beam finite elements with embedded transversal cracking. *International journal of solids and structures 51*, 1 (2014), 74–92.

[60] Batoz, J.-L., and Dhatt, G. Incremental displacement algorithms for nonlinear problems. *International Journal for Numerical Methods in Engineering 14*, 8 (1979), 1262–1267.

[61] Stanić, A., and Brank, B. A path-following method for elasto-plastic solids and structures based on control of plastic dissipation and plastic work. *Finite Elements in Analysis and Design 123* (2017), 1–8.

[62] Rukavina, T., Ibrahimbegovic, A., and Kozar, I. Modelling fibers in fiber-reinforced composites. In *3rd International Conference on Multiscale Computational Methods for Solids and Fluids* (2017).

[63] Ellis, B., McDowell, D., and Zhou, M. Simulation of single fiber pullout response with account of fiber morphology. *Cement and Concrete Composites 48* (2014), 42–52.

[64] Rukavina, T., Ibrahimbegovic, A., and Kozar, I. Multi-scale representation of plastic deformation in fiber-reinforced materials: application to reinforced concrete. *Latin American Journal of Solids and Structures* (2018).

[65] Ibrahimbegovic, A. *Nonlinear solid mechanics: theoretical formulations and finite element solution methods*. Springer, 2009.

[66] Isla, F., Ruano, G., and Luccioni, B. Analysis of steel fibers pull-out. experimental study. *Construction and Building Materials 100* (2015), 183–193.

[67] Gavin., H. P. The Levenberg-Marquardt method for nonlinear least squares curve-fitting problems. http://people.duke.edu/ hpgavin/ce281/lm.pdf, 2017.

[68] Kalincevic, S. Determination of homogeneity of steel fibres in concrete specimens using computational tomography (Ispitivanje homogenosti raspodjele vlakana u mikroarmiranom betonu primjenom računalne tomografije). Master's thesis, University of Rijeka, Faculty of Civil Engineering, 2016.

[69] Raischel, F., Kun, F., and Herrmann, H. J. Continuous damage fiber bundle model for strongly disordered materials. *Physical Review E 77*, 4 (2008), 046102.

[70] Rinne, H. Location-scale distributions – linear estimation and probability plotting using matlab. *Justus–Liebig–Univ., Dept. of Economics and Management Science, Giessen, Germany* (2010).

[71] Kozar, I., Toric Malic, N., and Rukavina, T. Inverse model for pullout determination of steel fibers. *Coupled Systems Mechanics 7*, 2 (2018), 197–209.

Appendices

List of Tables

List of Figures